Ballistic Resistance of Multi-layered Steel Shields

by

Min Huang

B.S., Material Science and Engineering (2005)

Tsinghua University

Submitted to the Department of Mechanical Engineering
in Partial Fulfillment of the Requirements for the Degree of
Master of Science in Mechanical Engineering

at the

MASSACHUSETTS INSTITUTE OF TECHNOLOGY

June 2007

© Massachusetts Institute of Technology 2007. All rights reserved.

Signature of Author.....
Department of Mechanical Engineering
May 10, 2007

Certified by.....
Tomasz Wierzbicki
Professor of Applied Mechanics
Thesis Supervisor

Accepted by.....
Lallit Anand
Professor of Mechanical Engineering
Chairman, Department Committee on Graduate Students

MASSACHUSETTS INSTITUTE OF TECHNOLOGY
JUL 13 2007
LIBRARIES

BARKER

Ballistic Resistance of Multi-layered Steel Shields

by

Min Huang

Submitted to the Department of Mechanical Engineering
on May 10, 2007, in Partial Fulfillment of the Requirements for the Degree of
Master of Science in Mechanical Engineering

ABSTRACT

In this thesis, the ballistic resistance of multi-layered steel shields against projectile impact at the sub-ordnance velocity is evaluated using finite element simulations. Eight types of projectiles of different weight and nose shapes are considered, while the multi-layered shields studied are the double-layered shield with the plates initially in contact, the double-layered shield with the plates spaced, the double-layered shield with the plates welded together and the BRAS shield. According to our simulation results, the double-layered shields are able to improve the ballistic limit by 7.0% - 25.0% under the impact of the flat-nose projectile, compared to the monolithic plate of the same weight. Under the impact of the conical-nose projectile, the double-layered shields are almost as capable as the monolithic plates. For the double-layered shields with different material combinations, the best configuration is that with the upper layer of high ductility material and the lower layer of low ductility material under moderate detrimental impact. The configuration results in some 25% gain in the ballistic limit. The worst configuration is that with the upper layer of low ductility material and the lower layer of high ductility material. The BRAS shield, which has been shown to resist blast loading is proved to be equal to the monolithic plate in perforation resistance against the flat-nose projectile. This research helps resolve the long outstanding issue of the ballistic resistance of the multi-layered configurations.

Thesis Supervisor: Tomasz Wierzbicki
Title: Professor of Applied Mechanics

Acknowledgement

First of all, I would like to express my heartful gratitude to Professor Tomasz Wierzbicki for his guidance, support and great vision during my two years graduate study at MIT, and for providing me with Research Assistantship all long. Throughout my life, I haven't met such a wonderful person as an advisor. Also, I wish to thank Professor Parks, my co-advisor, for his valuable guidance and encouragement.

To my colleagues at the Impact and Crashworthiness Lab, Post Doctor Xiaoqing Teng, Dr. Yuanli Bai, Dr. Liang Xue, Dr. Carey Walter, Dr. JongMin Shim and others, thank you for all your help and creating a pleasant working environment.

I am sincerely indebted to my parents-in-law, my uncle and my aunt-in law and my friends Simon Li, for their financial support during my studying abroad.

This work was partially supported by the ONR/MORI grant on "Development of Adaptive Blast Resistant Structures" and by the ARO grant on "Effect of Strain Rate on Fracture".

Contents

List of Figures

List of Tables

Nomenclature

d	diameter of projectile
M_0	mass of projectile
H	thickness of shield
V_0	initial impact velocity
t	time
$\bar{\sigma}$	von Mises stress
A, B, C, n, m	material constants in the Johnson-Cook constitutive model
$\bar{\varepsilon}_{pl}$	effective plastic strain
$\dot{\bar{\varepsilon}}_{pl}$	current plastic strain rate
$\dot{\bar{\varepsilon}}_0$	reference strain rate
$\bar{\varepsilon}_f$	equivalent strain to fracture
η	stress triaxility
T	temperature
T_0	room temperature
T_m	melting temperature
E	kinetic energy
v	poisson's ratio
ρ	density
C_v	specific heat

D	damage indicator
D_1, D_2, D_3	three material constants in the Johnson-Cook fracture model
C_1	scaling parameter of stress-strain curve
C_2	scaling parameter of fracture strain

Chapter 1
Introduction

In military and civilian applications, optimization of metal shields against projectile impact has long been of interest. In this thesis, several multi-layered configurations that consist of several parallel layers or inner structures have been proposed as a potential improvement over monolithic plates. Although a lot of experimental, numerical and theoretical investigations have been done on the perforation resistance of monolithic plates, there is limited study on that of multi-layered shields reported in the open literature.

From the perforation test of multi-layered beams impacted by a spherical-nose projectile, Marom and Bonder [1] concluded that the multi-layered beams were more effective in perforations resistance than the monolithic beams of the same weight. Besides, Corran et al. [2] found from a series of impact tests that a double/triple-layered shield is superior in ballistic resistance than a monolithic plate if the total thickness exceeded a critical value. However, Radin and Goldsmith [3] obtained an opposite conclusion through the normal impact tests of a blunt-nose and a conical-nose projectile on multi-layered shields of the thickness ranges from 1.6mm to 6.4mm. The ballistic limits of the monolithic plates were always higher than that of the multiple-layered shields for all types of projectiles. This finding was confirmed by Almohandes et al. [4] through an extensive tests on steel shields of varies configurations impacted by the

standard 7.62mm bullet projectiles. Recently, Dey et al. [5, 6] has executed a comprehensive experimental and numerical study on the perforation resistance of the double-layered steel shields. It was found that, in the case with the blunt-nose projectile, the ballistic limits of the double-layered shields are 30% higher than the monolithic one.

Meanwhile, several analytical models were also developed to determine the ballistic resistance of the multi-layered shields. For example, the effect of the spacing between two layers on the ballistic limits is studied by Ben-Dor et al. [7]. They concluded that the perforation resistance was not changed significantly by increasing the spacing. Elek et al. [8] extended the penetration model developed by Liss et al. [9] to the case with multi-layered shields. The theoretical solutions indicate that a monolithic plate is superior in ballistic resistance than a multi-layered shield of the same thickness. Furthermore, a simple theoretical model for the shear plugging process of the multi-layered shields was proposed by Liang et al. [10].

From the above literature review, it appears that the protection effectiveness of the multi-layered shields remains a subject of controversy. In this connection, two questions can be posed: Under what type of projectile impact, would a multi-layered shield be superior in the perforation resistance than a monolithic plate of the same weight? Among ductility and strength, which property is more important for perforation resistance against projectile impact?

Actually, different failure modes may be developed in one single shield by changing impact conditions, e.g. see Teng and Wierzbicki [11], and Børvik et al. [12, 13]. A failure mode with higher energy absorption can significantly improve the ballistic resistance of a shield. By replacing a monolithic plate with a double-layered shield, the bending resistance can be increased and thus the double-layered shield may undergo considerable deformation before fracture. By using two different grades of metals of various strength and ductility for two layers, the combined effect of ductility and strength on energy dissipation can be optimized. Furthermore, the perforation resistance of Blast Resistance

Adaptive Sandwich (BRAS), which is a good configuration for blast resistance [14], is of great interest. The objective of the present paper is to evaluate the performance of the multi-layered configuration against projectile impact.

In practical applications, a variety of projectiles including heavy fragments generated from Improvised Explosive Devices and light bullet projectiles typical for small guns may be encountered. Since a shield would behave differently under the impact of various projectiles, eight types of projectiles of different weight and nose shapes are considered in this thesis to thoroughly investigate the perforation resistance of a shield.

There are three additional important parameters for the multi-layered configurations: spacing, material parameter, and thickness ratio between each part. For simplicity, four multi-layered configurations are considered in this thesis: (1) two paralleled plates in contact, (2) two paralleled plates spaced, (3) two paralleled plates welded together and (4) the BRAS structure. Also, two materials of varied strength and ductility are designed for two layers of the double-layered shields, while the same material is considered for other configurations.

For each projectile-target system, a thorough of parametric studies would be conducted to determine the ballistic resistance of the shields. A corresponding experimental study could be overly expensive. As an alternative way, the commercial finite element codes such as ABAQUS/Explicit is able to fulfill this task with a suitable fracture model equipped. In this thesis, all perforation tests are simulated by ABAQUS/Explicit. The numerical modeling provides an insight into failure mechanisms and the number of necessary tests is reduced. In the end, the thesis concluded by pointing out the advantages of the multi-layered configuration over the monolithic plates.

Chapter 2
Problem Description

2.1 Computational models

The target shields considered in this thesis are (a) monolithic plate, (b) double-layered shield with the plates initially in contact, (c) double-layered shield with the plates spaced, (d) double-layered shield with the plates welded together, see Fig. 2.1. In addition, a more complex BRAS shield, which is shown previously to resist blast loading, is considered, see Fig. 2.2.

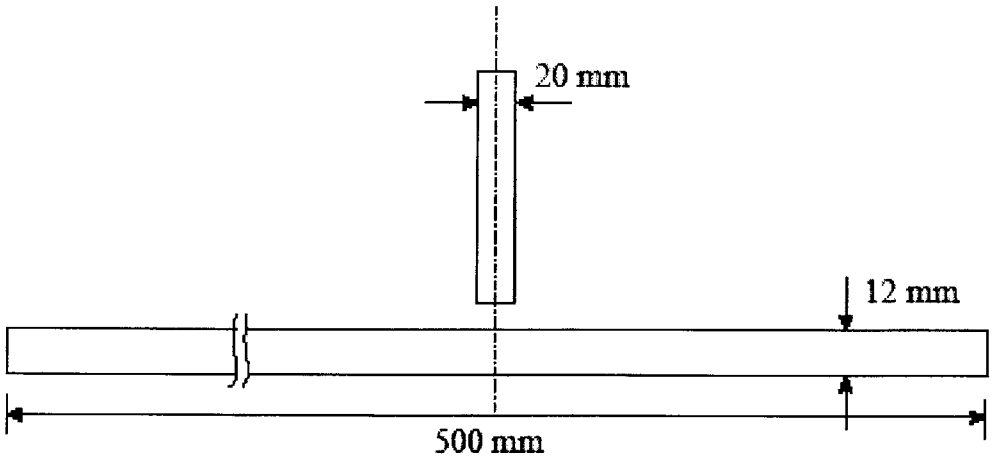

(a) monolithic plate

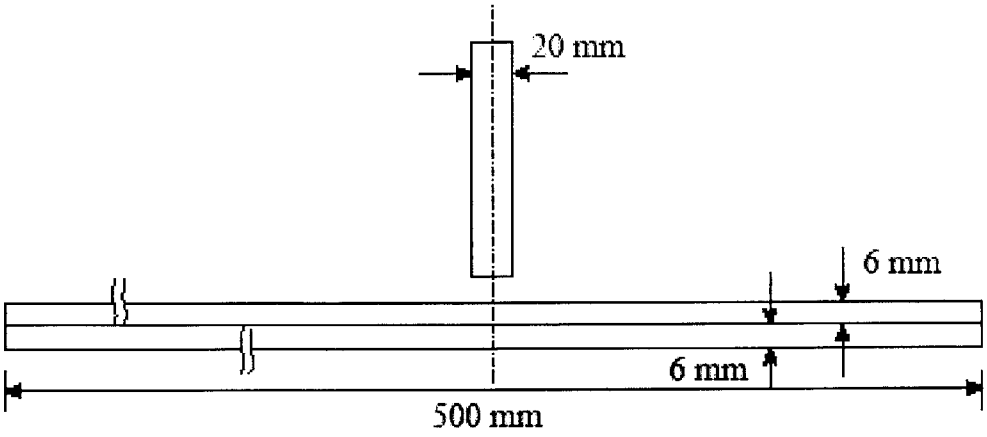

(b) double-layered shield with the plates initially in contact

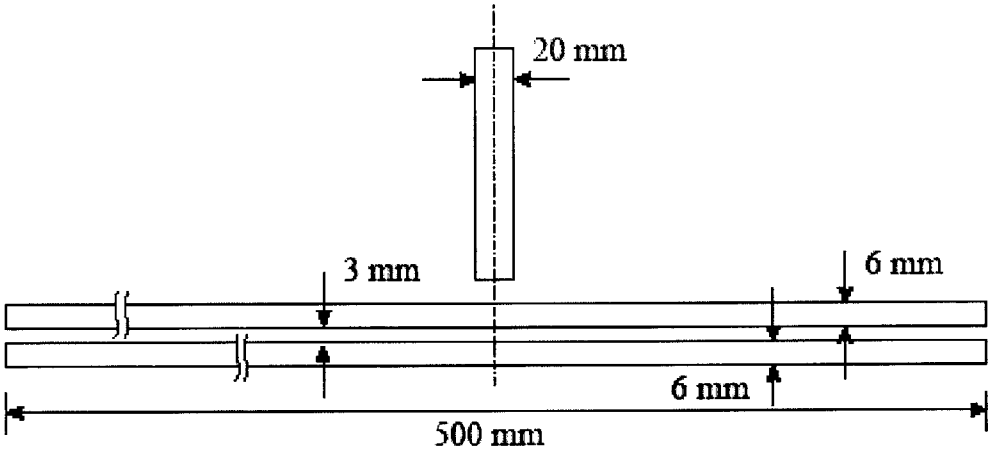

(c) double-layered shield with the plates spaced

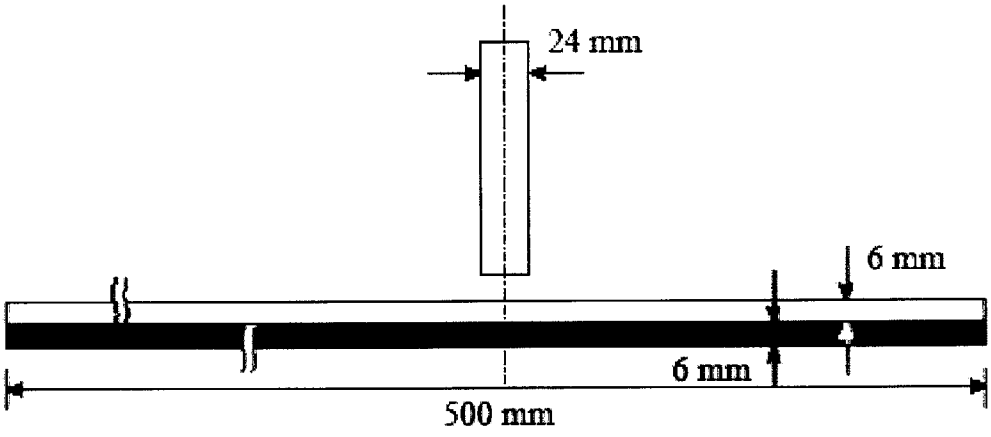

(d) double-layered shield with the plates welded together

Fig. 2.1: Four types of shields considered in this thesis

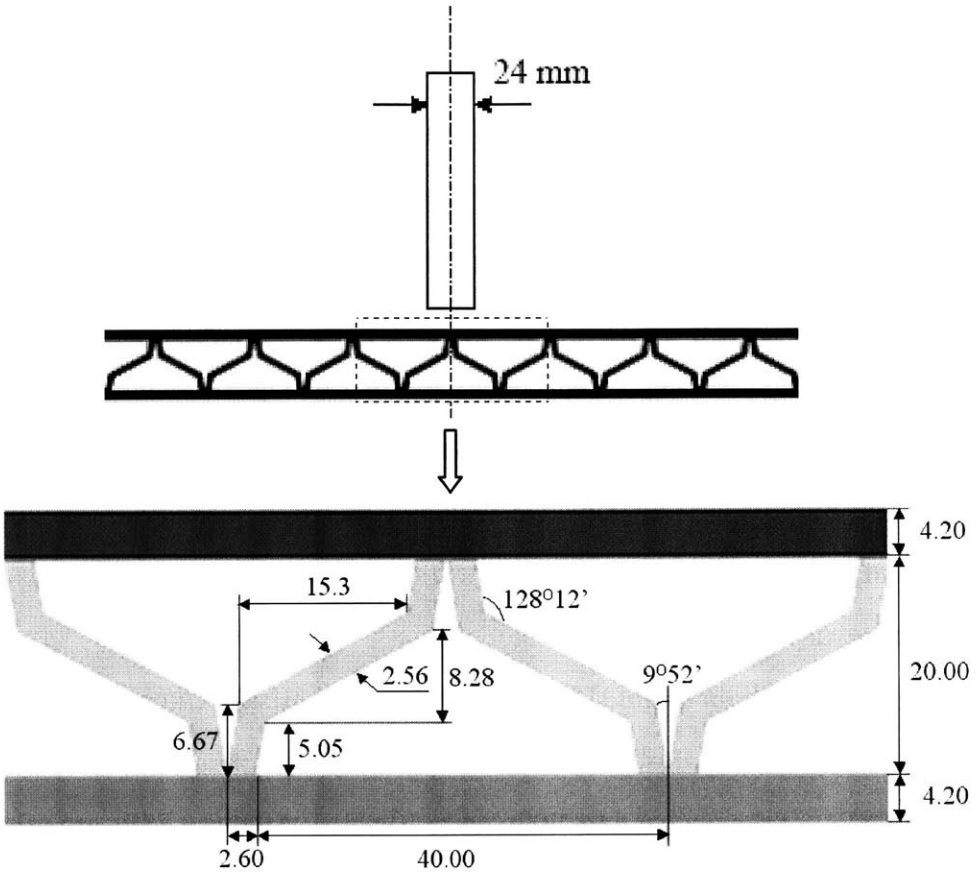

Fig. 2.2: BRAS shield and a detailed geometry (unit: mm)

At first, the case with the monolithic plates will be considered as a reference. The same material is defined for each part of the double-layered shield with the plates initially in contact, the double-layered shields with the plates spaced and the BRAS shield, while two materials of different ductility and strength are also designed for two layers of the double-layered shields. Obviously, compression is the main interaction between two plates, while no tension and limited shear stress due to friction can be transmitted between the plates. In our simulations, the shields are designed to be of circular shape and the equivalent total thickness 12mm. In order to verify our simulation results, the geometrical dimensions of first three types of target shields were taken from the impact tests conducted by Børvik et al. [12].

For the double-layered shields with the plates spaced, the spacing between the two plates is specified to be 3mm. In this distance, the two plates are still able to interact with each other.

For the BRAS shields, the spacing between the two layers is specified to be 20mm, while the thickness of girders is specified to be 2.6mm. These dimensions make the total weight of BRAS shields equivalent to the monolithic plates of the thickness 12mm.

In military and civilian applications, two types of armor-piercing projectiles are often encountered: 7.62mm armor-piercing bullets from rifles or machine guns and fragments generated from Improvised Explosive Devices. The bullets are usually of the weight of about 10g and are of the ogival-nose shape, while the weight and configurations of fragments may vary in a rather wide range.

In order to design light armor shields for perforation resistance against fragments, U.S. military standard MIL-P-46593A specifies three types of Fragment Simulating Projectiles (FSPs) of the weight 44g, 207g,and 830g [15]. All these FSPs are of cylindrical shape and chisel nose. In this thesis, eight types of cylindrical projectiles were considered, see Fig. 2.3. Among these projectiles, there are three weights of different orders of magnitude: 200g, 30g and 10g. Meanwhile, two types of projectile noses were defined: flat-nose and conical-nose, which represent two limiting cases.

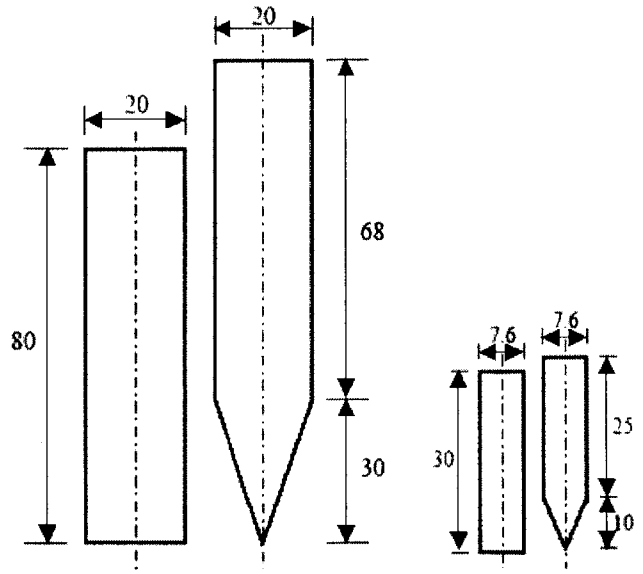

M_0 = 200g M_0 = 10g

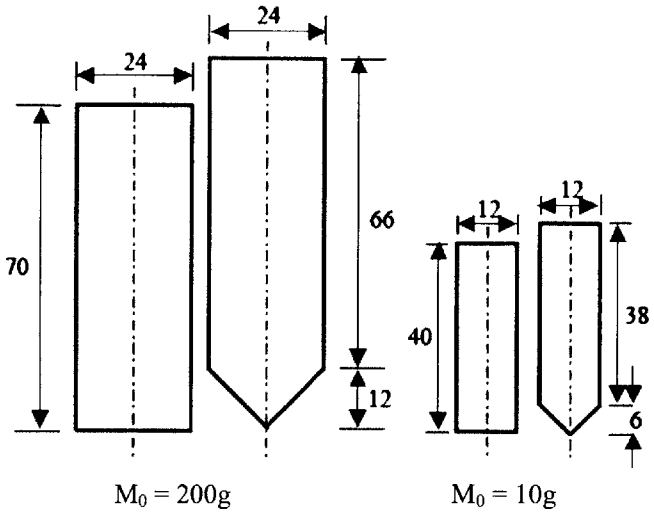

Fig. 2.3: Eight cylindrical projectiles considered in this study (Unit: mm).

There are totally 36 impact scenarios with different combinations of the five metal shields and the eight projectiles. Also, the initial impact velocity of the projectiles varies in a wide range. The perforation resistance of the five shields is studied by comparing their ballistic limits and residual velocities.

Two types of two-dimensional finite element models were generated for each projectile-target shield system. For the case with the monolithic and the double-layered shields, the target shields were modeled using four-node, axisymmetric elements with reduced integration (CAX4R), while for the case with BRAS shields, the model used is four-node, plain strain elements with reduced integration (CPS4R). Figures 2.4-2.6 show the finite element models for the double-layered shields with the plates spaced, the double-layered shields with different material combinations and the BRAS shields. For the double-layered shields with the plates spaced and that with the plates initially in contact, the impacted zone below the projectile was modeled by square elements with the size of 0.1×0.1mm, see Fig. 2.4. For the double-layered shields with different material combinations, the elements size varies from 0.2×0.2mm in the middle impact zone to 0.2×2mm near the out fringe, see Fig. 2.5. For the BRAS shields, the element size of the

impact zone is of 0.2×0.2mm, see Fig. 2.6. As indicated by the early study on mesh size effects, it was found that the numerical simulations based on such an element size agree well with experimental results [16].

For simplicity, the projectiles were considered as undeformable and were simply represented by rigid surfaces in our simulations. In reality, the projectiles would absorb some kinetic energy and may break into pieces under shock wave loading, e.g. see Børvik et al. [17]. Therefore, assuming the projectile to be rigid would underestimate the ballistic limits of the shields.

Also, we have to correctly define the contact conditions between any two bodies because they may interact with each other. For the monolithic plates, the kinematic contact constraint was defined between the projectile and the impacted zone of the target shields. This problem becomes much more complex for the case with the double-layered shields and the BRAS shields. Obviously, the projectiles may sequentially get into contact with each layer and meanwhile the layers may interact with each other. Therefore, two types of contact constraints have to be defined. The kinematic contact constraints were defined between the projectile and each layer, while the penalty contact constraint was defined between the layers. For all the possible contact interfaces, a constant frictional coefficient 0.1 was defined.

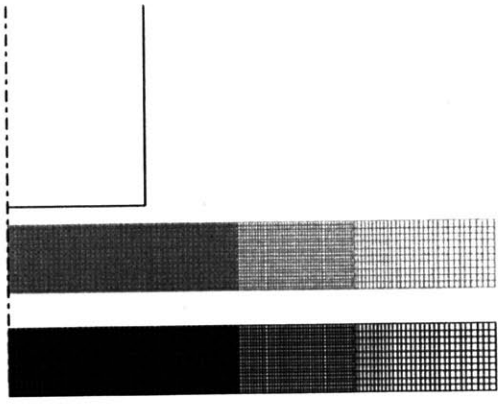

Fig. 2.4: The finite element model of a double-layered shield with the plates spaced impacted by a conical-nose projectile.

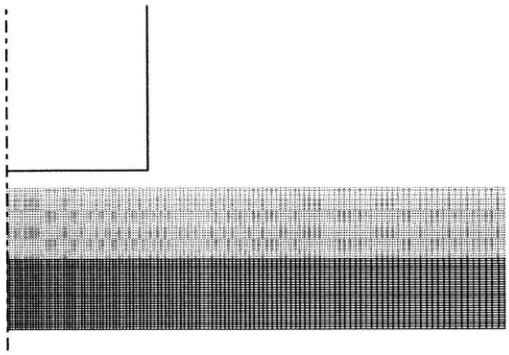

Fig. 2.5: The finite element model of a double-layered shield with different material combinations impacted by a conical-nose projectile.

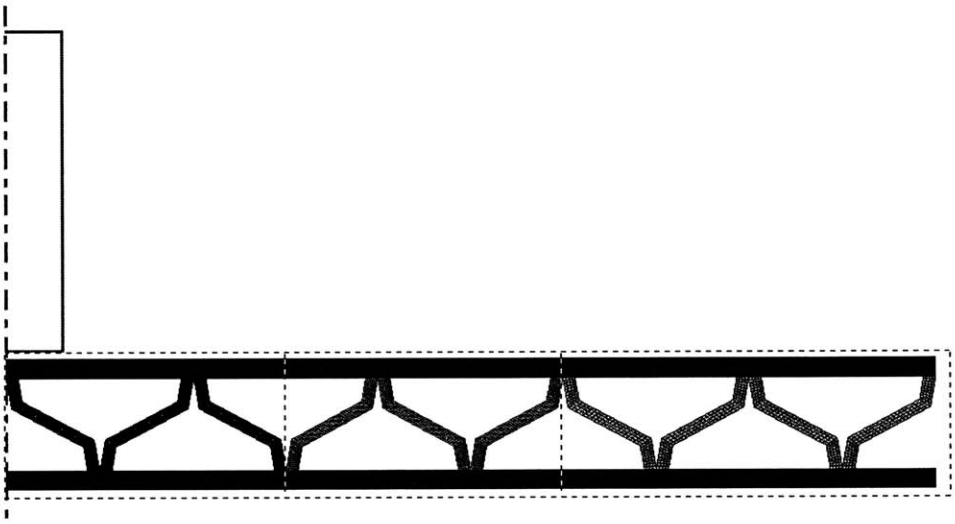

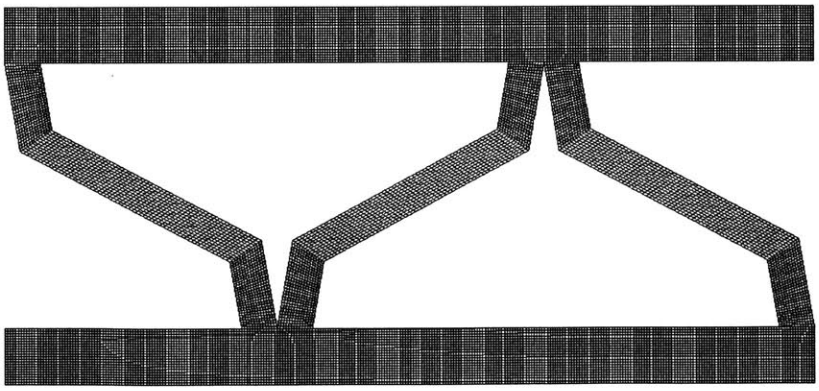

Section (a)
(fine mesh)

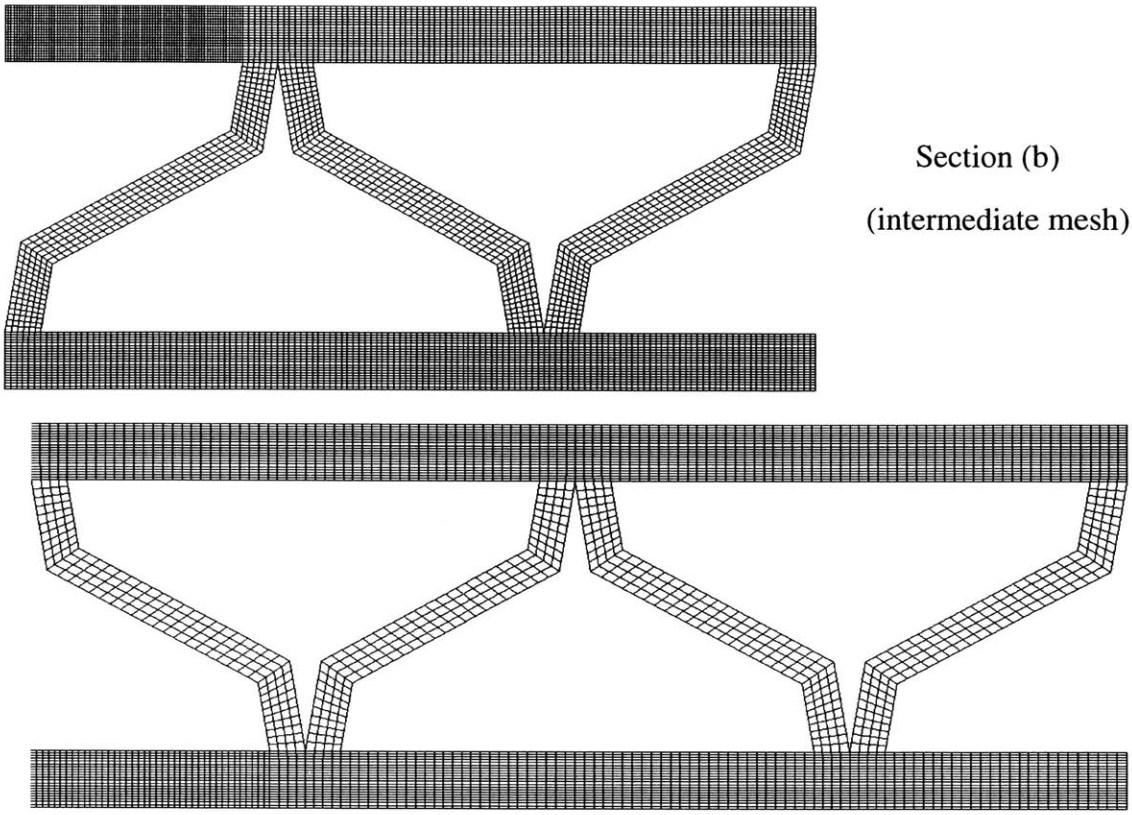

Fig. 2.6: The finite element model of BRAS shield impacted by conical-nose projectile.

2.2 Plasticity and fracture models for tested materials

2.2.1 Weldox 460 E steel

For the double-layered shield with two plates spaced, the double-layered shield with two plates initially in contact and the BRAS shield, the target shields were assumed to be made of Weldox 460 E steel. As a class of rolled steels manufactured by SSAB, Sweden, Weldox steel is of high strength and of outstanding ductility. To study the mechanical properties of Weldox 460 E steel, a series of tensile tests were conducted by Børvik et al. [18, 19]. In this thesis, the material constitute model proposed by Johnson and Cook [20] was used to describe the behaviors of Weldox 460 E steel under dynamic loading. The hardening rule including effects of the strain rates and temperature change is defined by

$$\bar{\sigma} = \left[A + B\bar{\varepsilon}_{pl}^{n}\right]\left[1 + C\ln\left(\frac{\dot{\bar{\varepsilon}}_{pl}}{\dot{\bar{\varepsilon}}_{0}}\right)\right]\left[1 - \left(\frac{T - T_0}{T_m - T_0}\right)^{m}\right] \tag{1}$$

where $\bar{\sigma}$ is the von Mises stress; $\bar{\varepsilon}_{pl}$ is the effective plastic strain; A, B, n, C, and m are five material constants which need to be calibrated from tests; $\dot{\bar{\varepsilon}}_{pl}$ and $\dot{\bar{\varepsilon}}_{0}$ are the current and reference strain rate; T_m and T_0 are the melting and room temperature; respectively. All the relevant material constants for Weldox 460 E steel are shown in Table 2.1.

E (GPa)	v	ρ (kg/m^3)	$\dot{\bar{\varepsilon}}_0$ (s^{-1})	C
200	0.33	7850	5.00×10^{-4}	0.0123
c_v (J/kgK)	T_m (K)	T_0 (K)	m	A (MPa)
452	1800	293	0.94	490
B (MPa)	n	D_1	D_2	D_3
383	0.45	0.0705	1.732	-0.54

Table 2.1: Material constants for Weldox 460 E steel

To predict the material failure, a ductile fracture model was formulated by the equivalent plastic strain to fracture $\bar{\varepsilon}_f$ and the stress triaxiality η, which is defined by the ratio of the mean stress σ_m to the equivalent stress. The damage indicator D can be written as

$$D = \int_0^{\bar{\varepsilon}_f} \frac{1}{\bar{\varepsilon}_f(\eta)} d\bar{\varepsilon}_{pl} \tag{2}$$

A material point is considered to fail when $D \geq 1.0$. The failed elements completely lose their load-carrying capability and are removed from the rest of the calculation. This fracture criterion was first suggested by Johnson and Cook [21] and was incorporated into our simulations. Also, Johnson and Cook suggested an exponential relationship between the effective plastic strain and the stress triaxiality:

$$\bar{\varepsilon}_f = D_1 + D_2 \exp(D_3 \eta) \tag{3}$$

where D_1, D_2, and D_3 denotes three material coefficients. Based on a series of tensile tests on round bars, Børvik et al. [18, 19] obtained test data for Weldox 460 E steel: $D_1 = 0.0705$, $D_2 = 1.732$, and $D_3 = -0.54$. Actually, Johnson-Cook fracture loci calibrated from tensile tests were often extrapolated to the range of negative stress triaxialities in practical applications. Note that the ductility of materials under compression may be underestimated due to extrapolation. Here, the Johnson-Cook fracture locus was modified by introducing a cut-off value for the negative stress triaxiality at -1/3, see Fig. 2.7. The concept of the cut-off value was first introduced by Bao and Wierzbicki [22] to describe the sharp increase of the ductility of materials under compression. As demonstrated by Teng and Wierzbicki [11, 23], the cut-off value has a critical effect on the reconstruction of various fracture patterns in a number of high velocity impact problems.

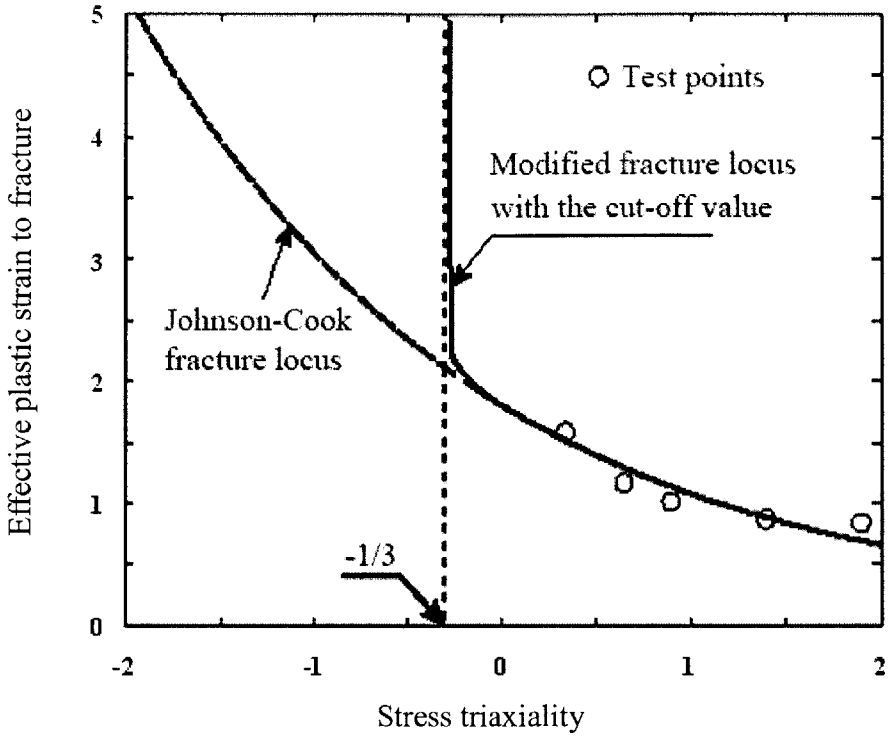

Fig. 2.7: Fracture loci for Weldox 460 E steel

2.2.2 Domex Protect 500 steel

It is known that ductility and strength is two incompatible properties for traditional materials. High ductility always accompanies with low strength, and vice versa. It can be seen from Fig. 2.8, the trade off between strength and ductility of materials. Here two parameters, C_1 and C_2, are defined to facilitate our explanations. C_1 and C_2 are the scaling parameter of stress-strain curves and fracture strain respectively. Figure 2.9 shows the varies stress-strain curves with the same fracture strain, while Fig. 2.10 shows the same stress-strain curves with varies fracture strains. The meaning of C_1 and C_2 can be easily understood from Fig. 2.9 and 2.10. Also, the trade off between strength and ductility can be rewrote using scaling parameter C_1C_2 = const, see Fig. 2.11.

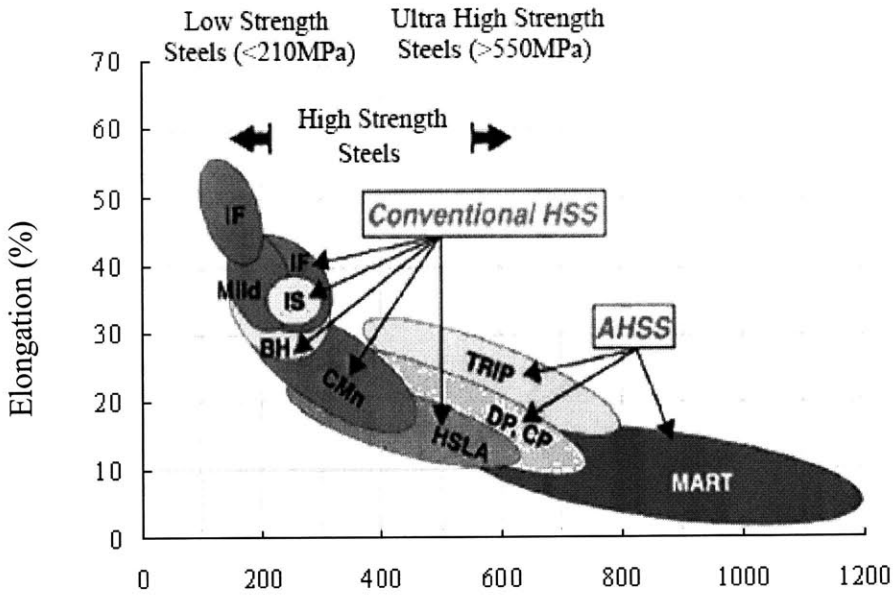

Fig. 2.8: Trade off between strength and ductility

$$\bar{\sigma} = C_1 f\left(\bar{\varepsilon}_{pl}\right)$$

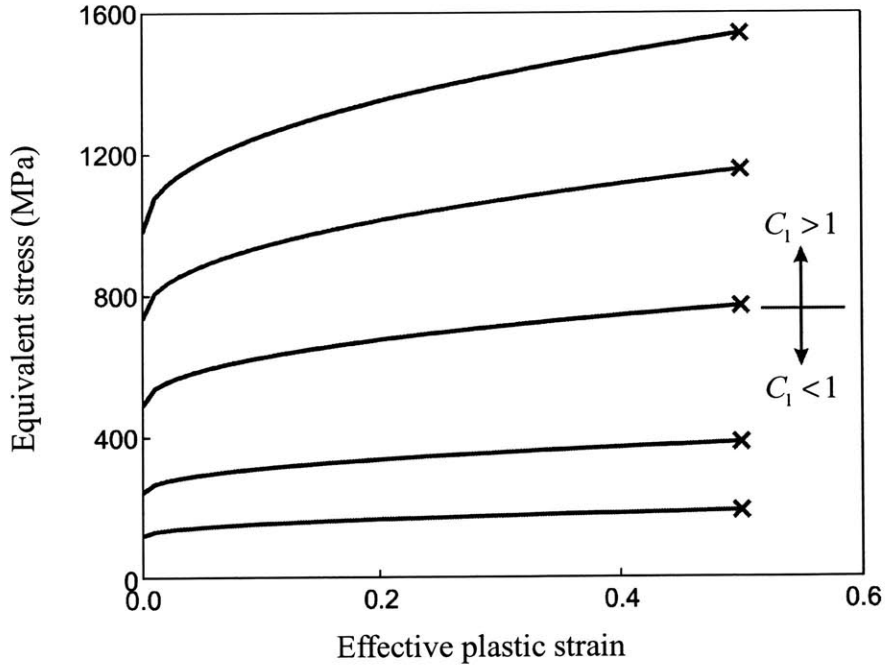

Fig. 2.9: Various stress-strain curves with the same fracture strain.

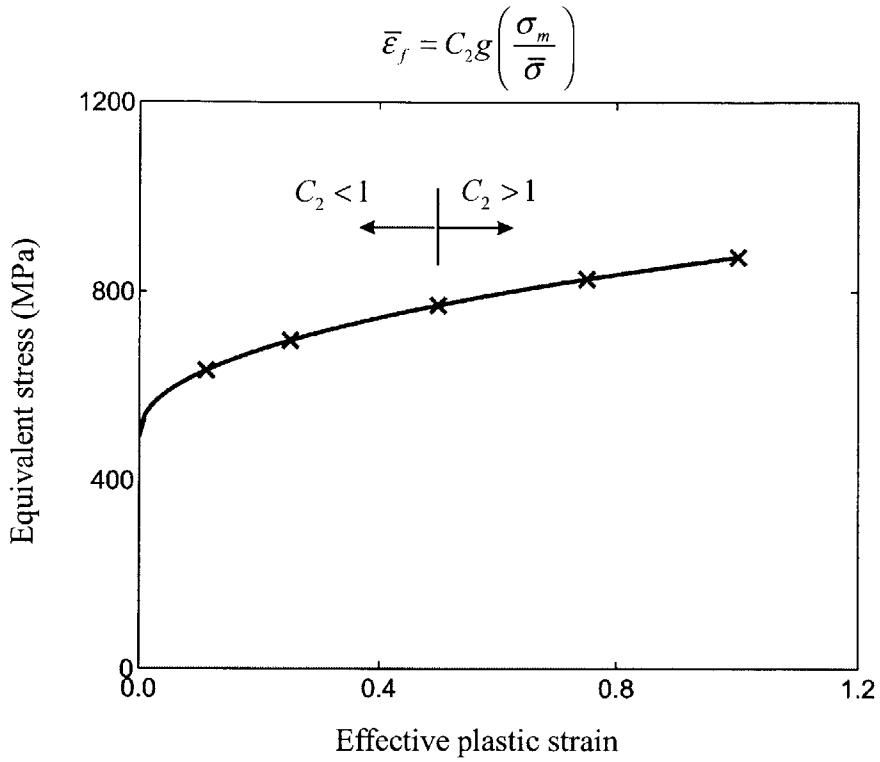

Fig. 2.10: The same stress-strain curves with various fracture strains.

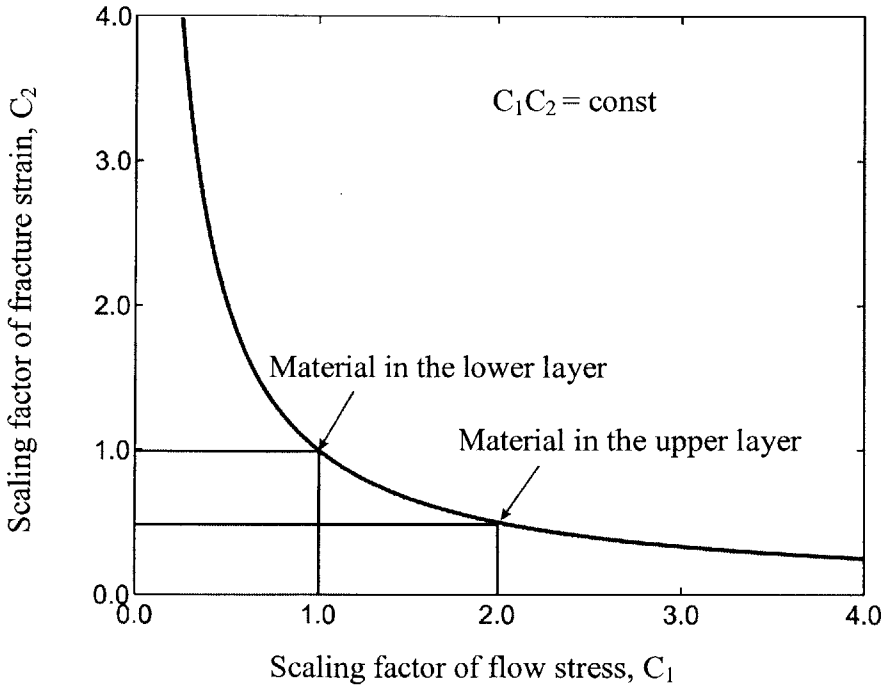

Fig. 2.11: Relation between flow stresses and fracture strains

The perforation resistance of the monolithic plates varies with the stress-strain curve and fracture strain of materials. At first, the fracture strain is maintained to be the same, while the stress-strain curve is scaled with the base line stress-strain curve. Figure 2.12 shows the time history of the transient velocity of the projectile impacts at the target with materials of different stress-strain curve and the same fracture strain. Another condition is scaling up the fracture strain and maintaining the stress-strain curve the same. Figure 2.13 shows the time history of the transient velocity of the projectile impacts at the target with materials of different yield strength and the same stress-strain curve. The plot of the normalized residual velocities of the projectile vs. the scaling parameters C_1 and C_2 is shown in Fig. 2.14.

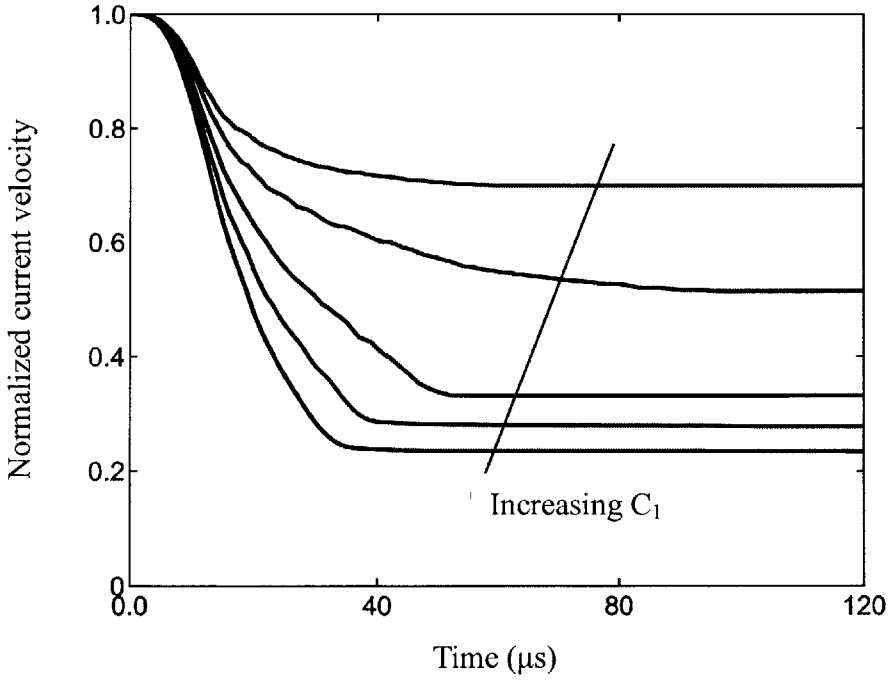

Fig. 2.12: Time history of the transient velocity of the projectile impacts at the target with materials of different stress strain curve

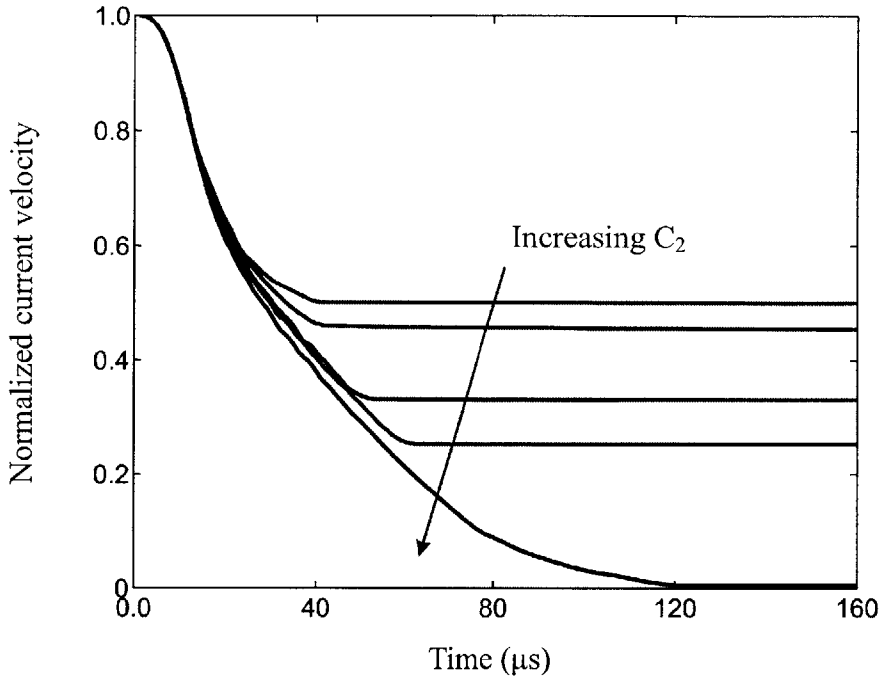

Fig. 2.13: Time history of the transient velocity of the projectile impacts at the target with materials of different yield strength

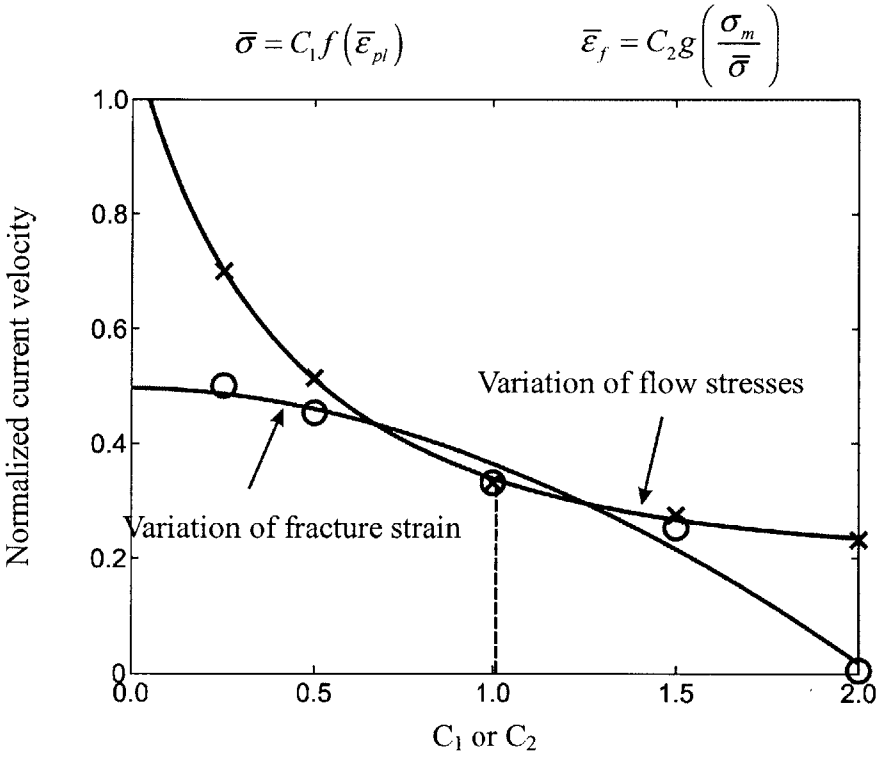

Fig. 2.14: Residual velocities vs. scaling parameters of yield strength and fracture strain

In order to study the optimization effect of ductility and strength on perforation resistance, besides Weldox 460 E steel, another grade of metal of higher ductility and lower strength is used as the material for the double-layered shields. If the Weldox 460 E steel is considered as the base material, the modified material Domex Protect 500 steel can be introduced by scaling up twice the base line stress-strain curve and scaling down the base line fracture locus by half, i.e. $C_1 = 2$, $C_2 = 0.5$. Figure 2.15 shows the true stress-strain curve of two types of armor steels studied in this thesis. In the following discussions, the high ductility material is represented by white box, while the low ductility material is represented by black box, see Fig. 2.15.

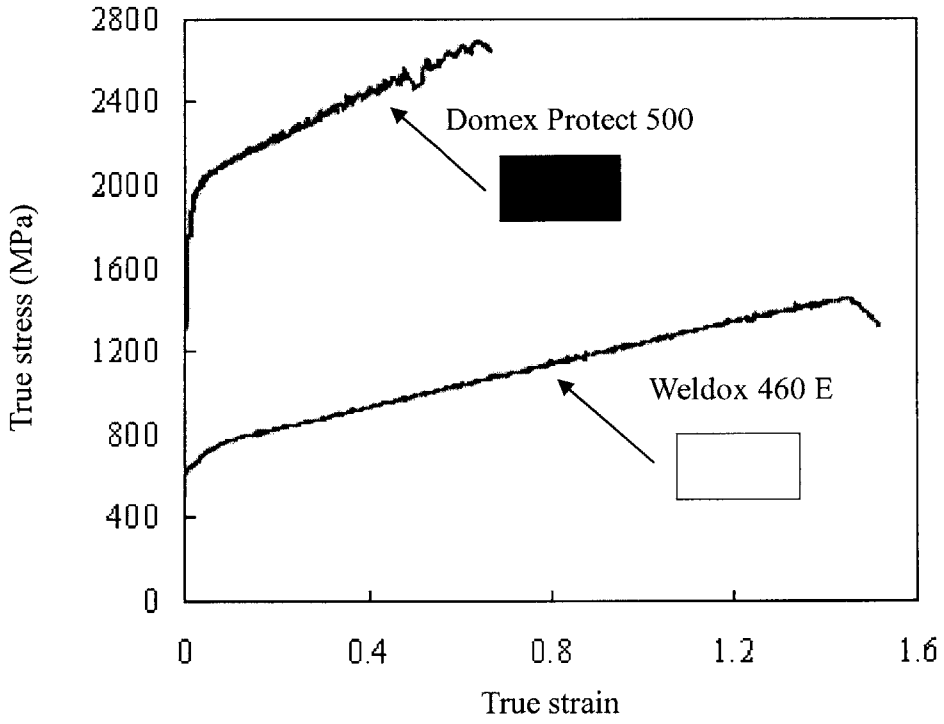

Fig. 2.15: The true stress-strain curve of two types of armor steels studied in this thesis

Chapter 3
Ballistic Resistance of the Double-layered Shields with Two Plates Spaced and in Contact

3.1 Heavy flat-nose projectile

In this section, the heavy flat-nose projectile is considered as the striker.

The first type of shield studied is the monolithic plate. Figure 3.1 shows a typical perforation process of the monolithic plate impacted by the heavy flat-nose projectile at V_0 = 285.4m/s. It can be observed that shear plugging is the predominant failure mode for the monolithic target under normal impact by this projectile. The sharp corner of flat-nose projectile often induces crack formation and propagation through the shield thickness. Also, it was found that the target plate undergoes insignificant global deformation even at the impact velocity near the ballistic limit. The whole impacted zone beneath the projectile is ejected as a plug. In order to verify the correctness of the numerical simulation, some of the initial impact velocities in section 3 were selected to be identical to those in the impact test performed by Børvik et al. [12].

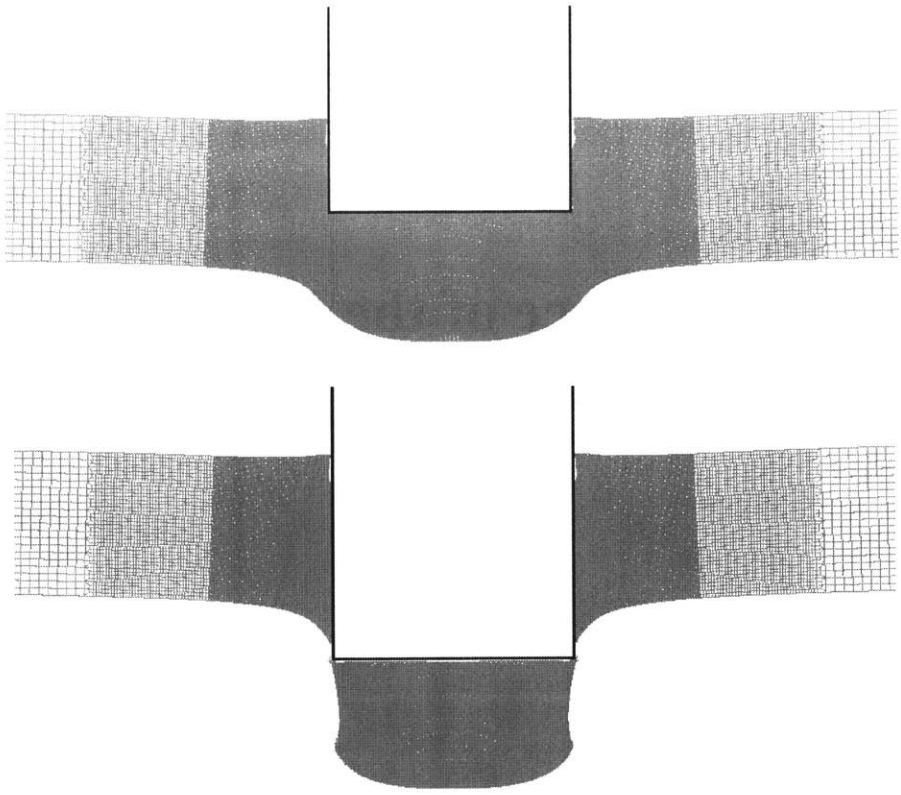

Fig. 3.1: The perforation process of the monolithic plate impacted by the heavy flat-nose projectile at $V_0 = 285.4$m/s.

The second type of shield considered is the double-layered shield with the plates in contact. Figure 3.2 shows the perforation process of the double-layered shield with the plates initially in contact impacted by the heavy flat-nose projectile at $V_0 = 285.4$m/s. Similar to the case of monolithic shied, the upper plate tends to fail by shear plugging and the plastic deformation is localized in the impacted zone. However, the failure mode of double-layered shield is different from that of monolithic plate. It is found that the deformation region of the lower plate extends well beyond the impacted zone. Also, thinning before fracture can be clearly observed in the lower plate. Another difference from the monolithic plate is the pattern of crack formation and propagation. For the monolithic target, one single crack continuously grows through the whole thickness during the perforation process, while two separate cracks have to be formed for each part

in the double-layered shields. Generally speaking, crack initiation requires more energy dissipation than crack propagation.

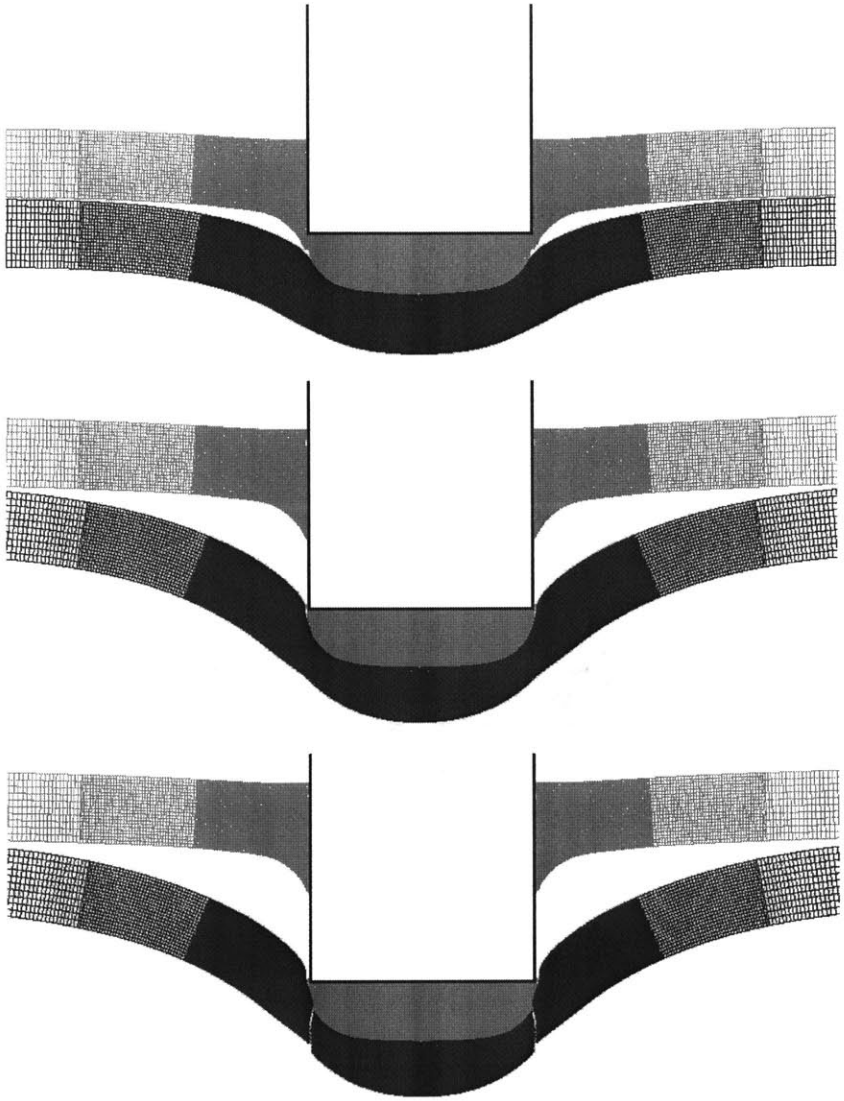

Fig. 3.2: The perforation process of the double-layered shield with the plates initially in contact impacted by the heavy flat-nose projectile at $V_0 = 285.4$m/s.

The third type of shield considered is the double-layered shield with the plates spaced. Figure 3.3 shows the perforation process of the double-layered shield with the plates spaced impacted by the heavy flat-nose projectile at $V_0 = 285.4$m/s. In this case,

the upper plate suffers large bending deformation before contacting with the lower plate. It can be observed that the lower plate undergoes deep necking before failure. Tensile tearing is the dominating failure mode for both plates in this case.

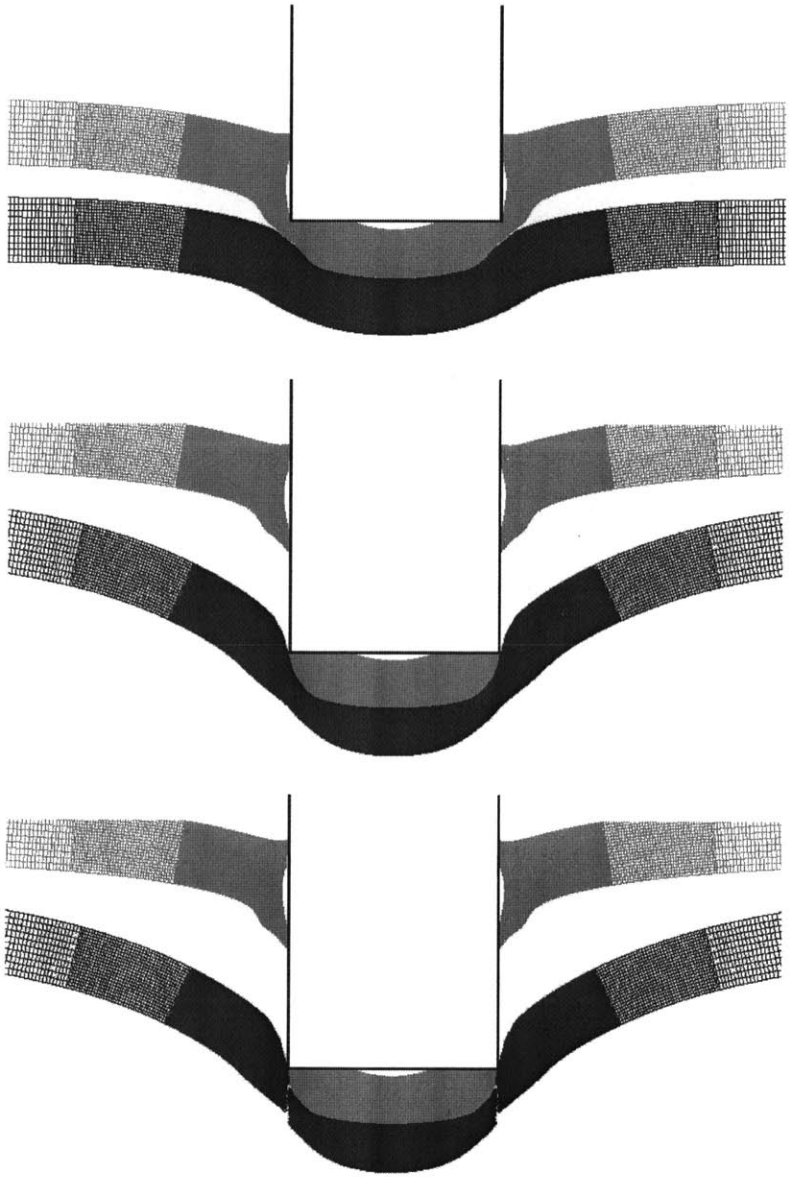

Fig. 3.3: The perforation process of the double-layered shield with the plates spaced impacted by the heavy flat-nose projectile at V_0 = 285.4m/s.

It can be concluded from the comparison that the transition of the failure mode from shear plugging in the monolithic plate to tensile tearing in the double-layered shield is accompanied with a considerable increase in plastic energy dissipation, particularly for the lower plate. In general, tensile tearing involves a larger deformed zone than shear plugging under the same impact condition. Figure 3.4 shows the time history of the plastic energy dissipation of the upper and lower plates among the three types of shields. The plastic energy absorbed by the lower plate of the double-layered shield with the plates spaced is almost twice as high as that absorbed by the corresponding part of the monolithic plate.

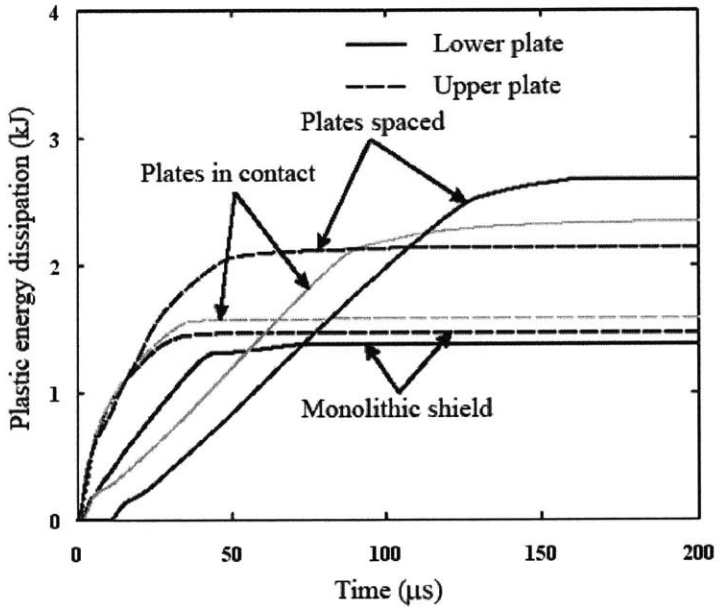

Fig. 3.4: The time history of plastic energy dissipation of the three types of shields impacted by the heavy flat-nose projectile at V_0 = 285.4m/s
(For the monolithic plate, the plastic energy for the upper and lower half was output separately.).

Apparently, large energy dissipation leads to low residual velocities of the projectile in the case with the double-layered shields. The residual velocity of the projectile vs. the initial impact velocity among all the three cases is plotted in Fig. 3.5. It can be observed

that, as the impact velocity approaches the ballistic limit, the double-layered shields become superior in resisting perforation over the monolithic plate. The ballistic limits of the three types of shields impacted by the heavy flat-nose projectile are given in Table 3.1. By replacing the monolithic plate with the double-layered shields of the same total thickness, the ballistic limit of the shield is improved by about 25.0%. This conclusion is confirmed by the impact tests conducted by Dey et al. [6]. According to test results, the double-layered shield was able to increase the ballistic resistance by about 30%. The present numerical prediction is also consistent qualitatively with Corran et al.'s test results [2] but contradicts to Radin and Goldsmith's test outcomes [3]. As Corran et al. [2] pointed out, the double-layered shield would become more effective than the monolithic plate as the total thickness exceeded a critical value. Note, that the thickness of the shields studied by Radin and Goldsmith ranges from 1.6mm to 6.4mm, which is much smaller than the present case.

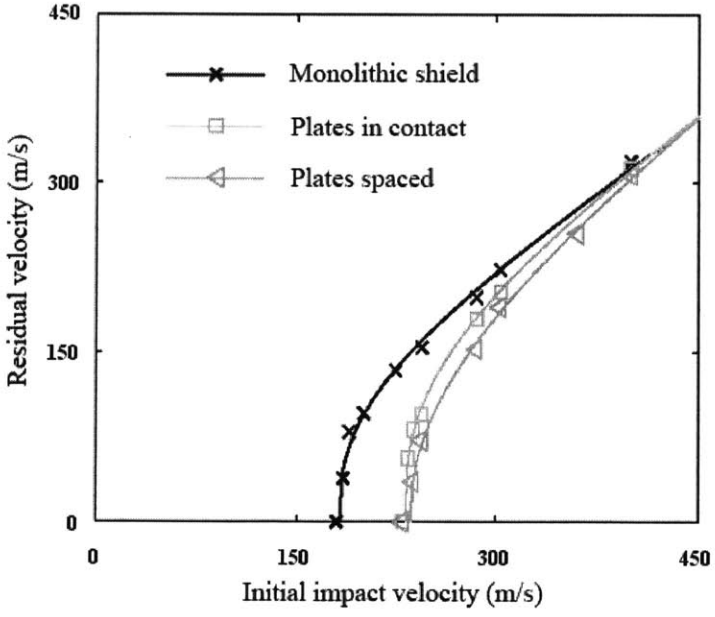

Fig. 3.5: The initial impact velocity vs. the residual velocity for the three types of shields impacted by the heavy flat-nose projectile.

Monolithic plate	Double-layered shield with the plates in contact	Double-layered shield with the plates spaced
186.1 (1.00)	232.0 (1.25)	236.0 (1.27)

Table 3.1: The ballistic limits of the shields impacted by the heavy, flat-nose projectile (unit: m/s)

For the double-layered shields, it can also be concluded from Fig. 3.3 that an increase in the spacing between the two plates improves only the ballistic resistance. However, this conclusion is contrary to the test results obtained by Marom and Bodner [1]. As they point out, the beams in contact always have higher ballistic limits than the beams spaced. Note that in their study the beams were so widely separated that there was actually no interaction between two beams during the perforation process, while in the present case, the two plates in the double-layered shields strongly interact with one another. This contradiction indicates that there may exist an optimal spacing for the ballistic resistance of the double-layered shield.

3.2 Heavy conical-nose projectile

In the previous section, the surface contact between the projectile and the shield was assumed. Actually, it is more likely that the sharp corner of a projectile may first pierce a shield. This type of perforation scenario is represented by introducing the heavy conical-nose projectile.

Figures 3.6-3.8 show the perforation processes of the three types of shields impacted normally by the conical-nose projectile. For the double-layered shield with the plates initially in contact, the lower plate experiences considerable bending deformation compared with the upper plate. The two plates, which are initially in contact, are separated clearly during the perforation process. Among the three cases, the materials in the impacted zone are pushed aside as the projectile penetrates through the thickness. During the perforation process, no clear sign of crack formation and propagation is found. The failure mode for all three types of shields is a ductile hole enlargement, independent of the impact velocity. Therefore, the introduction of the double-layered shield does not induce the transition of the failure mode for the heavy conical-nose projectile. This is different from the preceding case with the heavy flat-nose projectile.

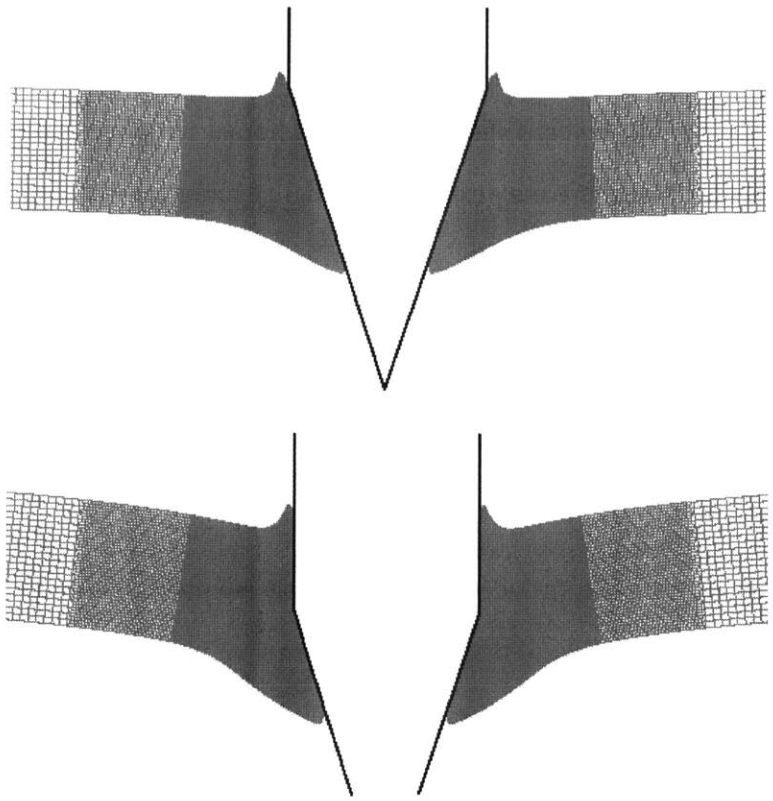

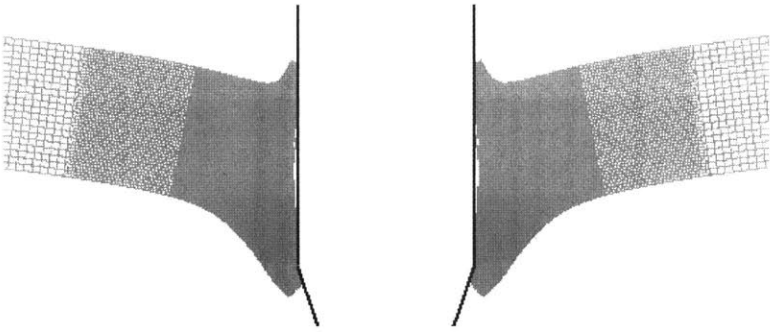

Fig. 3.6: The perforation process of the monolithic plate impacted by the heavy conical-nose projectile at $V_0 = 317.9$m/s.

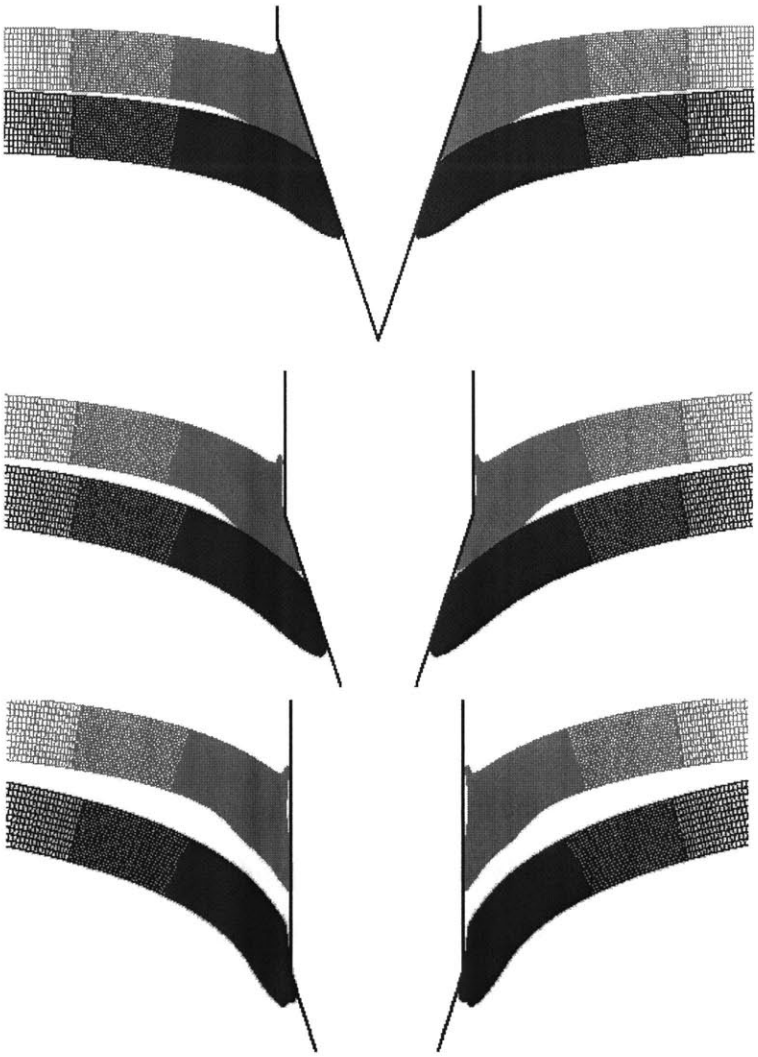

Fig. 3.7: The perforation process of the double-layered shield with the plates initially in contact impacted by the heavy conical-nose projectile at $V_0 = 317.9$m/s.

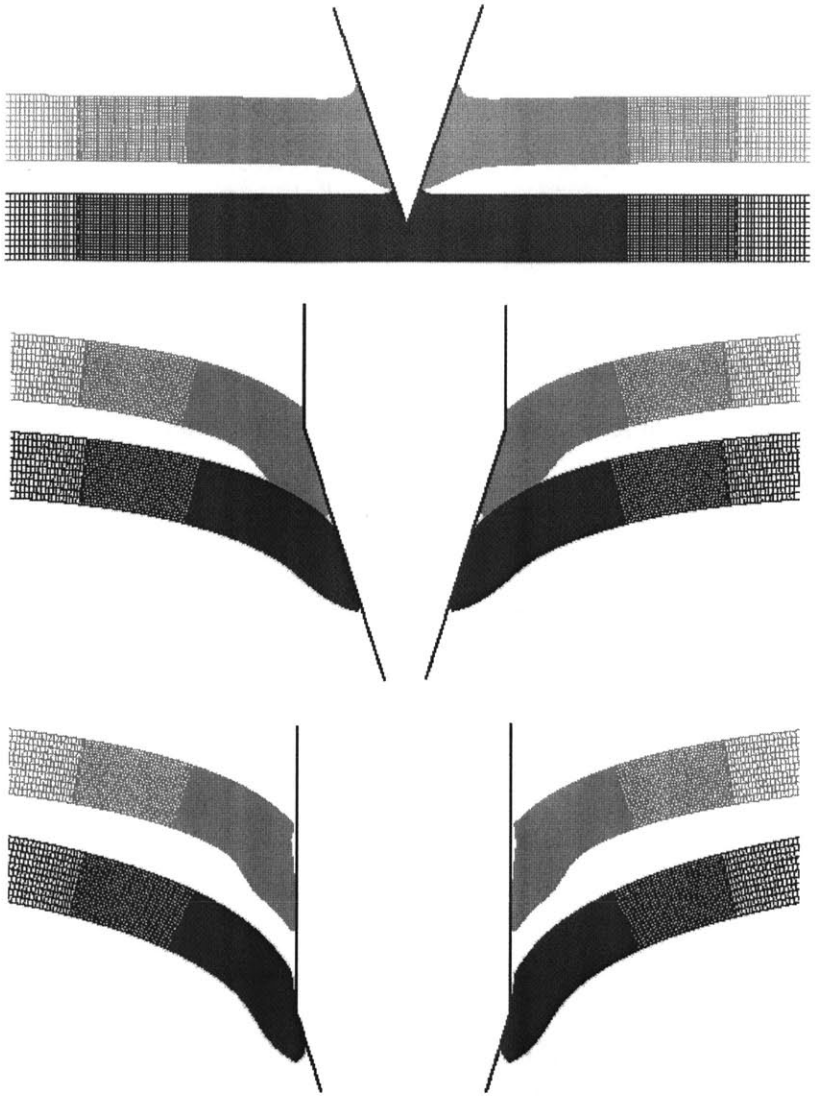

Fig. 3.8: The perforation process of the double-layered shield with the plates spaced impacted by the heavy conical-nose projectile at $V_0 = 317.9$m/s.

Figure 3.9 shows the plots of the initial impact velocity vs. the residual velocity for the three types of shields. Apparently, the predicted residual velocities for the double-layered shields are always higher than those for the monolithic plate. Since neither large shear nor tensile stresses can be transferred between the two plates of the double-layered shield, its shear resistance is weakened. This should be the reason for the 8.0% decrease in the ballistic limits compared to the monolithic plate, see Table 3.2. This

conclusion agrees with the test results obtained by Radin and Goldsmith [3], Almohandes et al. [4], and Dey et al. [6].

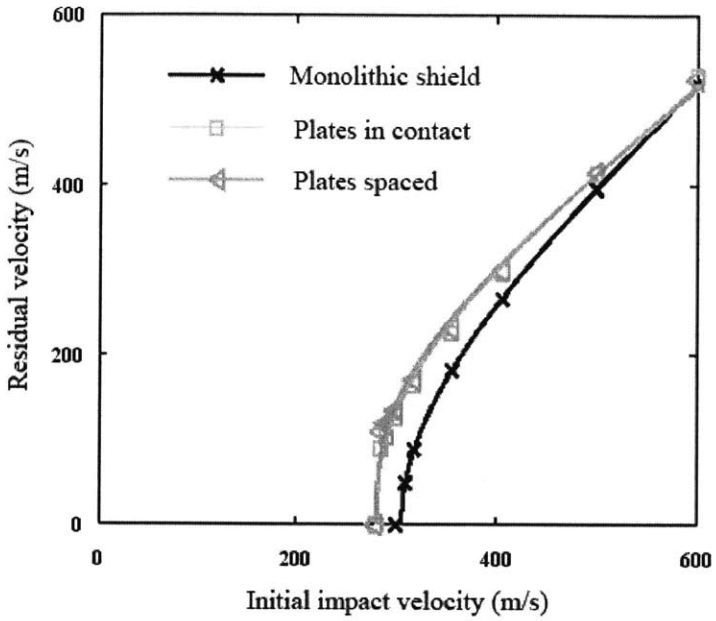

Fig. 3.9: The initial impact velocity vs. the residual velocity for the three types of shields impacted by the heavy conical-nosed projectile

Monolithic plate	Double-layered shield with the plates in contact	Double-layered shield with the plates spaced
305.9 (1.000)	282.0 (0.992)	280.0 (0.915)

Table 3.2: The ballistic limits of the shields impacted by the heavy, conical-nose projectile (unit: m/s)

According to our simulation results, the predicted residual velocities for the double-layered shield with the plates in contact are a little higher than those with the plates spaced. However, the difference is so small that it is difficult to discern in Fig. 3.9. Again, the results here agree with the observations by Almohandes et al. [4] and Dey et

al. [6]. Therefore, it may be concluded that an increase in the spacing between the two plates would not considerably improve the ballistic resistance of double-layered shields.

3.3 Light flat-nose projectile

The projectile considered in this section is a flat-nose projectile of the mass $M_0 = 10g$ and the diameter d = 7.6mm. This striker is close in size to the smallest Fragment Simulating Projectile (FSP) of 0.30'' caliber specified in Military Standard MIL-P-46593A [15]. Since the projectile is relatively light, a high initial impact velocity is required to completely perforate the shield. This leads to a different failure mode from shear plugging or tensile tearing.

Figure 3.10 shows the perforation process of the monolithic plate at $V_0 = 600m/s$. It can be observed that the materials in the impacted zone beneath the projectile are pushed aside and a cavity, whose diameter is larger than that of the projectile, is formed. In contrast, at a low initial impact velocity the cavity is of almost the same diameter through the target thickness, e.g. see Fig. 3.1. As the projectile approaches the bottom surface of the shield, shear plugging becomes the predominant failure mode and a plug of reduced thickness is ejected. Although the combined action of tension and shear is observed in the later process, ductile hole enlargement should be the dominating failure mode. Cavity formation contributes a large part of plastic energy dissipation. In contrast, in the case with the heavy flat-nose projectile, shear plugging is always observed in the monolithic plate and the ejected plug is of almost the same diameter as the original plate.

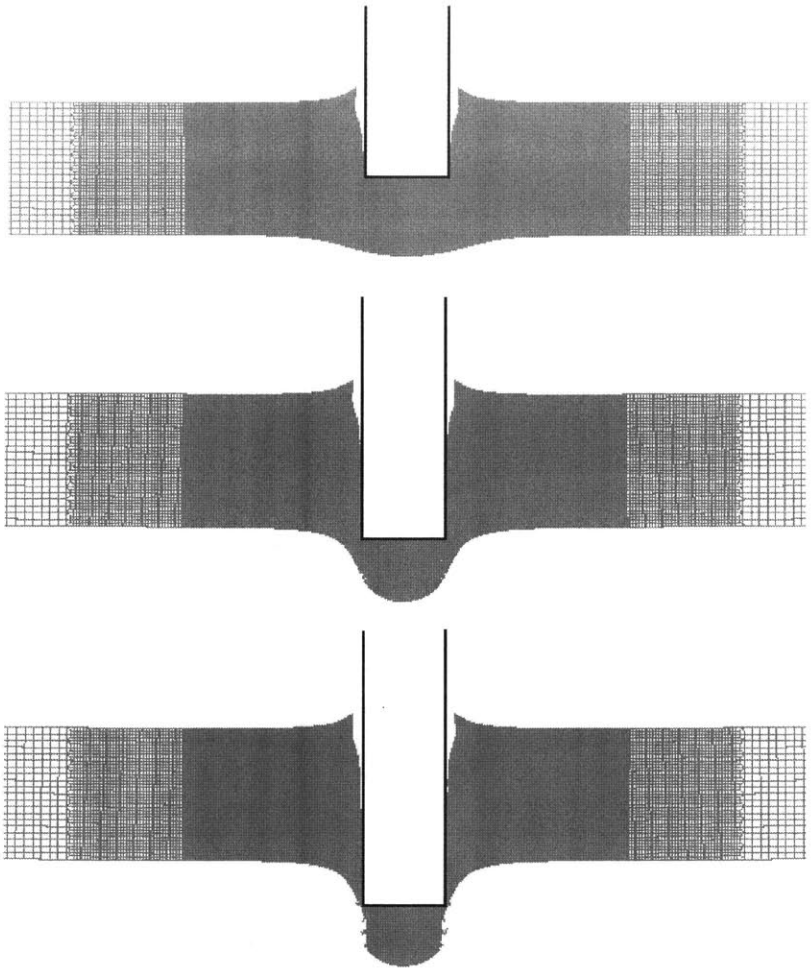

Fig. 3.10: The perforation process of the monolithic plate impacted by the light flat-nose projectile at V_0 = 600.0m/s.

Figure 3.11 shows the perforation process of the double-layered shield with the plates initially in contact impacted by the light flat-nose projectile at V_0 = 600m/s. It can be observed that the dominating failure mode of the upper plate is ductile hole enlargement, this is similar to the monolithic plate. However, the lower plate experiences small bending deformation and necking is observed clearly before fracture. Apparently, the failure mode of the case with the plates spaced is similar to that with the plates initially in contact, see Fig. 3.12.

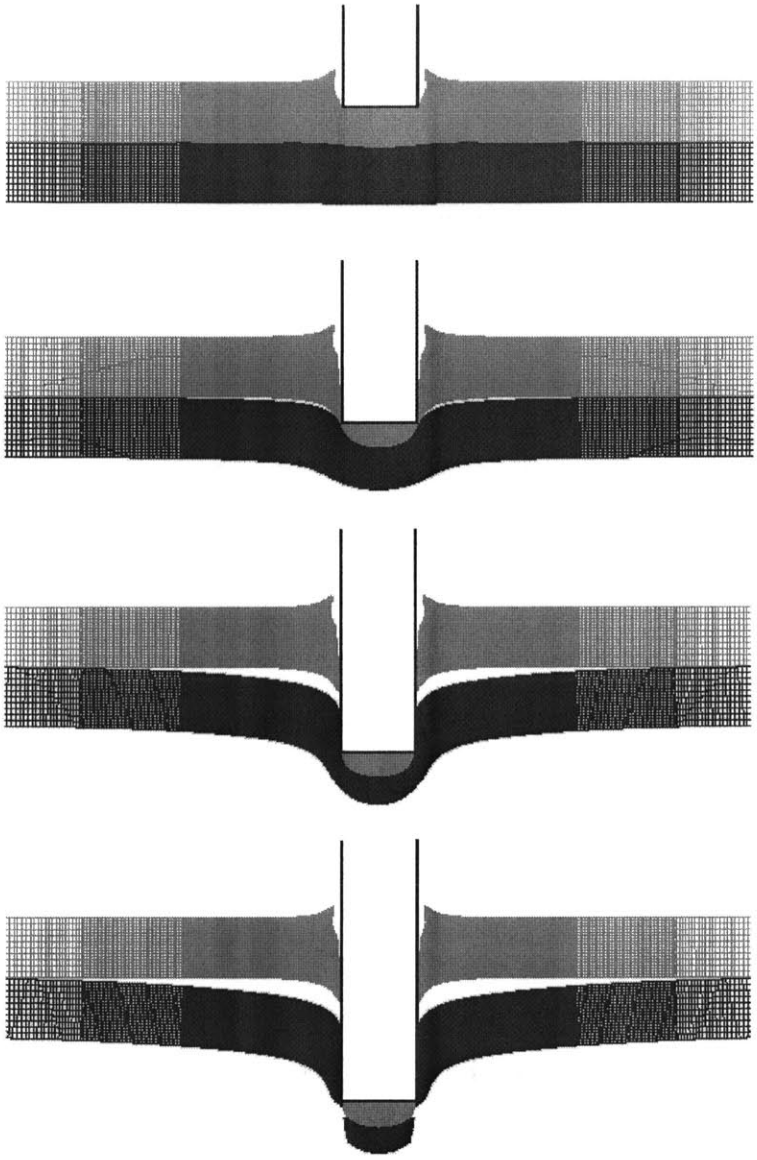

Fig. 3.11: The perforation process of the double-layered shield with the plates initially in contact impacted by the light flat-nose projectile at V_0 = 600.0m/s.

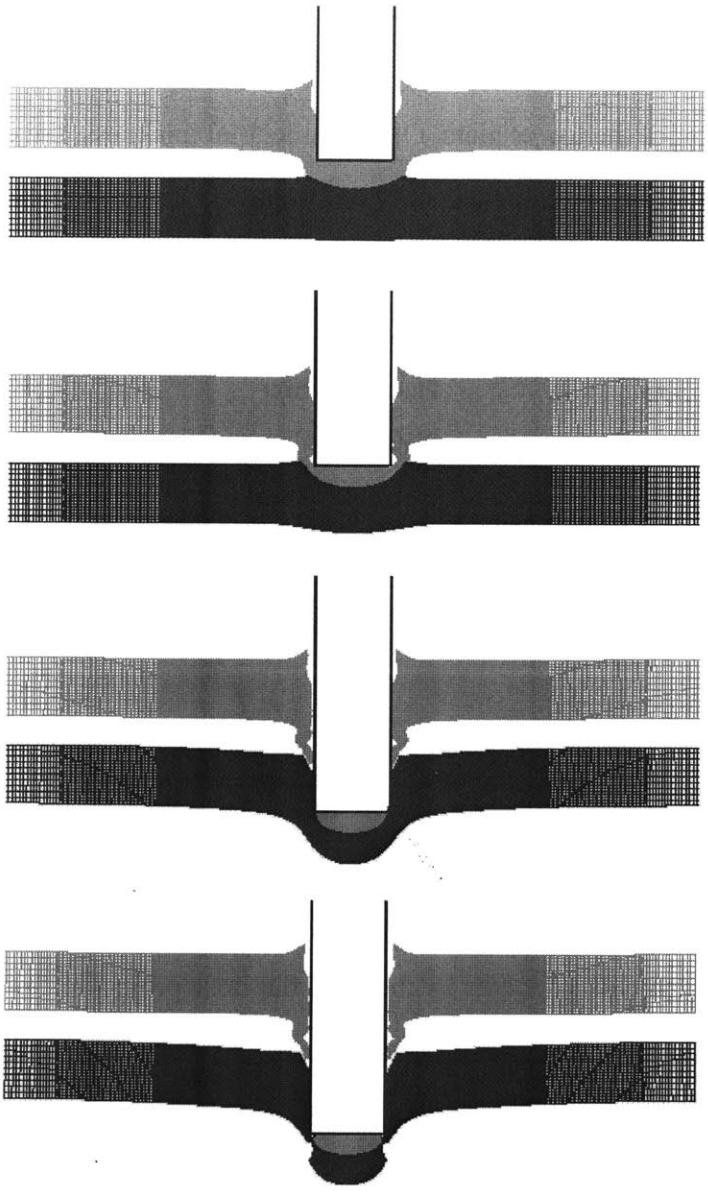

Fig. 3.12: The perforation process of the double-layered shield with the plates spaced impacted by the light flat-nose projectile at $V_0 = 600.0$m/s.

Figure 3.13 shows the plots of the initial impact velocity vs. the residual velocity for the three types of shields. As the initial impact velocity approaches the ballistic limit, the advantage of the double-layered shields over the monolithic plate becomes smaller. According to our results, the ballistic limits of the double-layered shields are higher by

about 7.0% than that of the monolithic plate, see Table 3.3. The reason for increase in the ballistic limit of the double-layered shields should be attributed to the increase in the bending deformation of the lower plate. Of the same total thickness, the detail bending stiffness of the double-layered shield is only one quarter of that of the monolithic plate.

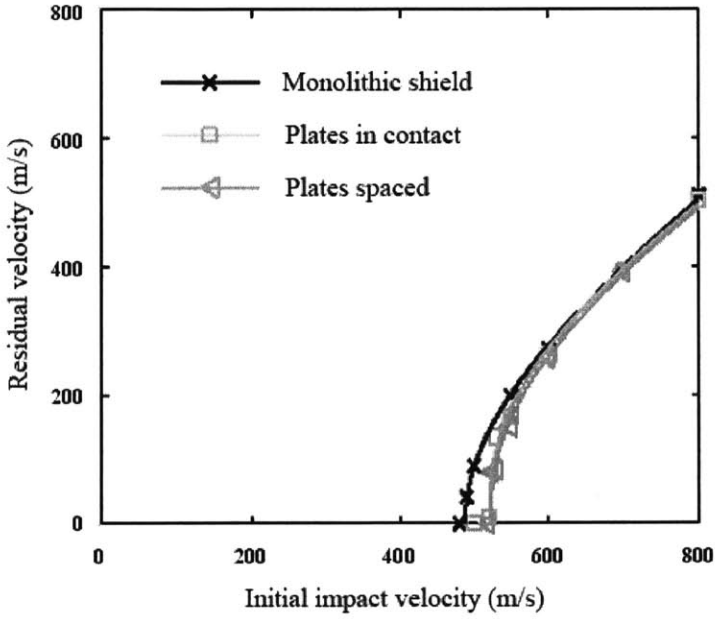

Fig. 3.13: The initial impact velocity vs. the residual velocity for the three types of shields impacted by the light flat-nose projectile.

Monolithic plate	Double-layered shield with the plates in contact	Double-layered shield with the plates spaced
487.4 (1.00)	520.0 (1.07)	523.0 (1.07)

Table 3.3: The ballistic limits of the shields impacted by the light, flat-nose projectile (unit: m/s)

According to our results, the calculated ballistic limit of the double-layered shield with the plates spaced is slightly higher than that with the plates in contact. However, the variation in the spacing between the two plates is not able to considerably improve the ballistic resistance, because the failure mode is kept almost the same.

3.4 Light conical-nose projectile

The light conical-nose projectile of the mass 10.0g is considered as a simplification of a standard 7.62mm hard-core bullet. It is realized that a real bullet projectile is usually of the ogival-nose rather than the conical nose. However, Dey et al. [24] found from a series of tests that a conical-nose projectile has a very similar perforation capability to the ogival-nose one.

Figures 3.14-3.16 show the perforation processes of the three types of shields impacted by the light conical-nose projectile at V_0 = 600.0m/s. It can be observed that all the three shields fail by ductile hole enlargement. The shields are subjected to little structural deformation and plastic deformation concentrates in the impacted zone beneath the projectile. According to our results, the failure mode keeps almost the same at a range of impact velocities. At the same time, this failure mechanism is almost identical to that of the previous case with the heavy projectile. Therefore, it can be concluded that, for the conical-nose projectile, the double-layered shield would not introduce a new failure mode.

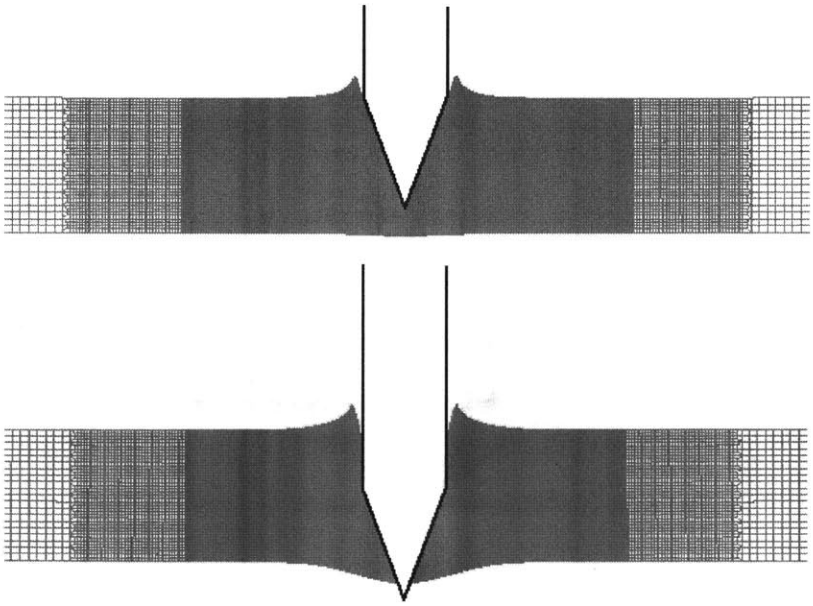

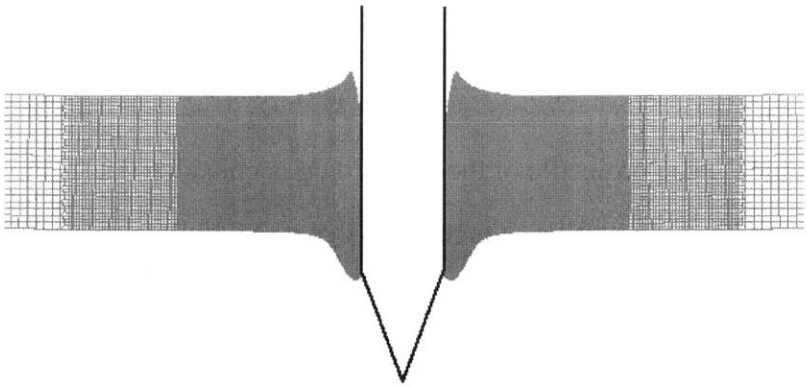

Fig. 3.14: The perforation process of the monolithic plate impacted by the light conical-nose projectile at $V_0 = 600.0$m/s.

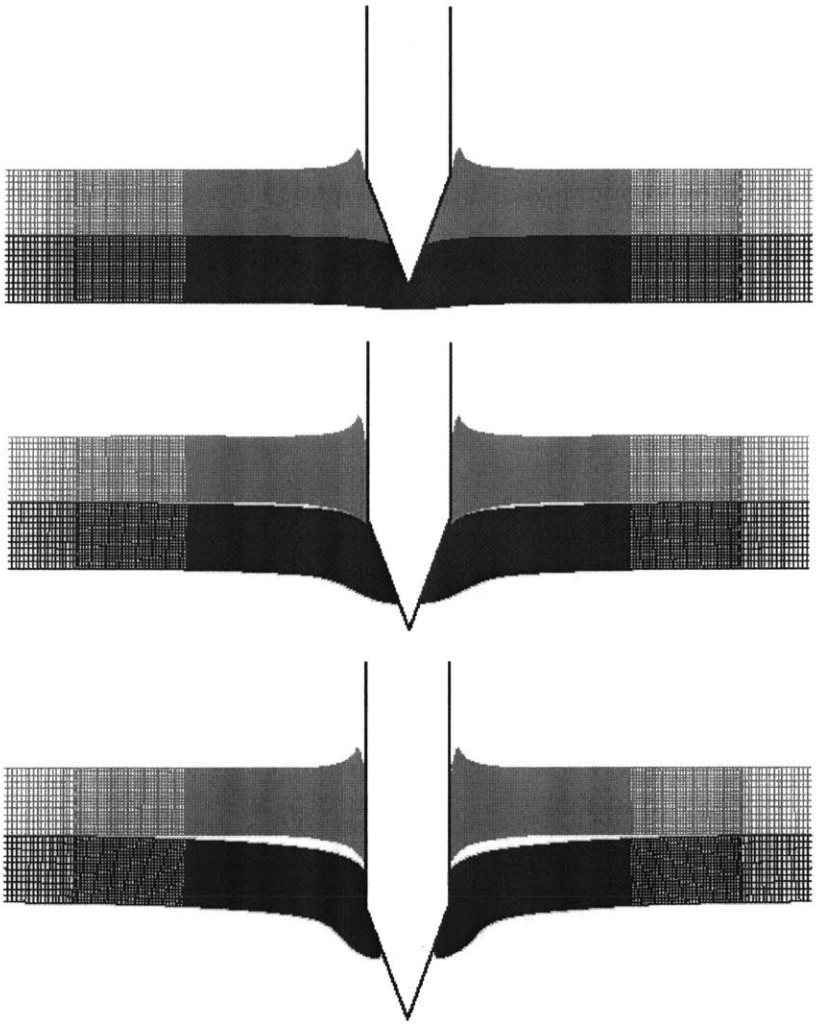

Fig. 3.15: The perforation process of the double-layered shield with the plates initially adjacent impacted by the light conical-nose projectile at $V_0 = 600.0$m/s.

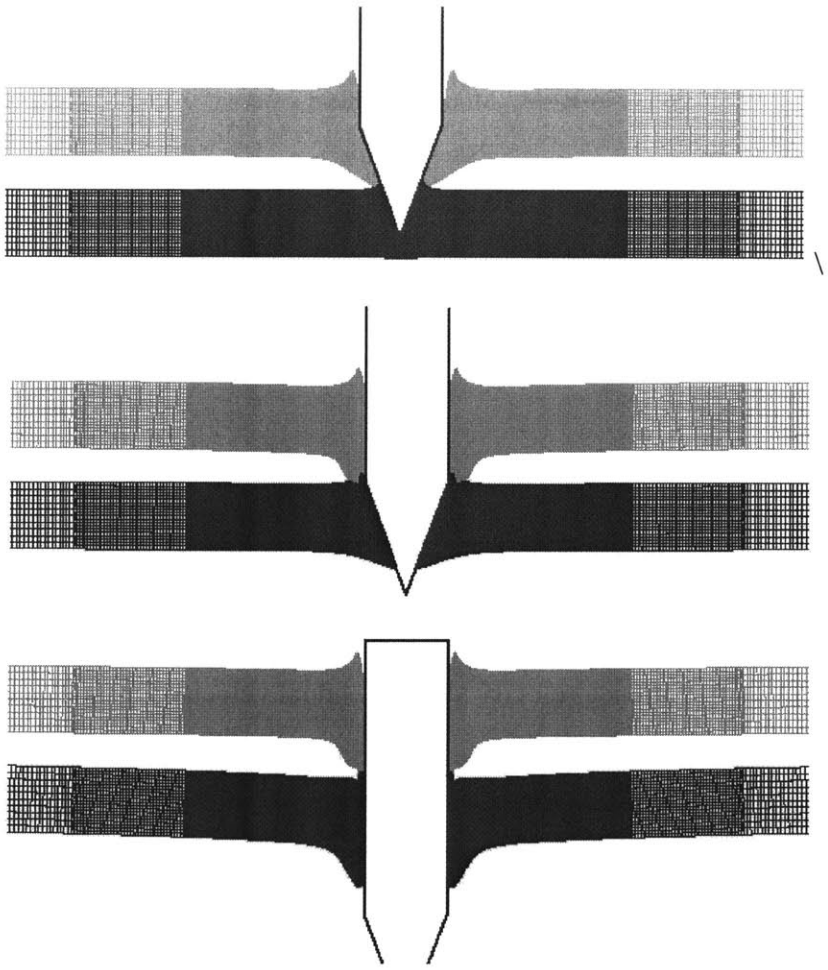

Fig. 3.16: The perforation process of the double-layered shield with the plates spaced impacted by the light conical-nose projectile at V_0 = 600.0m/s.

Figure 3.17 shows the plots of the initial impact velocity vs. the residual velocity for the three types of shields. The corresponding ballistic limits are listed in Table 3.4. It can be observed that the double-layered shield is slightly weaker in ballistic resistance. However, the difference between the effect of the monolithic plate and the double-layered shields is so small that it can be neglected. At the same time, the numerical results indicate that the increase in the spacing between the two plates does not improve the ballistic resistance of the shield.

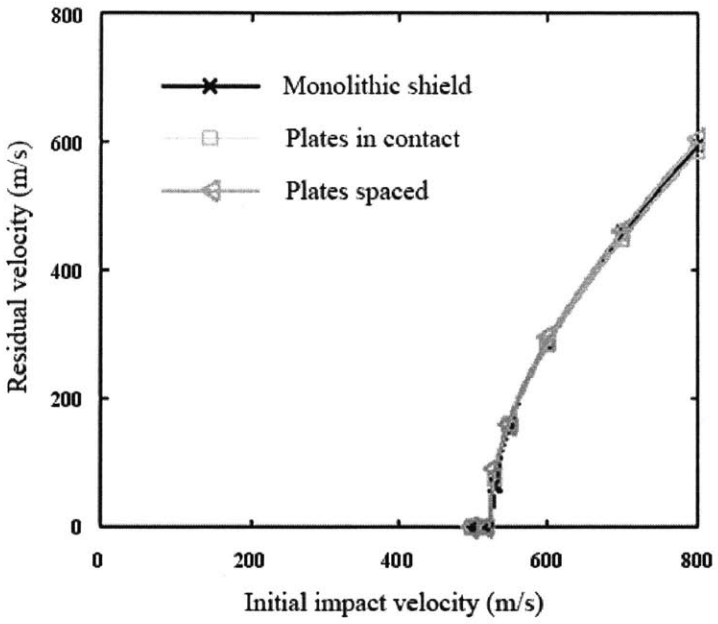

Fig. 3.17: The initial impact velocity vs. the residual velocity for the three types of shields impacted by the light conical-nose projectile.

Monolithic plate	Double-layered shield with the plates in contact	Double-layered shield with the plates spaced
525.9 (1.000)	524.5 (0.997)	522.5 (0.994)

Table 3.4: The ballistic limits of the shields impacted by the light, conical-nose projectile (unit: m/s)

A few armor piercing experiments has been performed on the double/multiple-layered shields impacted by the standard 7.62mm calibre bullet balls, e.g. Almohandes et al. [4], Gupta and Madhu [25]. According to their results, there is slight degradation in the ballistic resistance of the double/multiple-layered shields, compared to the monolithic plate of the same total weight. Those experimental results qualitatively agree with the present numerical prediction.

3.5 Comparison with experimental results

Besides numerical study, Børvik et al. [12, 13] also performed many experimental tests on the ballistic resistance of a Weldox 460 E steel shield under the impact of a flat-nose, a round-nose, and a conical-nose projectile. By conducting the tensile tests on round bars under various strain rates and temperature change [19], the strength and fracture properties of Weldox steels were calibrated. In this section, the experimental results published in the literature are used to verify the numerical procedures. The geometrical dimensions of the projectile-target shield systems for the monolithic plates were taken to be identical to the one designed by Børvik et al. [12]. Therefore, the present numerical predictions can be directly verified by comparing to the experimental results.

The plots of the initial impact velocity vs. the residual velocity for the case with the monolithic plate under impact by the heavy flat-nose and conical-nose projectiles are shown in Fig. 3.18 and 3.19. It was observed that the numerical results agree well with the test results. Hence, the correctness of the present finite element procedure is validated.

Recently, Dey et al. [6] performed 36 perforation tests on double-layered shields. In his experiments, the target shields made of Weldox 700 E steel were impacted by a flat-nose and a ogival-nose projectile at sub-ordnance velocities. According to his results, the ballistic resistance could be increased by about 30% by using the double-layered configuration instead of the monolithic plates in the case with the flat-nose projectile, see Fig. 3.20. This is in general in accordance with the present numerical results. However, the experimental data cannot be directly compared with the present numerical results, because the plasticity and fracture properties of Weldox 700 E steel is significantly different from those of Weldox 460 E steel, which is used in the present numerical simulations.

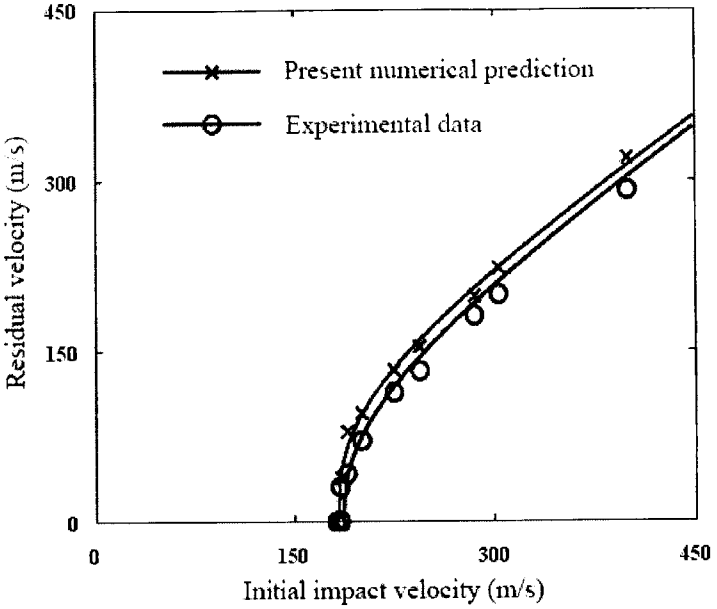

Fig. 3.18: Comparison of the residual velocities between the numerical prediction and the experimental results for the monolithic plate impacted by the heavy flat-nose projectile.

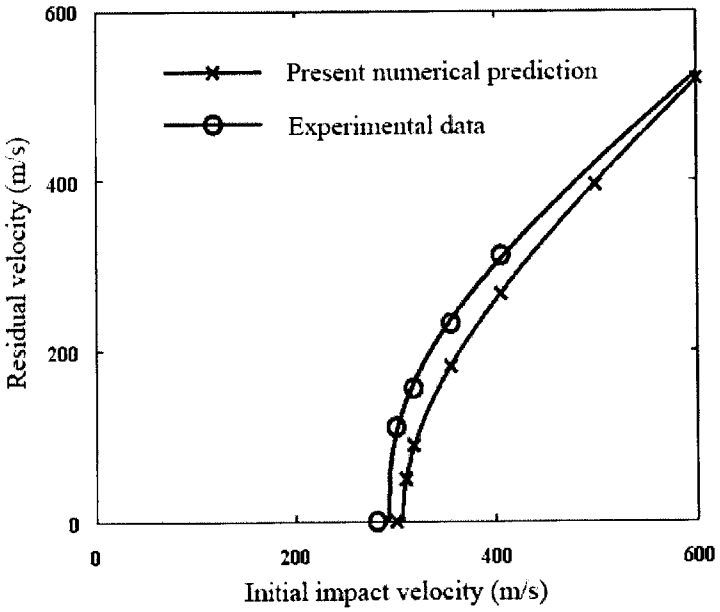

Fig. 3.19: Comparison of the residual velocities between the numerical prediction and the experimental results for the monolithic plate impacted by the heavy conical-nose projectile.

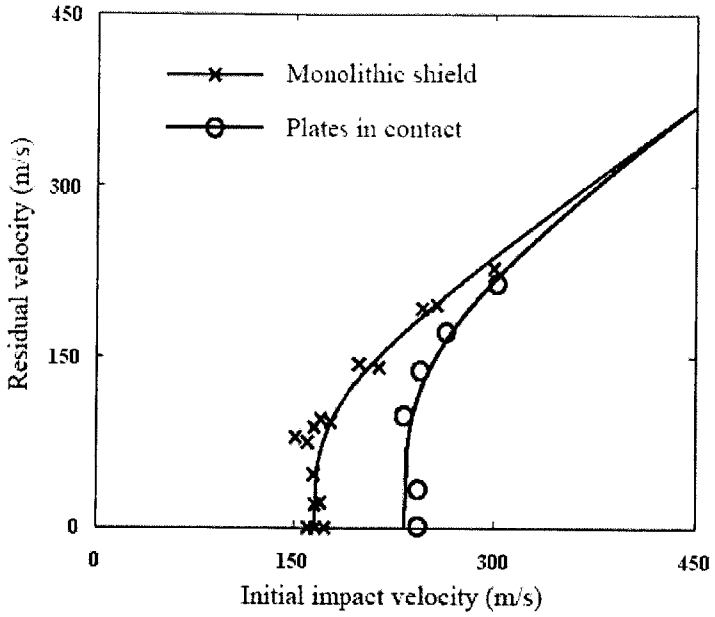

Fig. 3.20: Comparison of experimentally obtained residual velocities between the monolithic and the double-layered shield.

Chapter 4
Ballistic Resistance of the Double-layered Shields with Different Combinations of Materials

4.1 Heavy conical-nose projectile

In this section, a conical-nose projectile of the mass M_0 = 200g and the diameter d = 24mm is considered as the striker.

At first, the monolithic plate of two different materials, Weldox 460 E steel and Domex Protect 500 steel, is studied. Figures 4.1 and 4.2 show the perforation processes of the monolithic plates of high ductility and low ductility materials impacted by the heavy conical-nose projectile at V_0 = 400m/s.

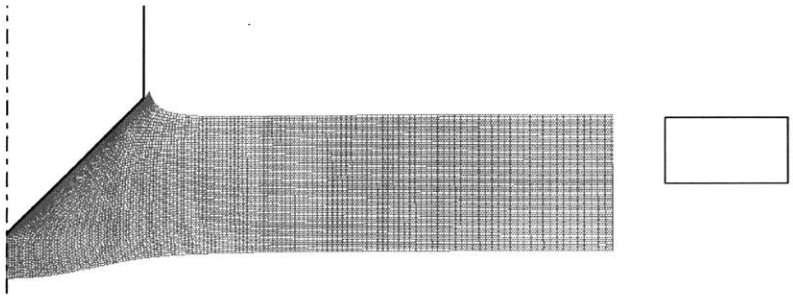

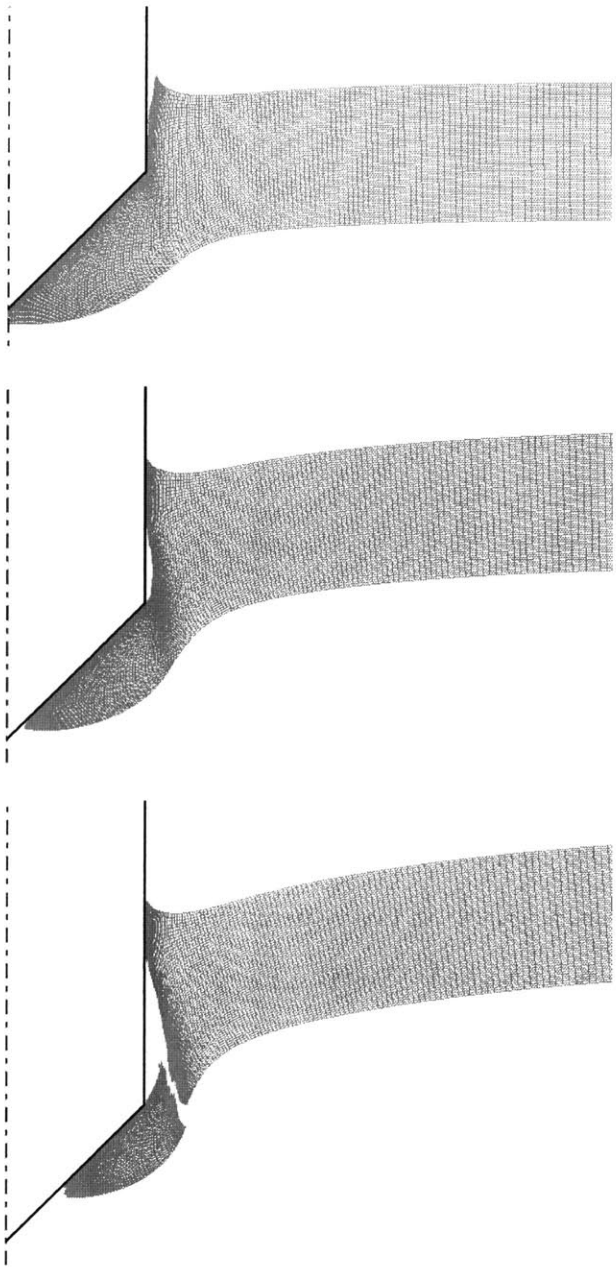

Fig. 4.1: The perforation process of the monolithic plate of high ductility material impacted by the heavy conical-nose projectile at $V_0 = 400$m/s

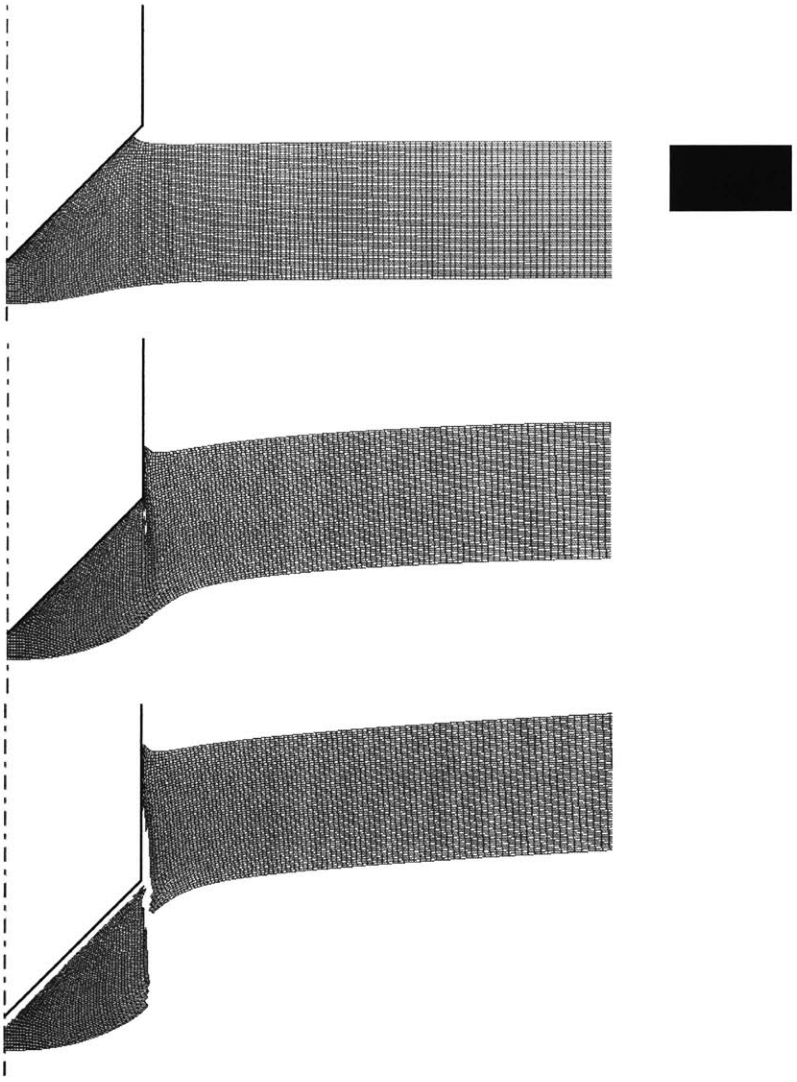

Fig. 4.2: The perforation process of the monolithic plate of low ductility material impacted by the heavy conical-nose projectile at $V_0 = 400$m/s

As shown in Fig. 4.2, shear plugging is the predominant failure mode for the monolithic plate of low ductility material. Since the monolithic plate of high ductility material undergoes deep necking before failure, its dominating failure mode is tensile tearing, see Fig. 4.1. Compared with high ductility material Weldox 460 E steel, the low fracture locus of Domex Protect 500 steel leads to early fracture and insignificant global deformation. It can be concluded that high ductility material has advantage over low ductility material in energy dissipation.

According to our simulation results, the residual velocity of projectile is 160m/s for the case with the high ductility monolithic plate, while 205m/s for the case with low ductility one. The simulation results agree with our qualitative analysis. The conclusion here is that the perforation resistance of the monolithic plate of low ductility material is worse than that of high ductility material at the impact velocity of 400m/s. Actually the contribution of low ductility material to plastic energy dissipation is weakened by its early fracture.

Now, a question comes up: How to maximize the energy dissipation potential of low ductility material. Professor Wierzbicki suggested that a double-layered shield with the upper and lower layer of different materials can be considered as a possible optimum configuration of shield for ballistic resistance.

Figure 4.3 shows the perforation processes of the double-layered shield with the upper layer of low ductility material and lower layer of high ductility material impacted by the heavy conical-nose projectile at $V_0 = 400$m/s. It can be observed that the upper layer tends to fail by shear plugging with insignificant global bending and plastic deformation. This is similar to the preceding case with the monolithic plate of low ductility material. This configuration is not able to improve the perforation resistance. Actually, the residual velocity of projectile in this case is 240m/s, which is the highest among all cases.

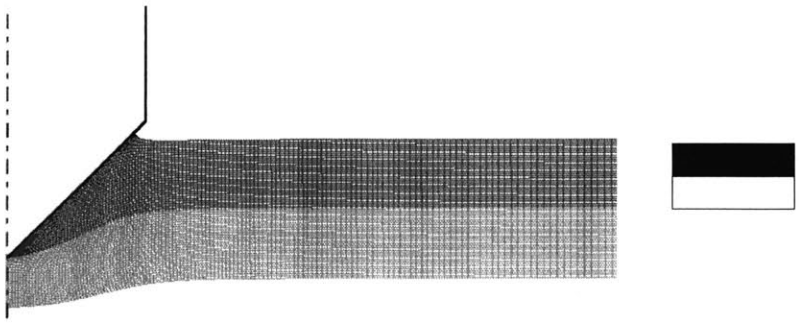

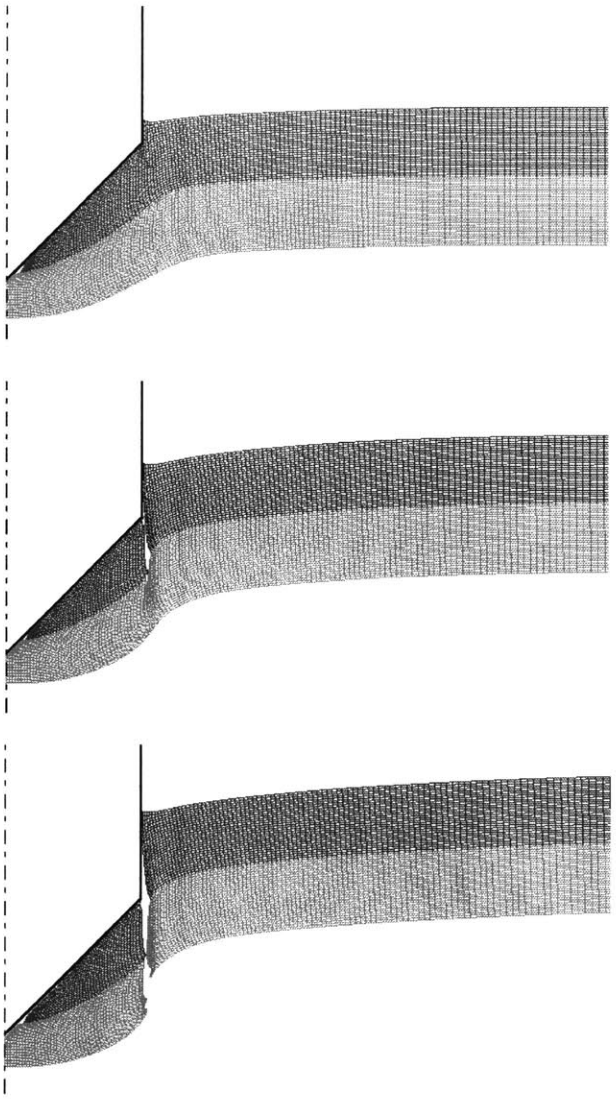

Fig. 4.3: The perforation process of the double-layered shield with the upper layer of low ductility material and lower layer of high ductility material impacted by the heavy conical-nose projectile at $V_0 = 400$m/s

Now, let us replace the position of two materials, we obtain another modified configuration. Figure 4.4 shows the perforation process of the double-layered shield with the upper layer of high ductility material and lower layer of low ductility material impacted by the heavy conical-nose projectile at $V_0 = 400$m/s.

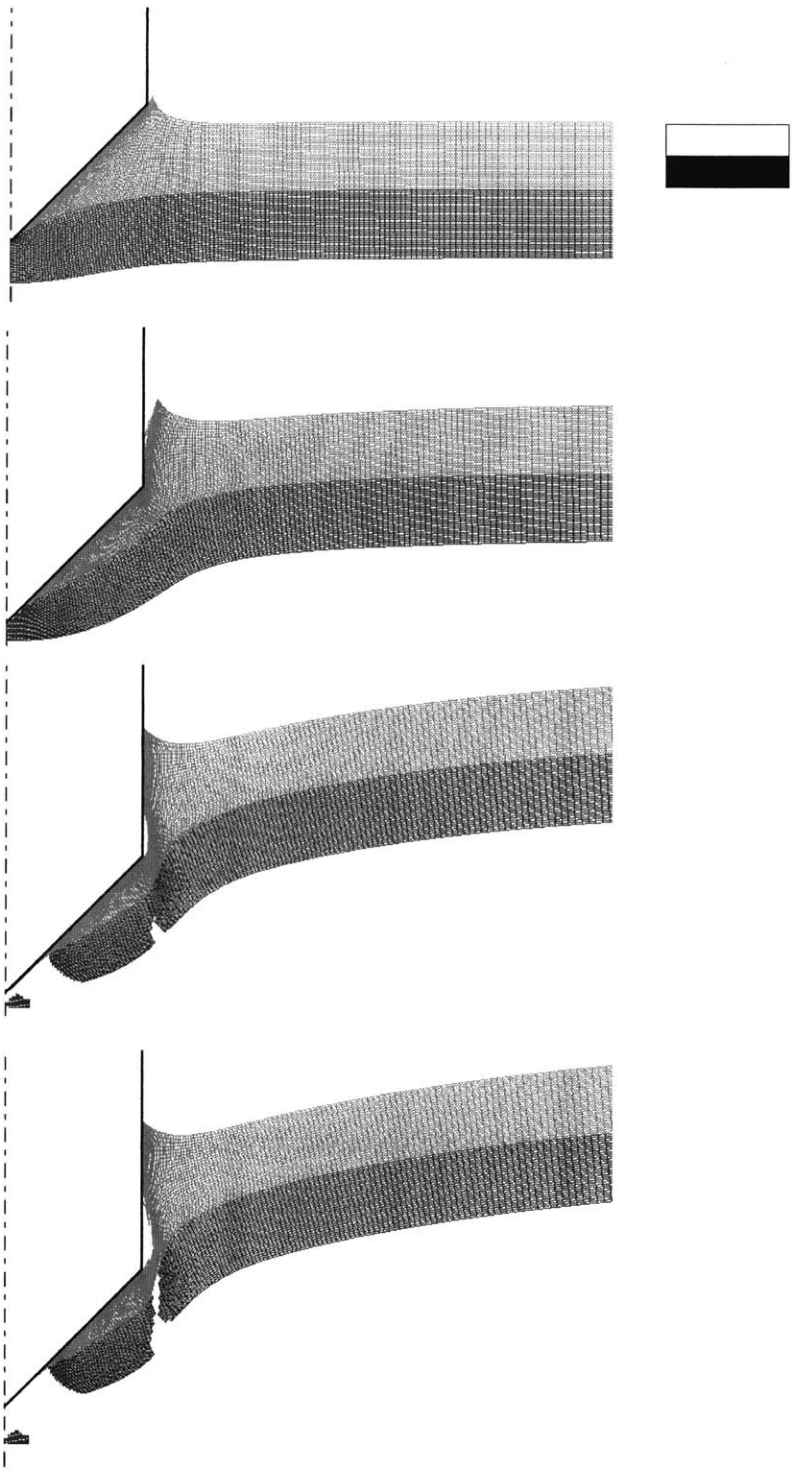

Fig. 4.4: The perforation process of the double-layered shield with the upper layer of high ductility material and lower layer of low ductility material impacted by the heavy conical-nose projectile at $V_0 = 400$m/s

It can be observed from Fig. 4.4 that the upper layer undergoes deep necking before failure. Therefore, the predominant failure mode for upper layer is tensile tearing, while the lower layer mainly fails by shear plugging. Since the deformation region is extended well beyond the impact zone, the global bending in this configuration is found to be larger than that in any other configurations. As we have mentioned, the transition of the failure mode from shear plugging to tensile tearing is accompanied with a considerable increase in plastic energy dissipation. It can be concluded that the best configuration for perforation resistance against the heavy conical-nose projectile at V_0 = 800m/s is the double-layered shield with the upper layer of high ductility material and lower layer of low ductility material. Figure 4.5 shows the time history of the transient velocity of the heavy conical-nose projectile impacted at four types of shields at V_0 = 400m/s. The simulation results are in general in accordance with our qualitative analysis.

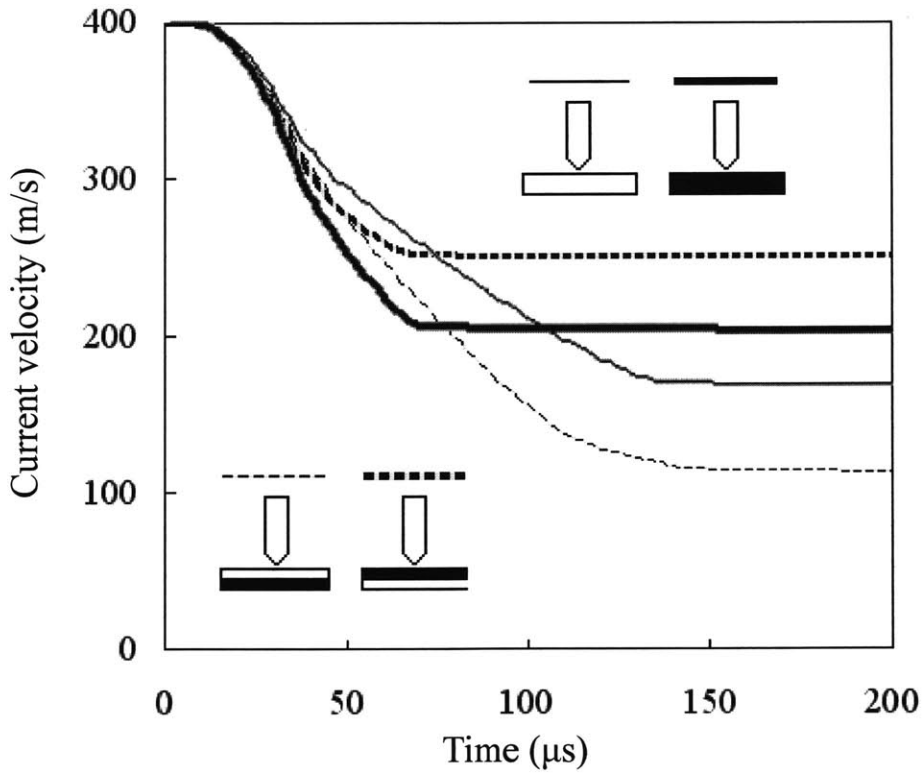

Fig. 4.5: Time history of the transient velocity of the heavy conical-nose projectile at V_0 = 400m/s

How the above picture will change with a higher impact velocity, e.g. V_0 = 800m/s? Figures 4.6-4.9 show the perforation processes of the monolithic and double-layered shields of different material combinations impacted by the heavy conical-nose projectile at V_0 = 800m/s. It can be observed that, high velocity increases the local plastic deformation in the impact zone in all configurations. Therefore, the advantage of high ductility material in plastic energy dissipation is weakened at high impact velocity. The failure mode is tensile tearing for the monolithic plate and double-layered shield with upper layer of high ductility material and lower layer of low ductility material, while the double-layered shield with upper layer of low ductility material and lower layer of high ductility material mainly fails by shear plugging.

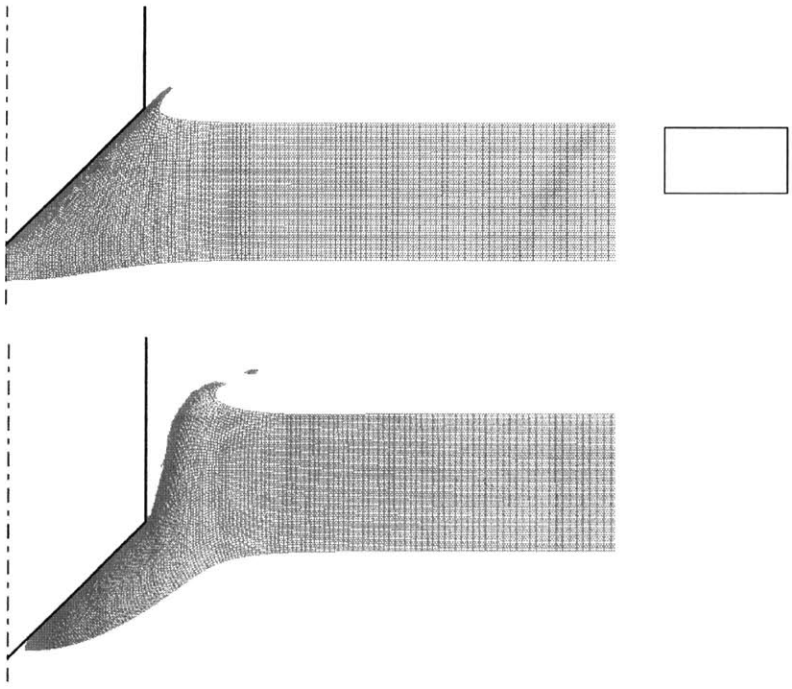

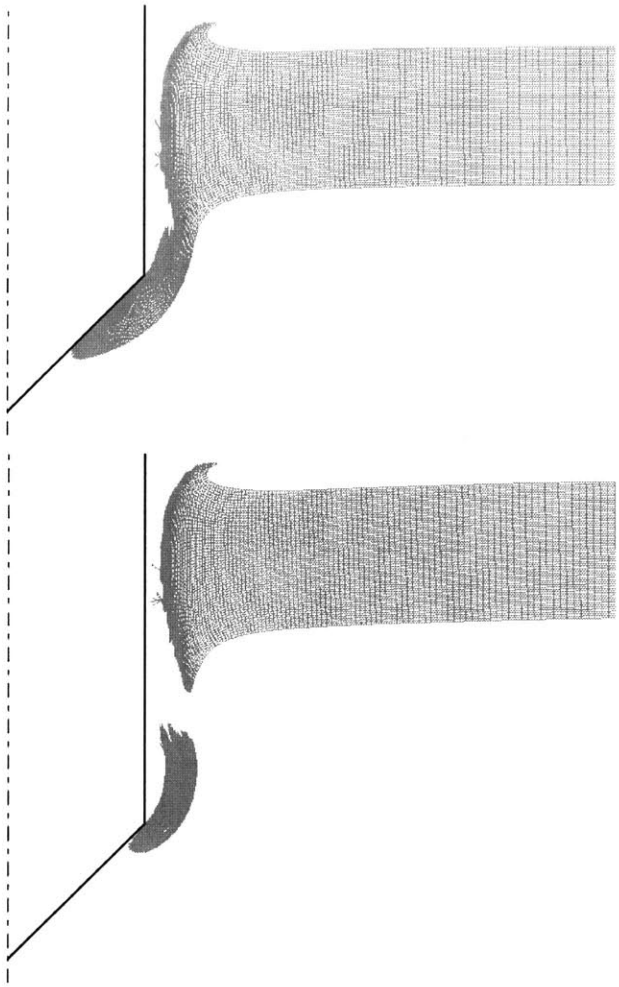

Fig. 4.6: The perforation process of the monolithic plate of high ductility material impacted by the heavy conical-nose projectile at V_0 = 800m/s

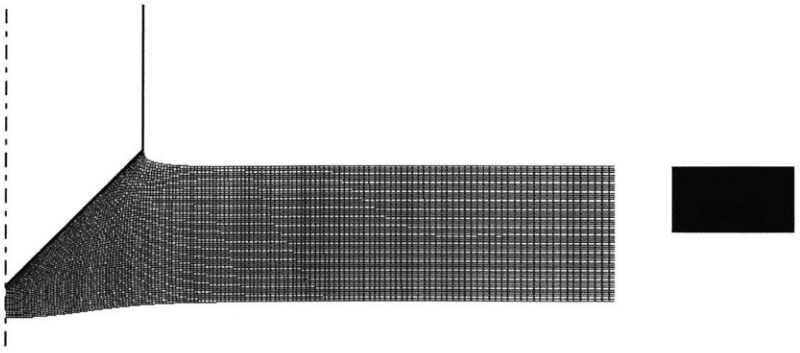

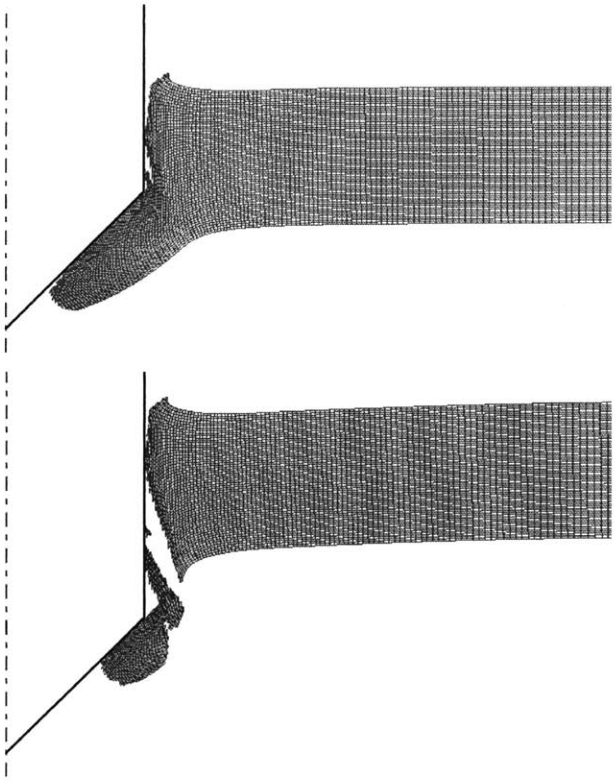

Fig. 4.7: The perforation process of the monolithic plate of low ductility material impacted by the heavy conical-nose projectile at $V_0 = 800$m/s

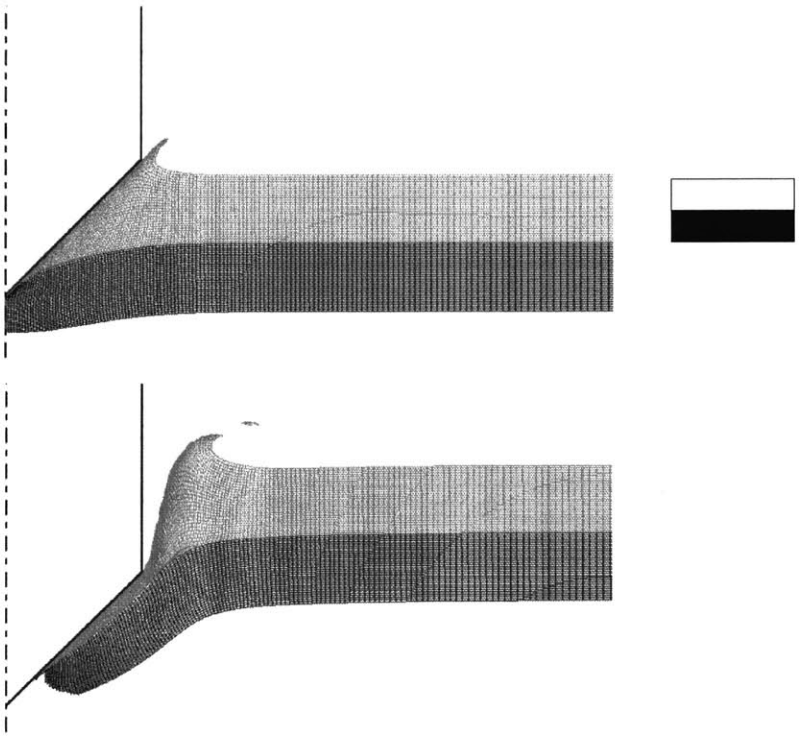

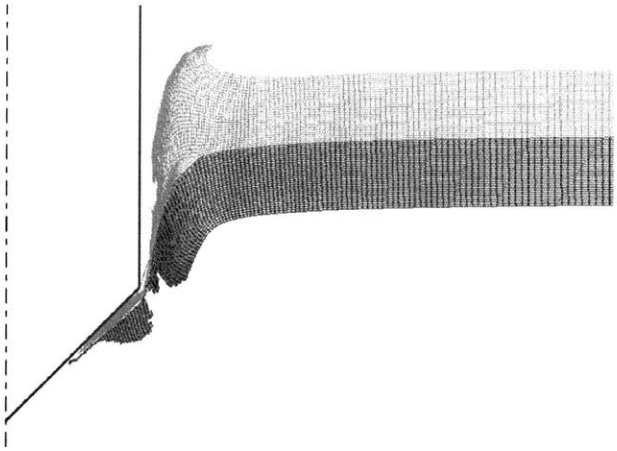

Fig. 4.8: The perforation process of the double-layered shield with the upper layer of high ductility material and lower layer of low ductility material impacted by the heavy conical-nose projectile at $V_0 = 800$m/s

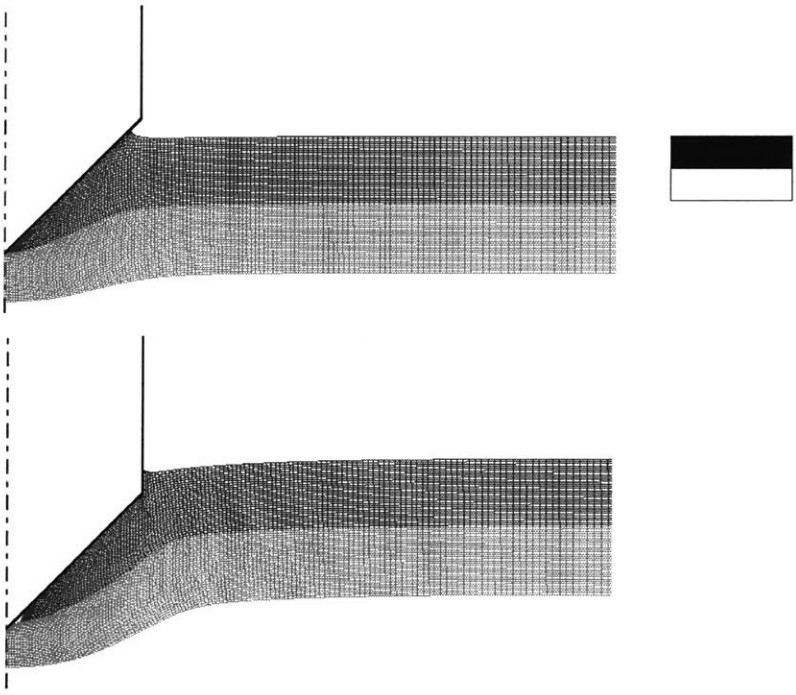

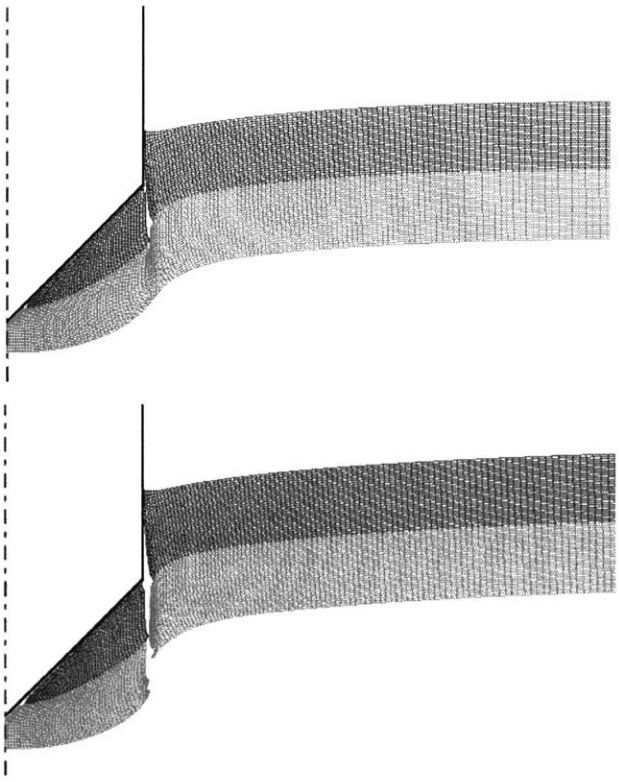

Fig. 4.9: The perforation process of the double-layered shield with the upper layer of low ductility material and lower layer of high ductility material impacted by the heavy conical-nose projectile at V_0 = 800m/s

At V_0 = 800m/s, the perforation resistance depends strongly on the ductility. It can be seen from the time history of the transient velocity of the heavy conical-nose projectile impacted at four types of shields, see Fig. 4.10. By the way, the position of two materials in the double-layered shields does not bring in any differences in this case.

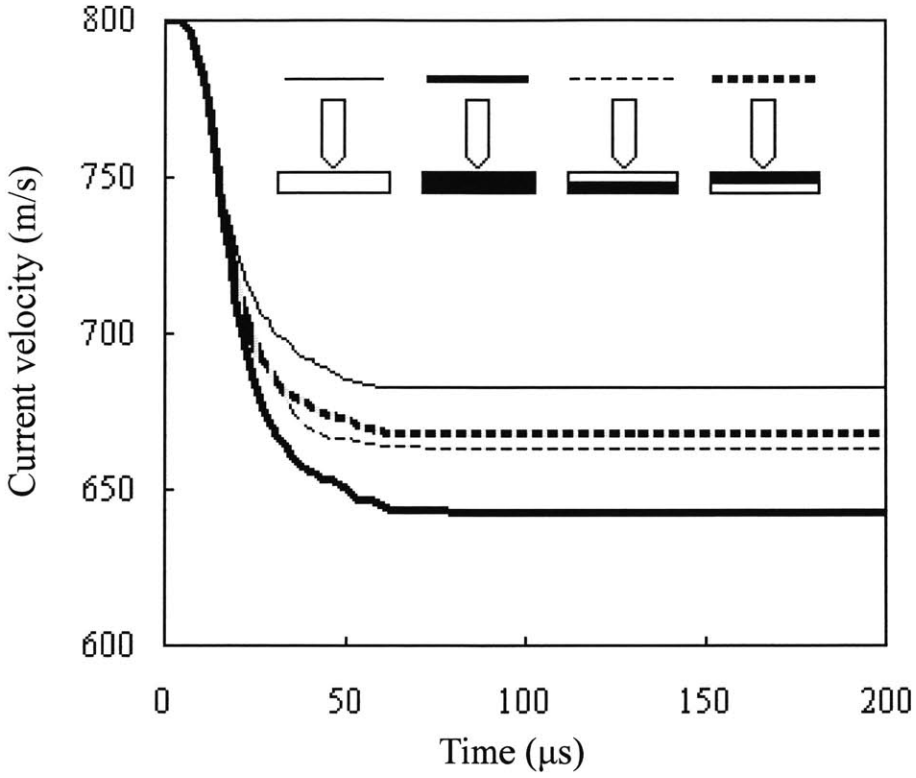

Fig. 4.10: Time history of the transient velocity of the heavy conical-nose projectile at V_0 = 800m/s

4.2 Heavy flat-nose projectile

The projectile considered in this section is a flat-nose projectile of the mass M_0 = 200g and the diameter d = 24mm.

Figures 4.11-4.14 show the perforation processes of the monolithic and double-layered shields of different material combinations impacted by the heavy flat-nose projectile at V_0 = 400m/s.

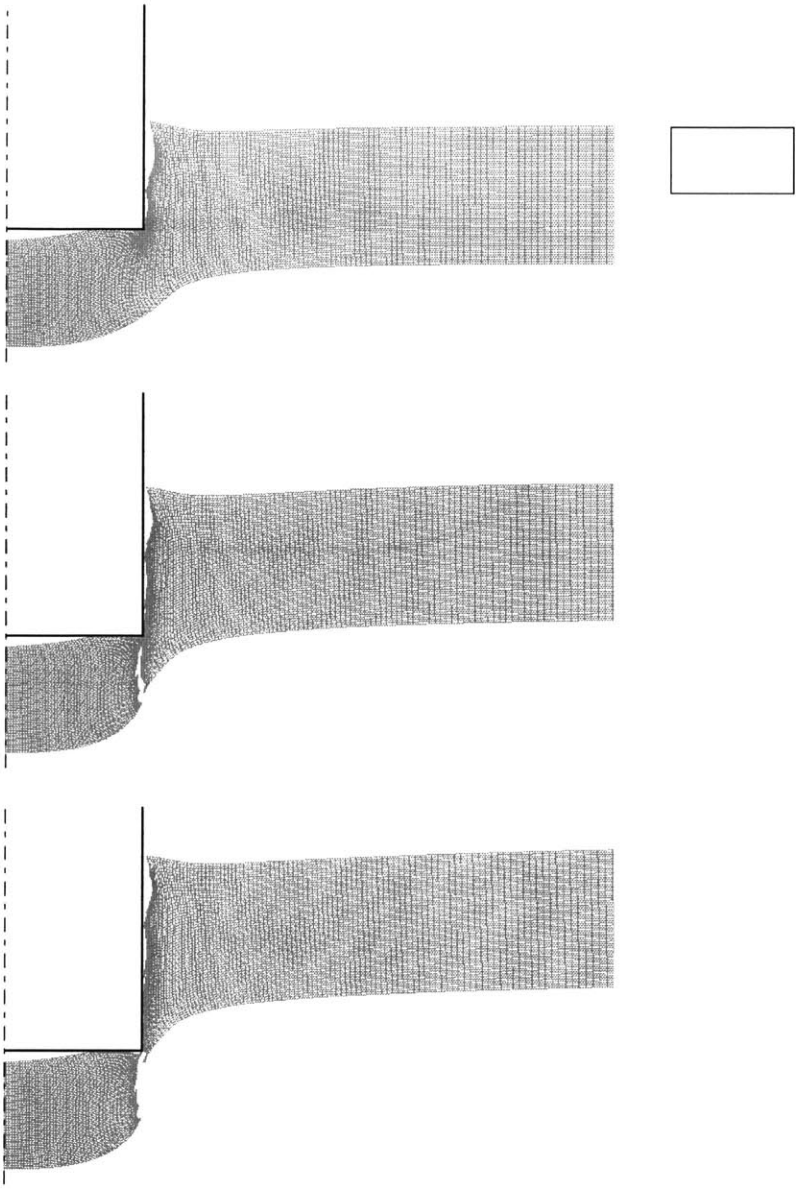

Fig. 4.11: The perforation process of the monolithic plate of high ductility material impacted by the heavy flat-nose projectile at V_0 = 400m/s

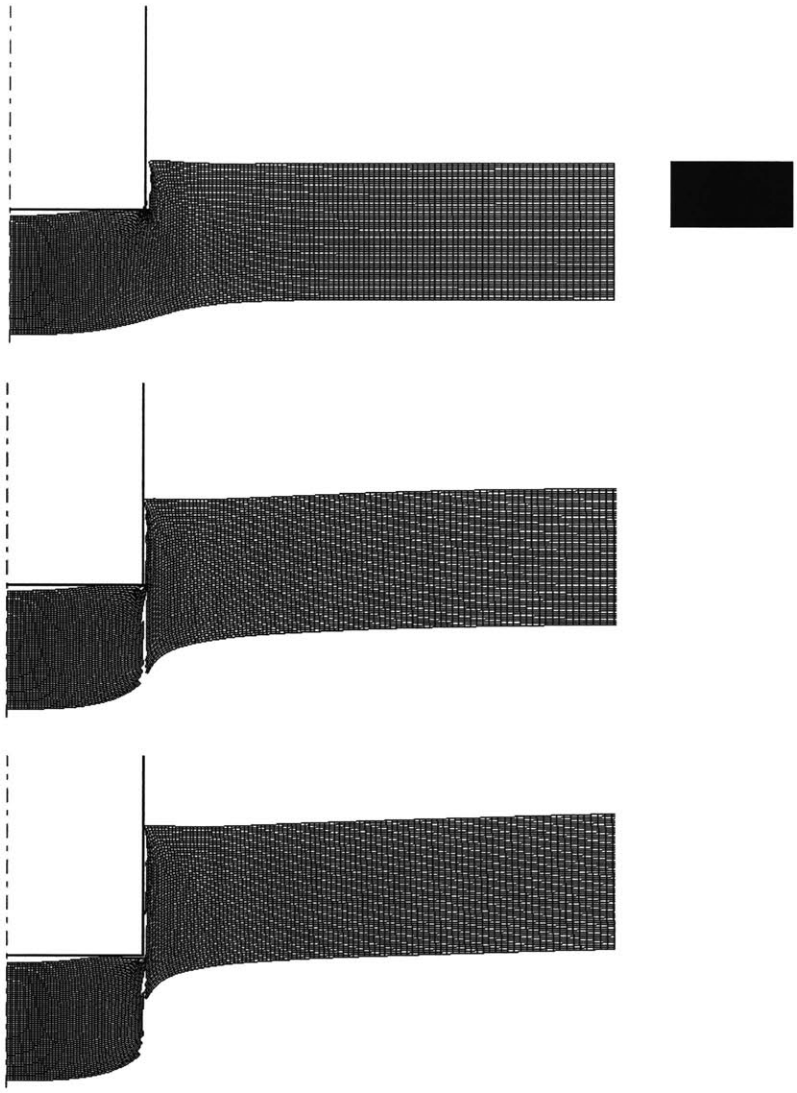

Fig. 4.12: The perforation process of the monolithic plate of low ductility material impacted by the heavy flat-nose projectile at $V_0 = 400$m/s

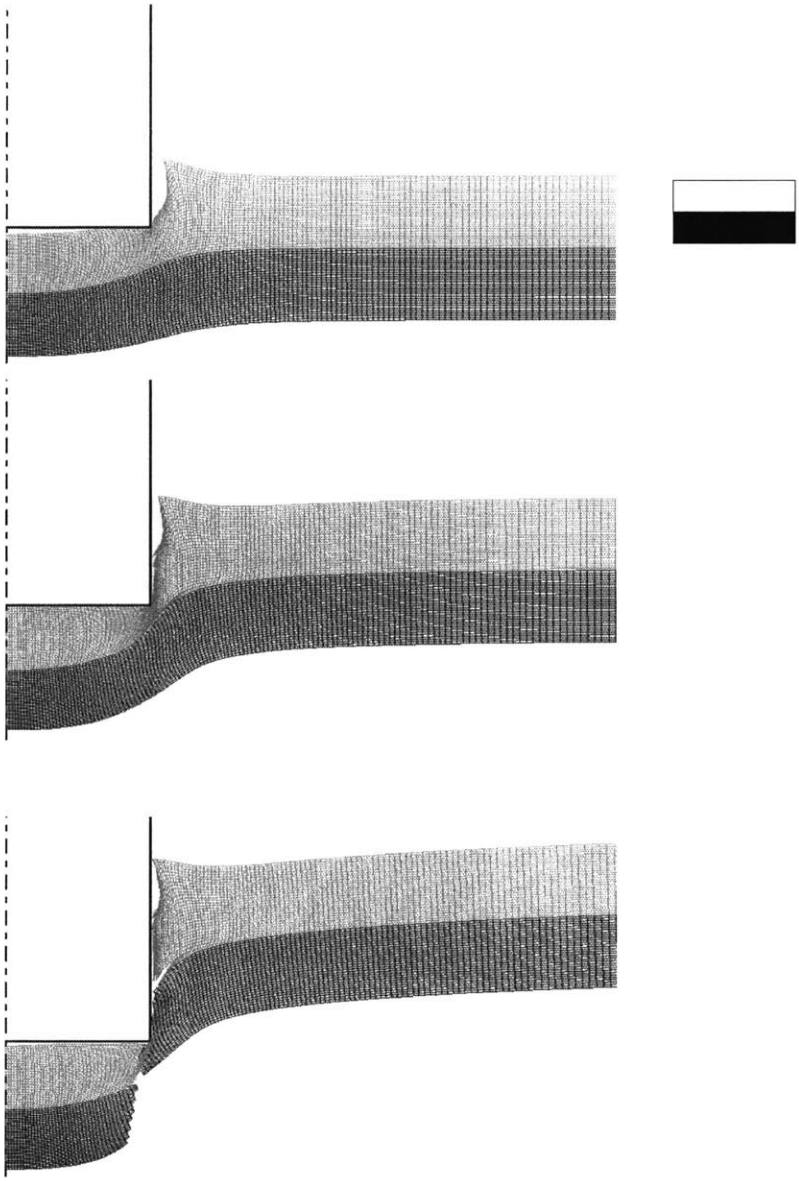

Fig. 4.13: The perforation process of the double-layered shield with the upper layer of high ductility material and lower layer of low ductility material impacted by the heavy flat-nose projectile at $V_0 = 400$m/s

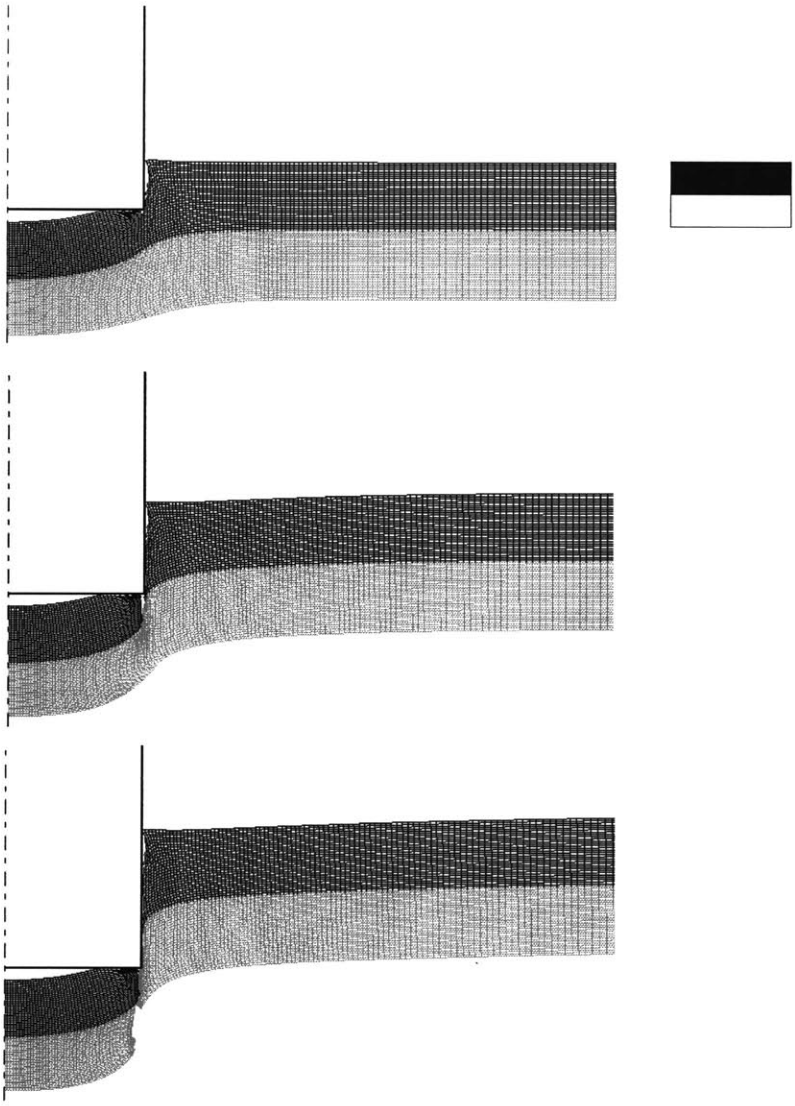

Fig. 4.14: The perforation process of the double-layered shield with the upper layer of low ductility material and lower layer of high ductility material impacted by the heavy flat-nose projectile at $V_0 = 400$m/s

It can be observe that shear plugging is the predominant failure mode for all the four configurations. As we have mentioned in the preceding section, crack formation and propagation is often induced by the sharp corner of flat-nose projectile. Also, the shields undergoes insignificant global deformation, the plastic deformation is localized in the impact zone. However, the double-layered shield with the upper layer of high ductility

material and lower layer of low ductility material is again the best in perforation resistance among all configurations. This can be seen from the time history of the transient velocity of the heavy flat-nose projectile impacted at four types of shields at V_0 = 400m/s, see Fig 4.15.

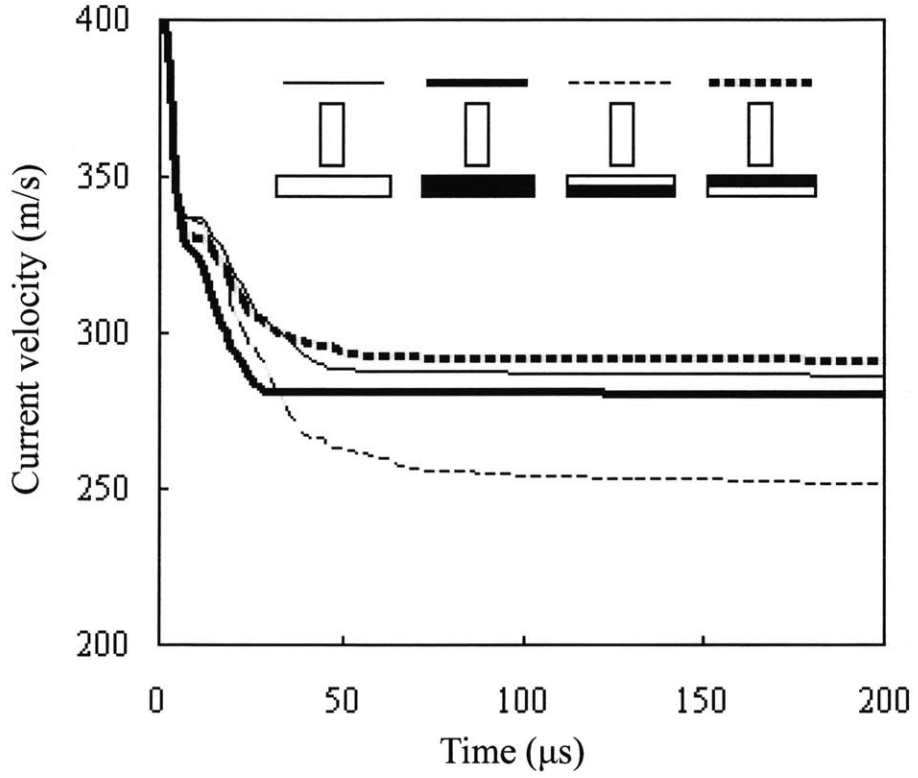

Fig. 4.15: Time history of the transient velocity of the heavy flat-nose projectile at V_0 = 400m/s

At the impact velocity of 800m/s, the phenomenon becomes interesting. As shown in Fig. 4.16-4.19, the materials in the impacted zone are push aside and a cavity, whose diameter is larger than that of the projectile, is generated. This is similar to the case in section 3.3, the double-layered separable shield impacted by the light flat-nose projectile at high impact velocity. As a projectile approaches the rear surface of the shields, the failure mode changes to tensile tearing and shear plugging.

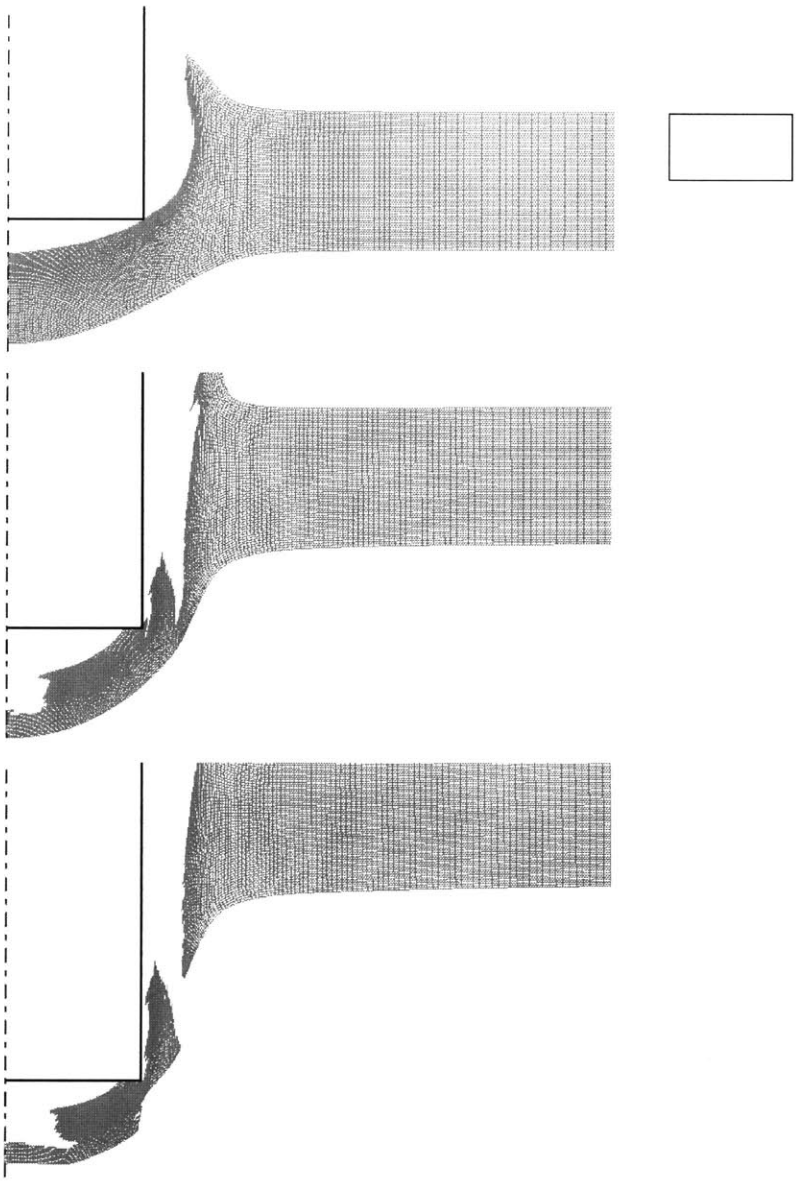

Fig. 4.16: The perforation process of the monolithic plate of high ductility material impacted by the heavy flat-nose projectile at V_0 = 800m/s

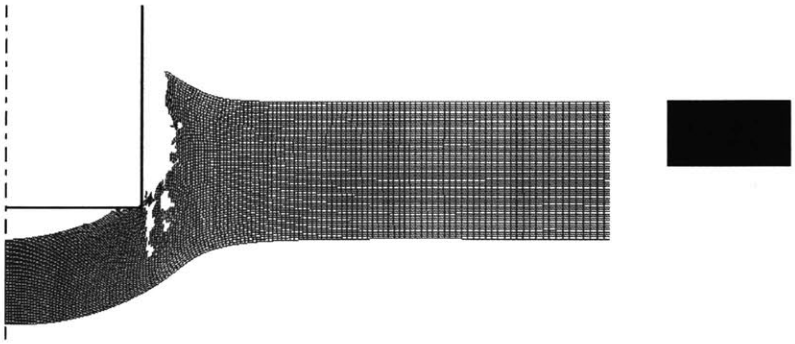

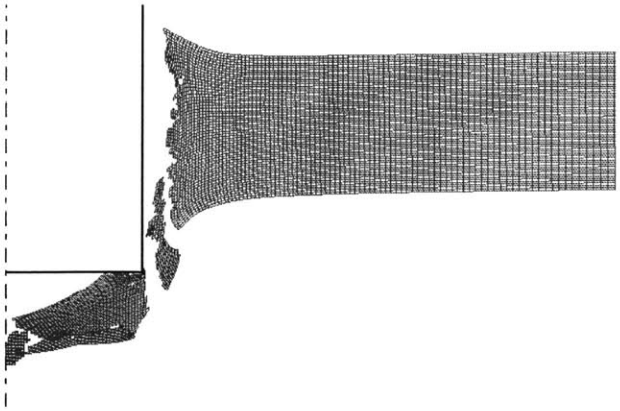

Fig. 4.17: The perforation process of the monolithic plate of low ductility material impacted by the heavy flat-nose projectile at V_0 = 800m/s

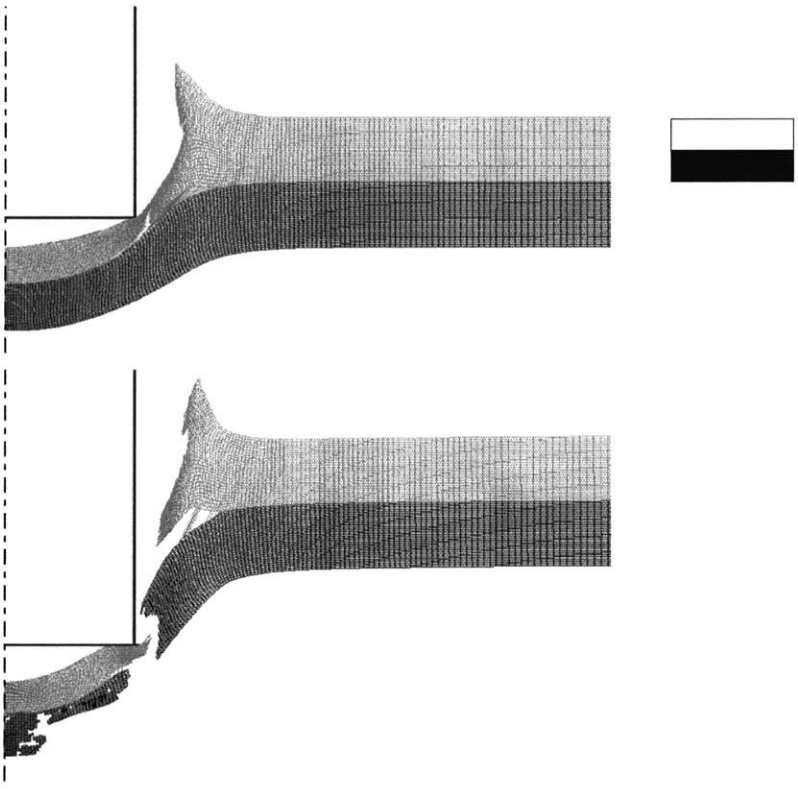

Fig. 4.18: The perforation process of the double-layered shield with the upper layer of high ductility material and lower layer of low ductility material impacted by the heavy flat-nose projectile at V_0 = 800m/s

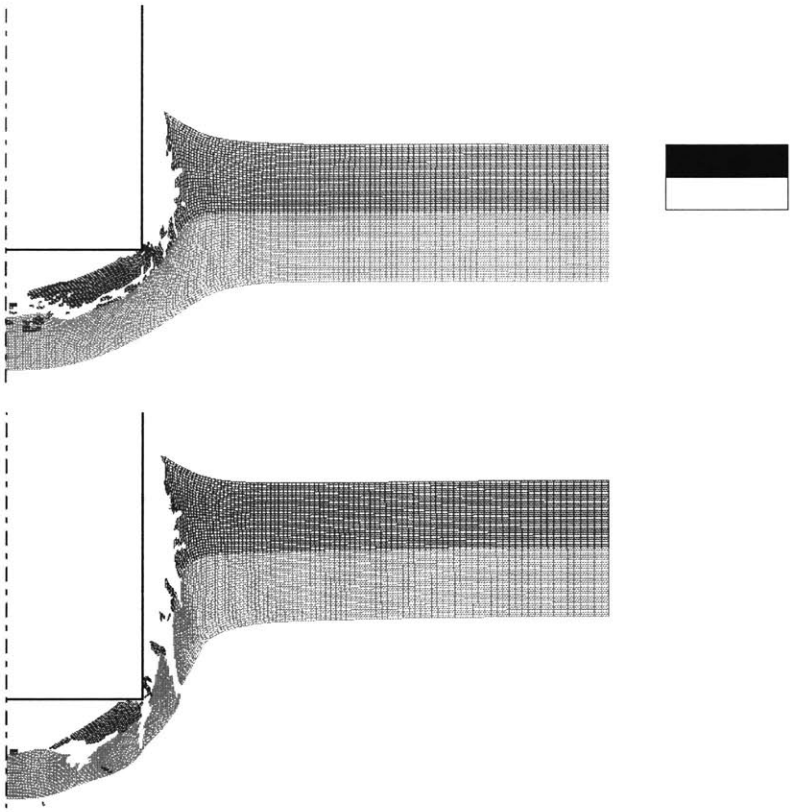

Fig. 4.19: The perforation process of the double-layered shield with the upper layer of low ductility material and lower layer of high ductility material impacted by the heavy flat-nose projectile at V_0 = 800m/s

Since all shields are torn to pieces, it is difficult to analyze the combined action of tension and shear. Figure 4.20 shows the time history of the transient velocity of the heavy flat-nose projectile impacted at four types of shields. It can be found that, the residual velocities of projectile are almost the same for four configurations at V_0 = 800m/s. At high impact velocity, all configurations are identical in perforation resistance under the impact by the heavy flat-nose projectile.

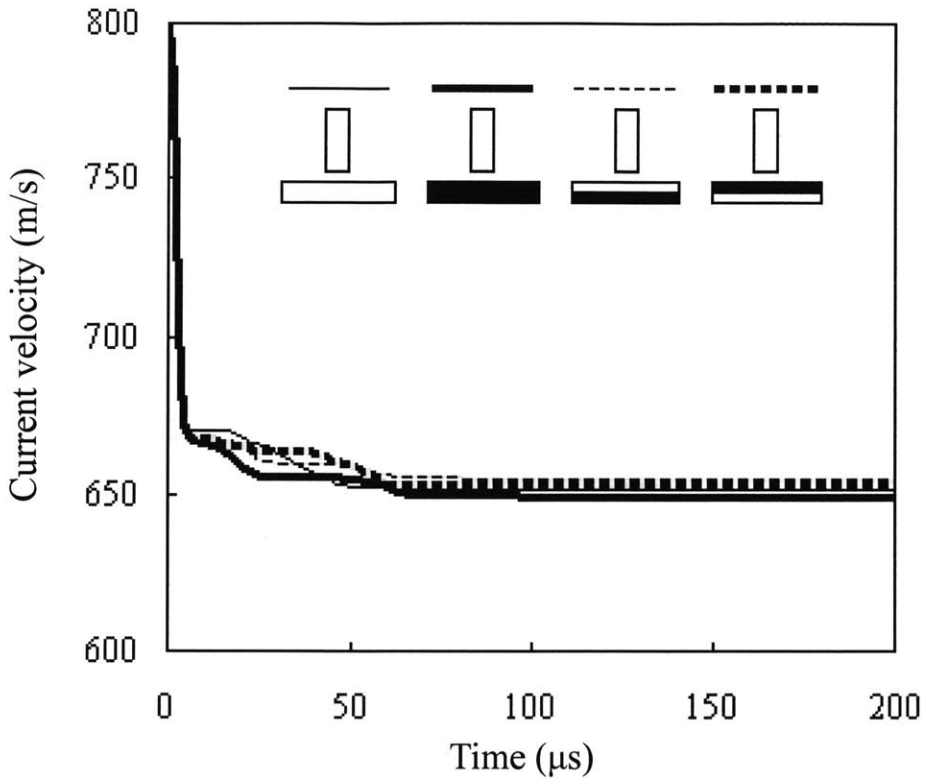

Fig. 4.20: Time history of the transient velocity of the heavy flat-nose projectile at V_0 = 800m/s

4.3 Light conical-nose projectile

In this section, a conical-nose projectile of the mass M_0 = 30g and the diameter d = 12mm is considered as the striker. Since the projectile is relatively light, it will be stopped by all type of shields at the impact velocity of 400m/s, see Fig. 4.21. Therefore, a high impact velocity, e.g. V_0 = 800m/s. is required to differentiate the perforation resistance of four types of shields.

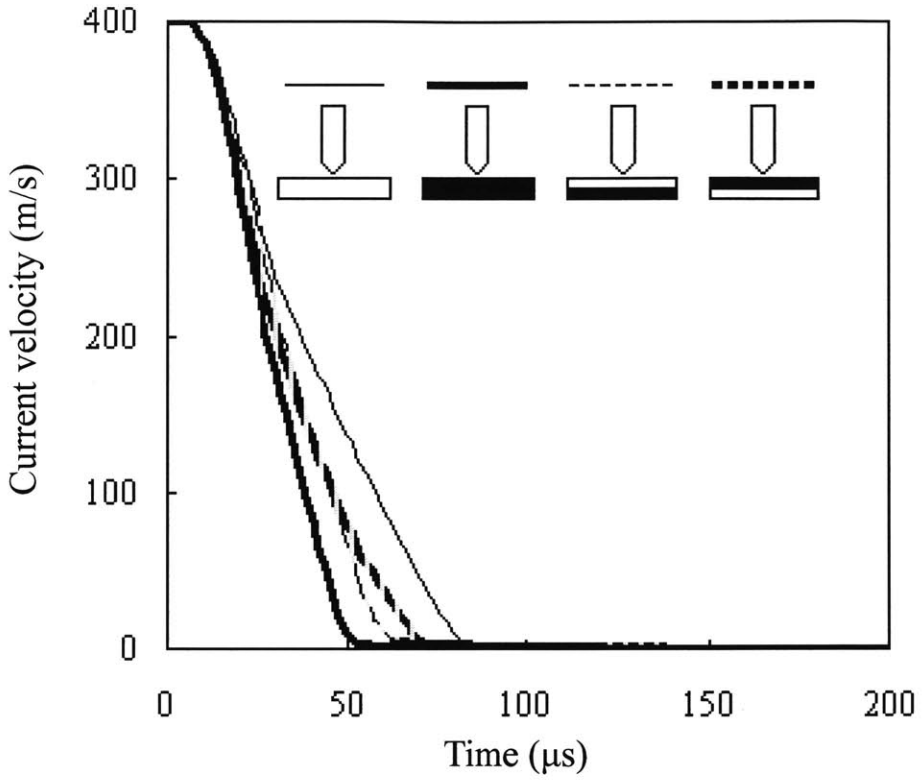

Fig. 4.21: Time history of the transient velocity of the light conical-nose projectile at $V_0 = 400$m/s

Figures 4.22-4.25 show the perforation processes of the monolithic and double-layered shields of different material combinations impacted by the light conical-nose projectile at V_0 = 800m/s. For the monolithic plates of high ductility material and the double-layered shield with upper layer of high ductility material and lower layer of low ductility material, the materials in the impacted zone are pushed aside until the projectile head approaches the rear surface. In the later steps, a small zone near the rear surface fails by tensile tearing.

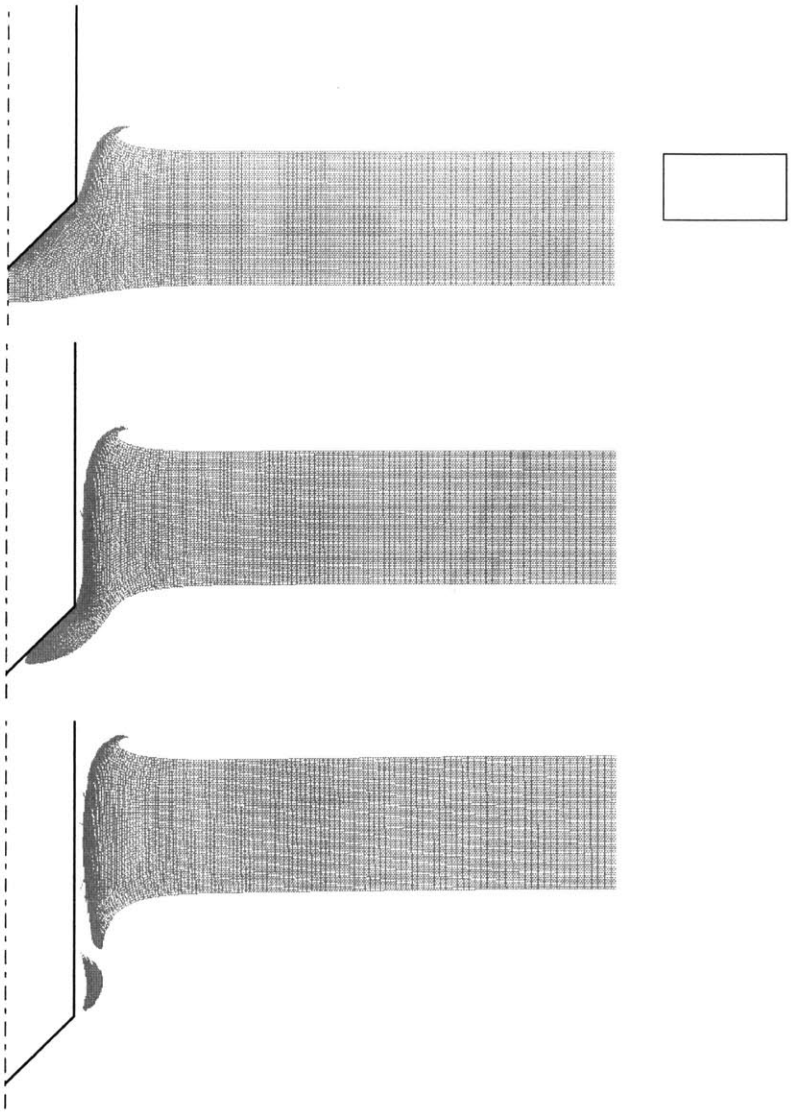

Fig. 4.22: The perforation process of the monolithic plate of high ductility material impacted by the light conical-nose projectile at $V_0 = 800$m/s

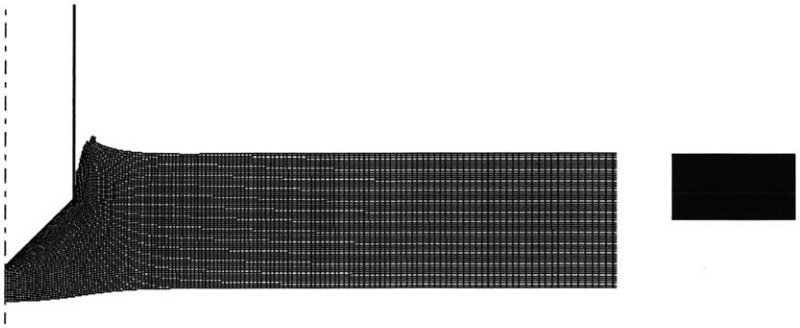

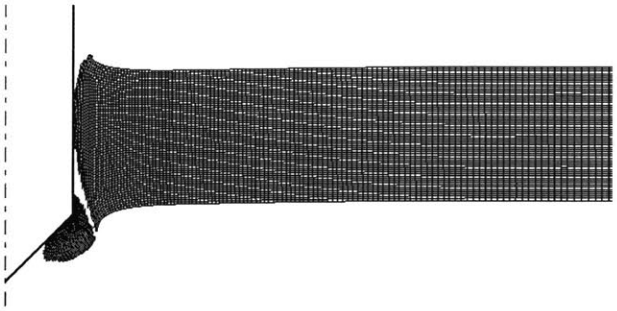

Fig. 4.23: The perforation process of the monolithic plate of low ductility material impacted by the light conical-nose projectile at V_0 = 800m/s

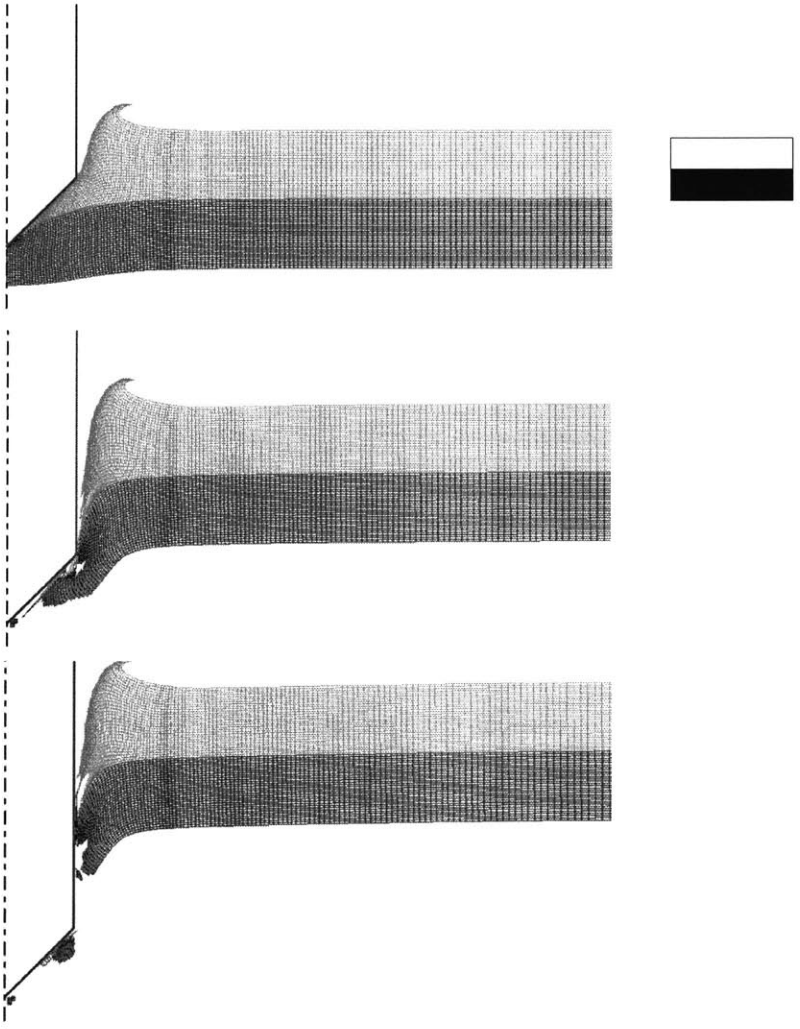

Fig. 4.24: The perforation process of the double-layered shield with the upper layer of high ductility material and lower layer of low ductility material impacted by the light conical-nose projectile at V_0 = 800m/s

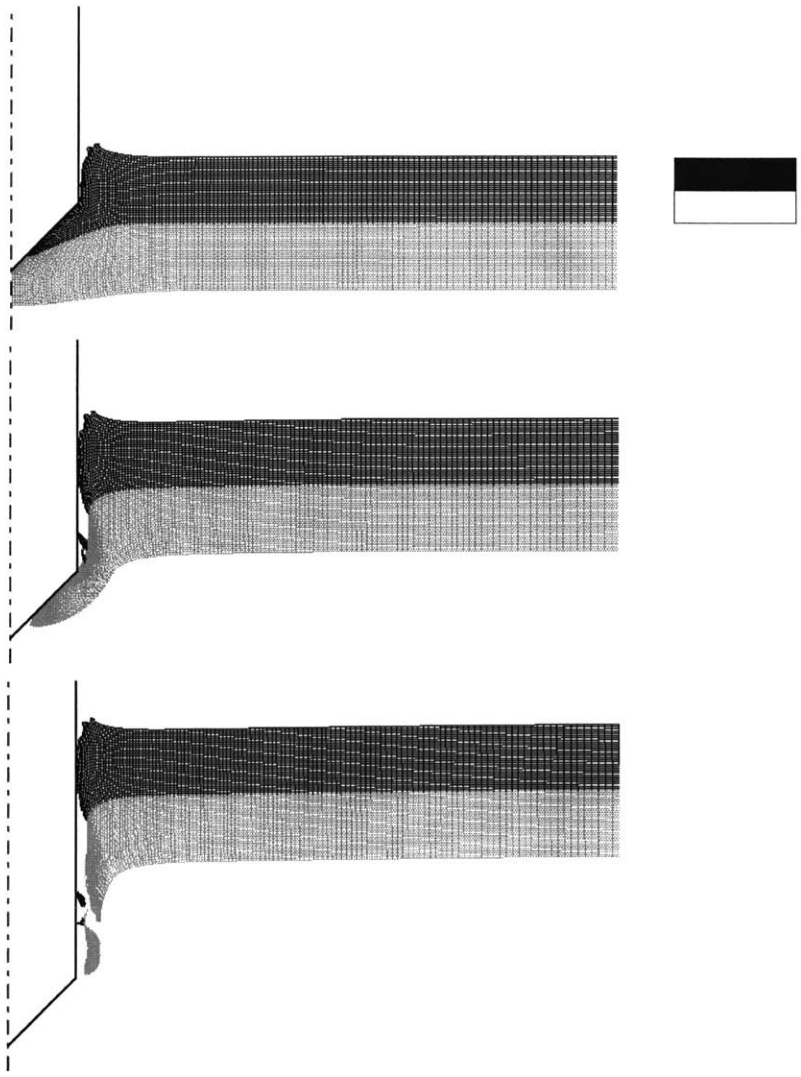

Fig. 4.25: The perforation process of the double-layered shield with the upper layer of low ductility material and lower layer of high ductility material impacted by the light conical-nose projectile at V_0 = 800m/s

The dominating failure mode is ductile hole enlargement for the monolithic plate of high ductility material and the double-layered shield with upper layer of high ductility material and lower layer of low ductility material. Differently, the monolithic plate of low ductility material fails by shearing plugging, while tensile tearing is found to be the dominating failure mode for the double-layered shield with the upper layer of low ductility material and the lower layer of high ductility material

Figure 4.26 shows the time history of the transient velocity of the light conical-nose projectile impacted at four types of shields at V_0 = 800m/s. Again, the double-layered shield with the upper layer of high ductility material and the lower layer of low ductility material is found to be the best configuration for perforation resistance under the impact of the light conical-nose projectile at V_0 = 800m/s. It can also be observed that, the two worst configurations for perforation resistance fails by ductile hole enlargement. Therefore, it can be concluded that ductile hole enlargement is the worst mode for plastic energy dissipation, while tensile tearing is the best mode.

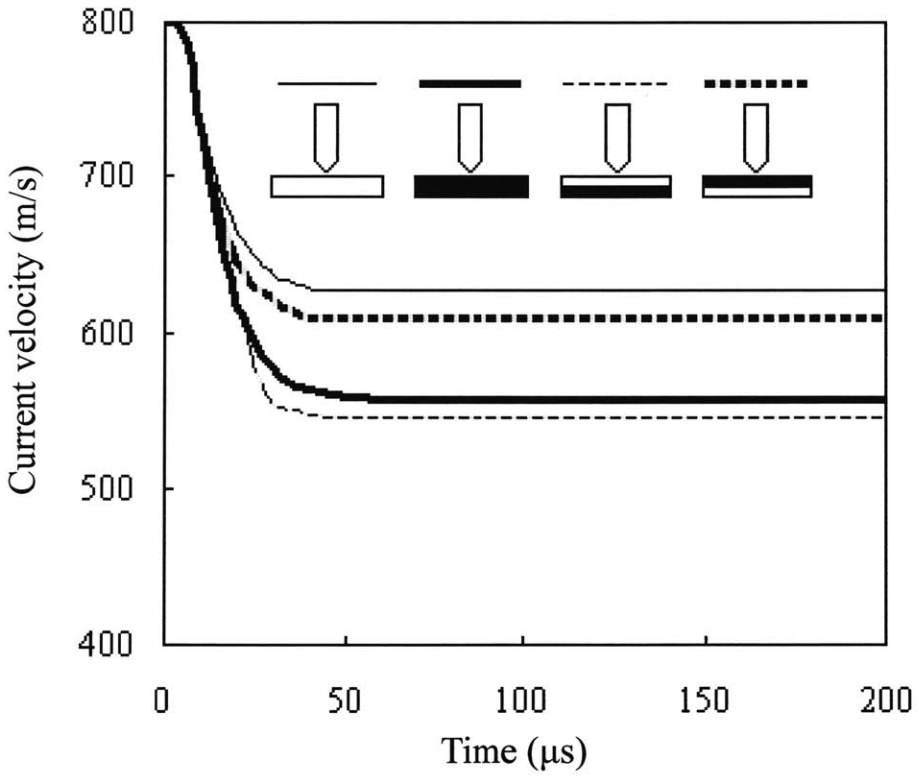

Fig. 4.26: Time history of the transient velocity of the light conical-nose projectile at V_0 = 800m/s

4.4 Light flat-nose projectile

In this section, a flat-nose projectile of the mass M_0 = 30g and the diameter d = 12mm is considered.

Figures 4.27-4.30 show the perforation processes of the monolithic and double-layered shields of different material combinations impacted by the light flat-nose projectile at V_0 = 400m/s.

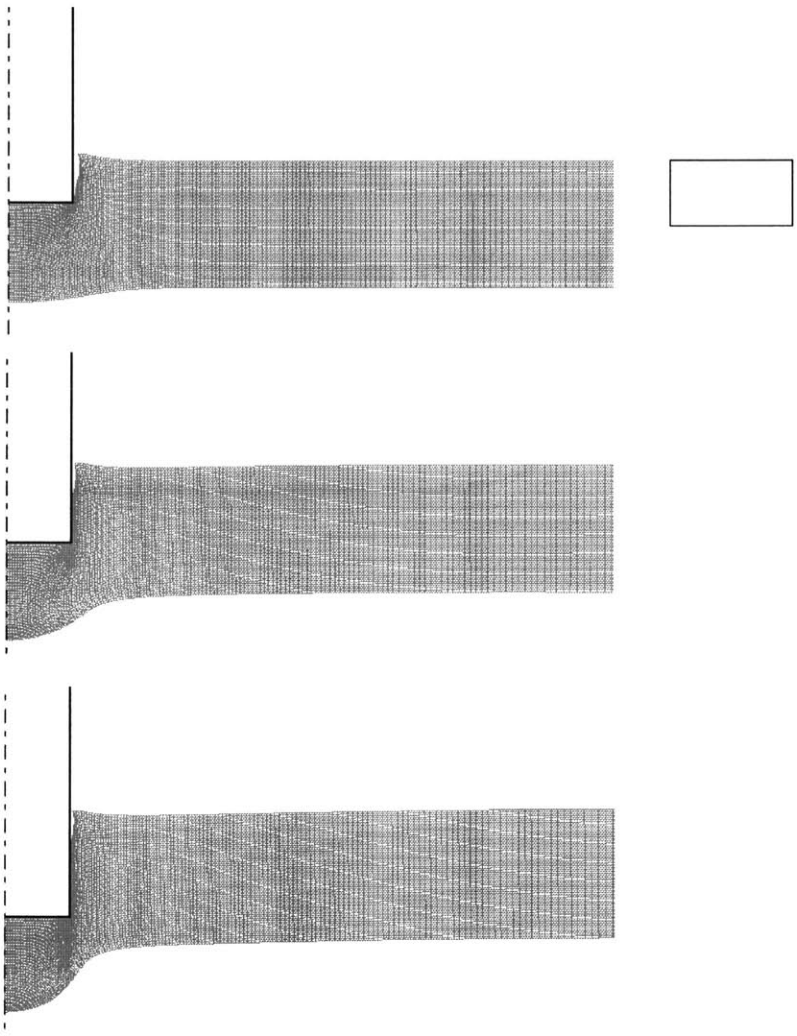

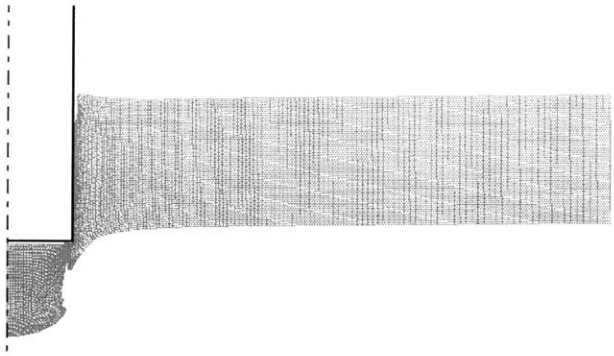

Fig. 4.27: The perforation process of the monolithic plate of high ductility material impacted by the light flat-nose projectile at $V_0 = 400$m/s

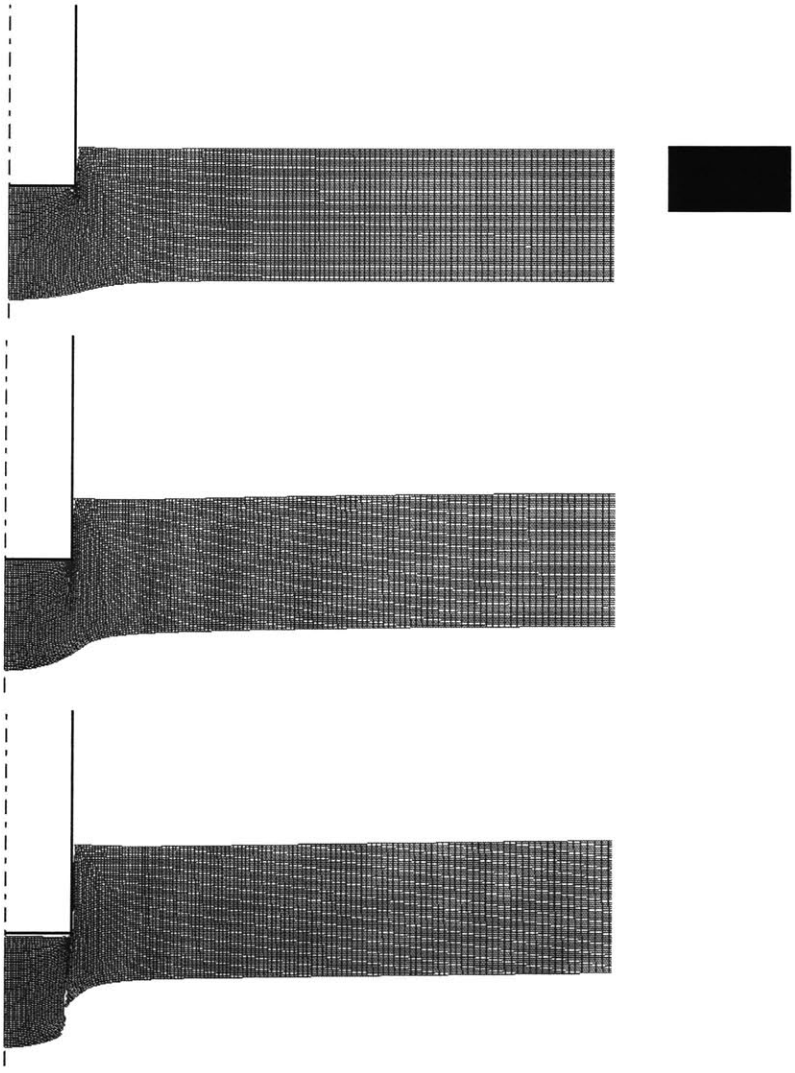

Fig. 4.28: The perforation process of the monolithic plate of low ductility material impacted by the light flat-nose projectile at $V_0 = 400$m/s

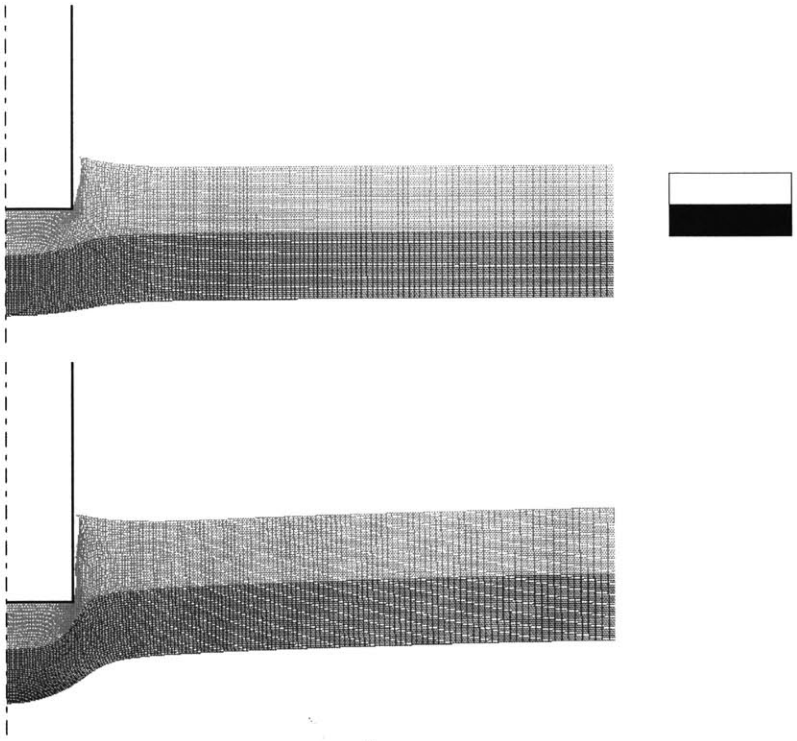

Fig. 4.29: The perforation process of the double-layered shield with the upper layer of high ductility material and lower layer of low ductility material impacted by the light flat-nose projectile at $V_0 = 400$m/s

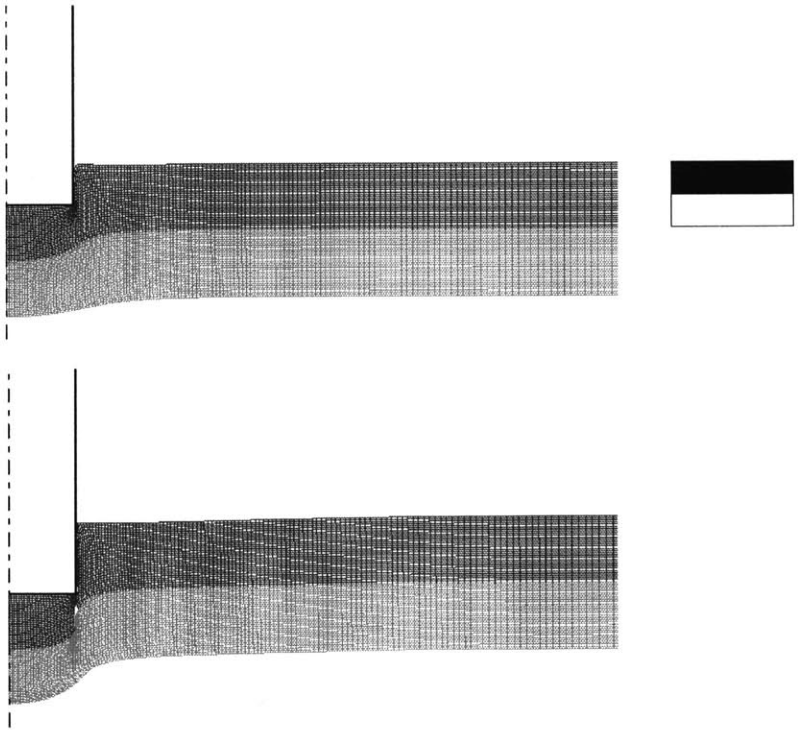

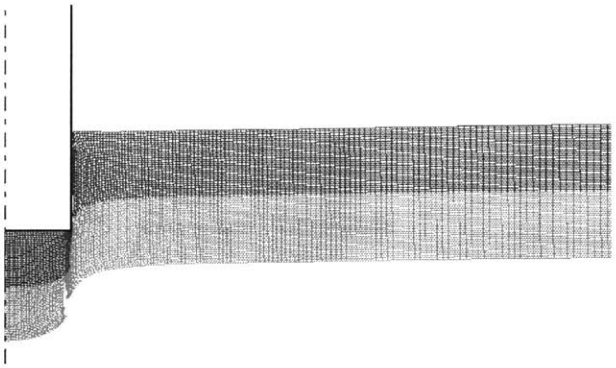

Fig. 4.30: The perforation process of the double-layered shield with the upper layer of low ductility material and lower layer of high ductility material impacted by the light flat-nose projectile at V_0 = 400m/s

It can be observed that the failure mode is shear plugging for the monolithic plates of high ductility material and low ductility material and the double-layered shield with the upper layer of low ductility material and the lower layer of high ductility material. For the three types of shields, plastic deformation is localized in the impact zone, this is similar to the preceding section that impacted by the heavy conical-nose projectile at V_0 = 400m/s. Actually, V_0 = 400m/s is the ballistic limit of the monolithic plate of low ductility material. For the double-layered shield with the upper layer of high ductility material and the lower layer of low ductility material, the projectile is stopped at an early stage. It can be seen from Fig. 4.29 that the upper layer tends to fail by tensile tearing.

The time history of the transient velocity of the light flat-nose projectile impacted at fours types of shields at V_0 = 400m/s is shown in Fig. 4.31. According to our simulation results, the double-layered shield with the upper layer of high ductility material and the lower layer of low ductility material is the best configuration in perforation resistance among all types of shields, while the double-layered shield with the upper layer of low ductility material and the lower layer of high ductility material is the worst one.

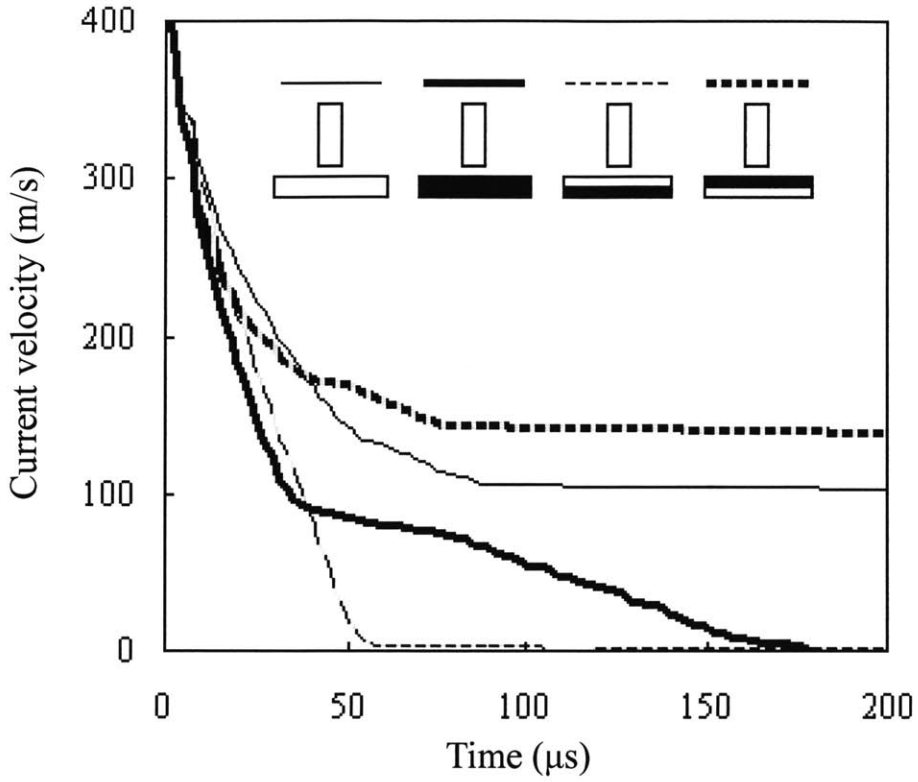

Fig. 4.31: Time history of the transient velocity of the light flat-nose projectile at V_0 = 400m/s

When the impact velocity is increased to 800m/s, the failure modes are similar to that of the preceding section that impacted by the heavy conical-nose projectile at V_0 = 800m/s. Figures 4.32-4.35 show the perforation process of each type of shield. It can be observed that the plastic deformation of the monolithic plate of low ductility material becomes larger at high velocity. Therefore the energy absorption advantage of low ductility material is increased under this condition.

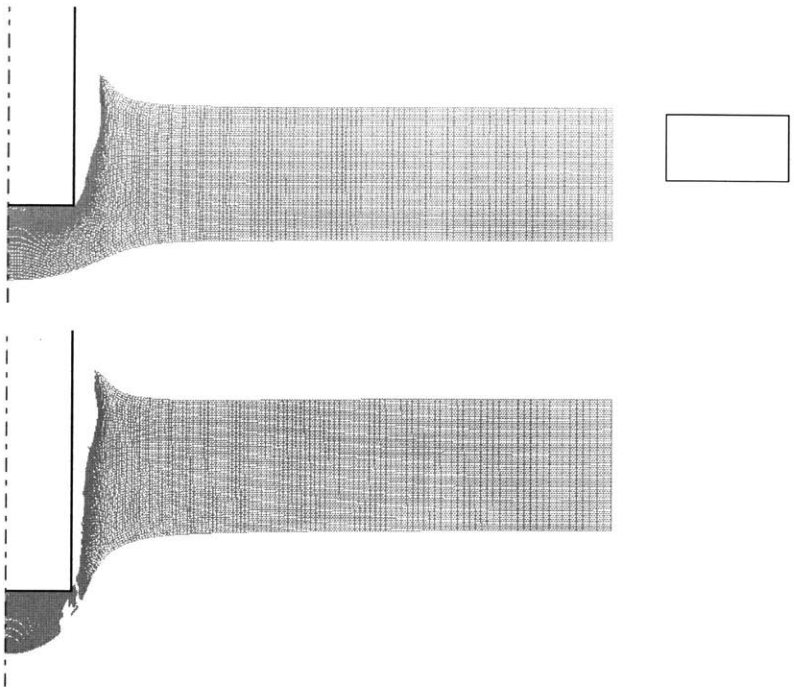

Fig. 4.32: The perforation process of the monolithic plate of high ductility material impacted by the light flat-nose projectile at V_0 = 800m/s

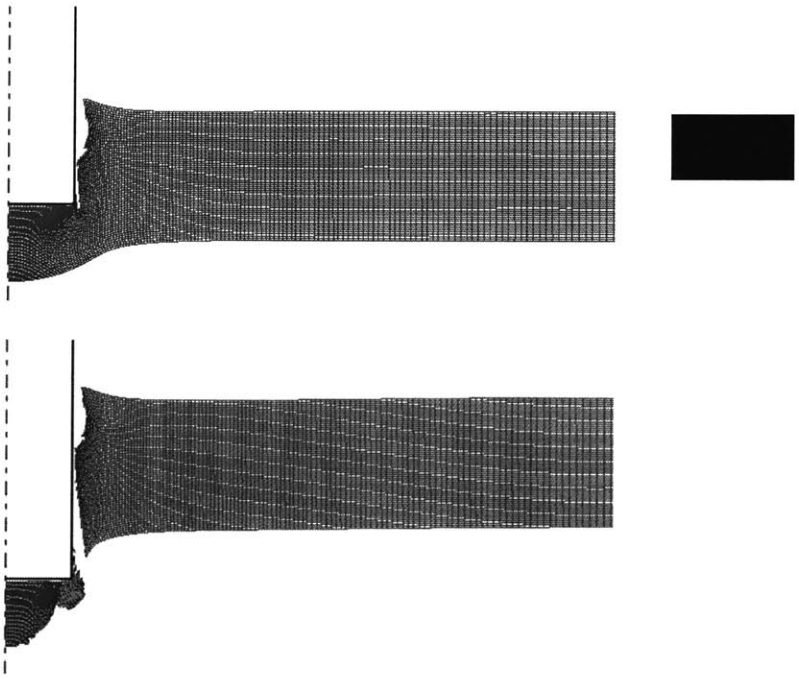

Fig. 4.33: The perforation process of the monolithic plate of low ductility material impacted by the light flat-nose projectile at V_0 = 800m/s

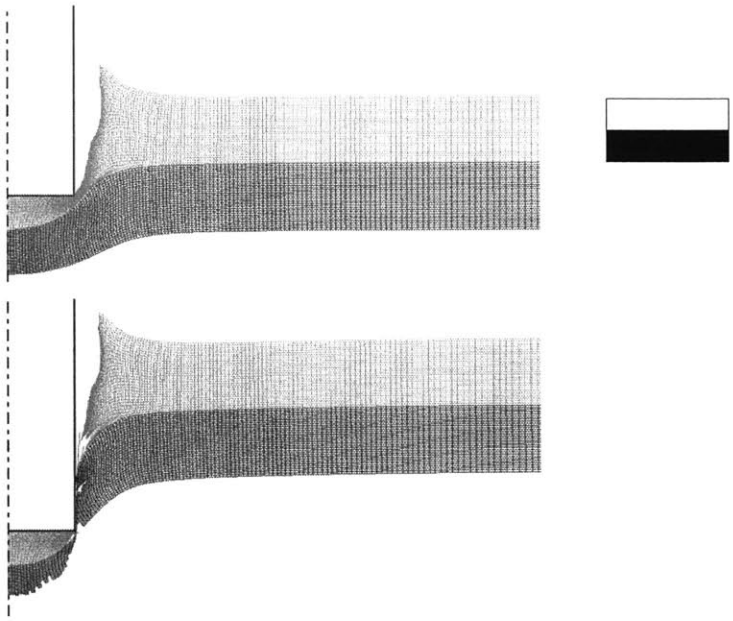

Fig. 4.34: The perforation process of the double-layered shield with the upper layer of high ductility material and lower layer of low ductility material impacted by the light flat-nose projectile at V_0 = 800m/s

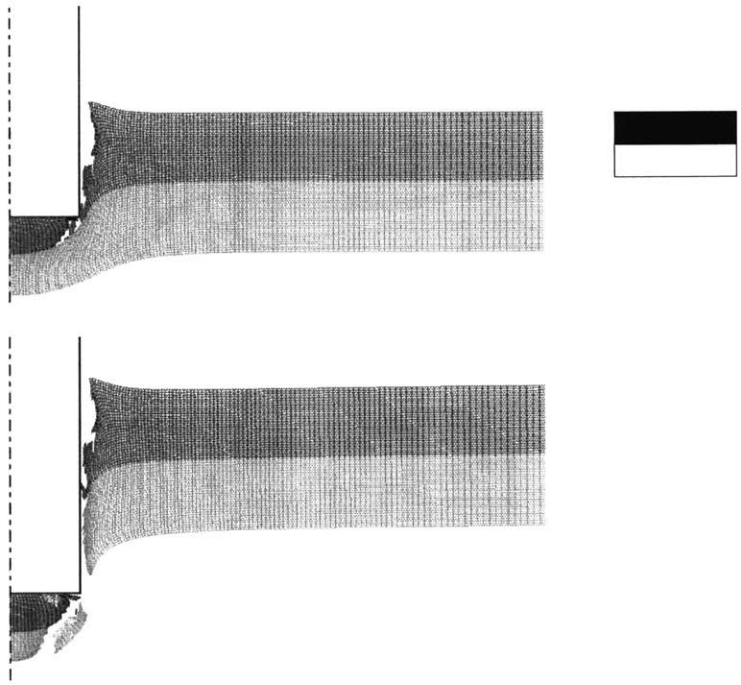

Fig. 4.35: The perforation process of the double-layered shield with the upper layer of low ductility material and lower layer of high ductility material impacted by the light flat-nose projectile at V_0 = 800m/s

Figure 4.36 shows the time history of the transient velocity of the light flat-nose projectile. At high impact velocity, the perforation resistance mainly depends on the ductility, while the fracture property is no so important. Anyway, the perforation resistance of the double-layered shield with the upper layer of high ductility material and the lower layer of low ductility material is still slightly superior than the double-layered shield with the upper layer of low ductility material and the lower layer of high ductility material.

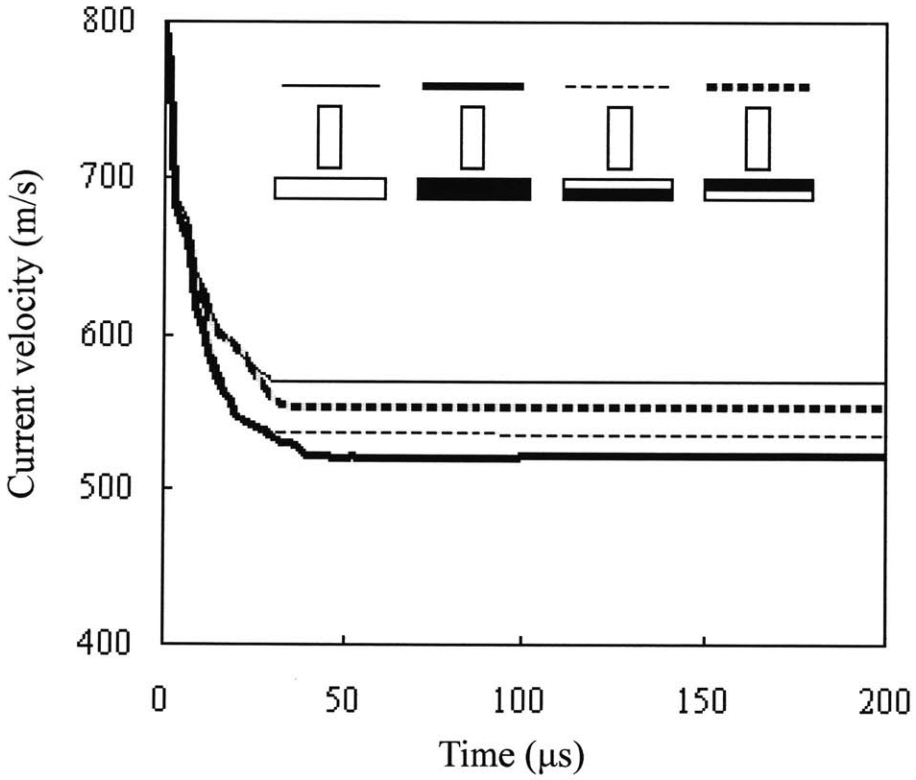

Fig. 4.36: Time history of the transient velocity of the light flat-nose projectile at V_0 = 800m/s

Chapter 5
Ballistic Resistance of Blast Resistance Adaptive Sandwich

5.1 Heavy flat-nose projectile

In this section, the BRAS shields and the monolithic plates under the impact of a flat-nose projectile of the mass M_0 = 200g and the diameter d = 24mm is studied.

At first, let us consider the impact velocity of 400m/s. Figures 5.1 and 5.2 show the perforation process of the BRAS shields impacted normally by the heavy flat-nose projectile towards the top and bottom joints at V_0 = 400m/s. It can be observed that, for both impact positions, the top layer of the BRAS shield fails by shear plugging, while the sandwich core and bottom layer fails by tensile tearing. Differently, the monolithic plate fails by shearing plugging under the same impact condition, see Fig. 5.3. As we have mentioned earlier, the tensile tearing is a better resisting mode than shear plugging. Therefore, the BRAS shield is slightly superior than the monolithic plate in perforation resistance under the impact of the heavy flat-nose projectile at V_0 = 400m/s.

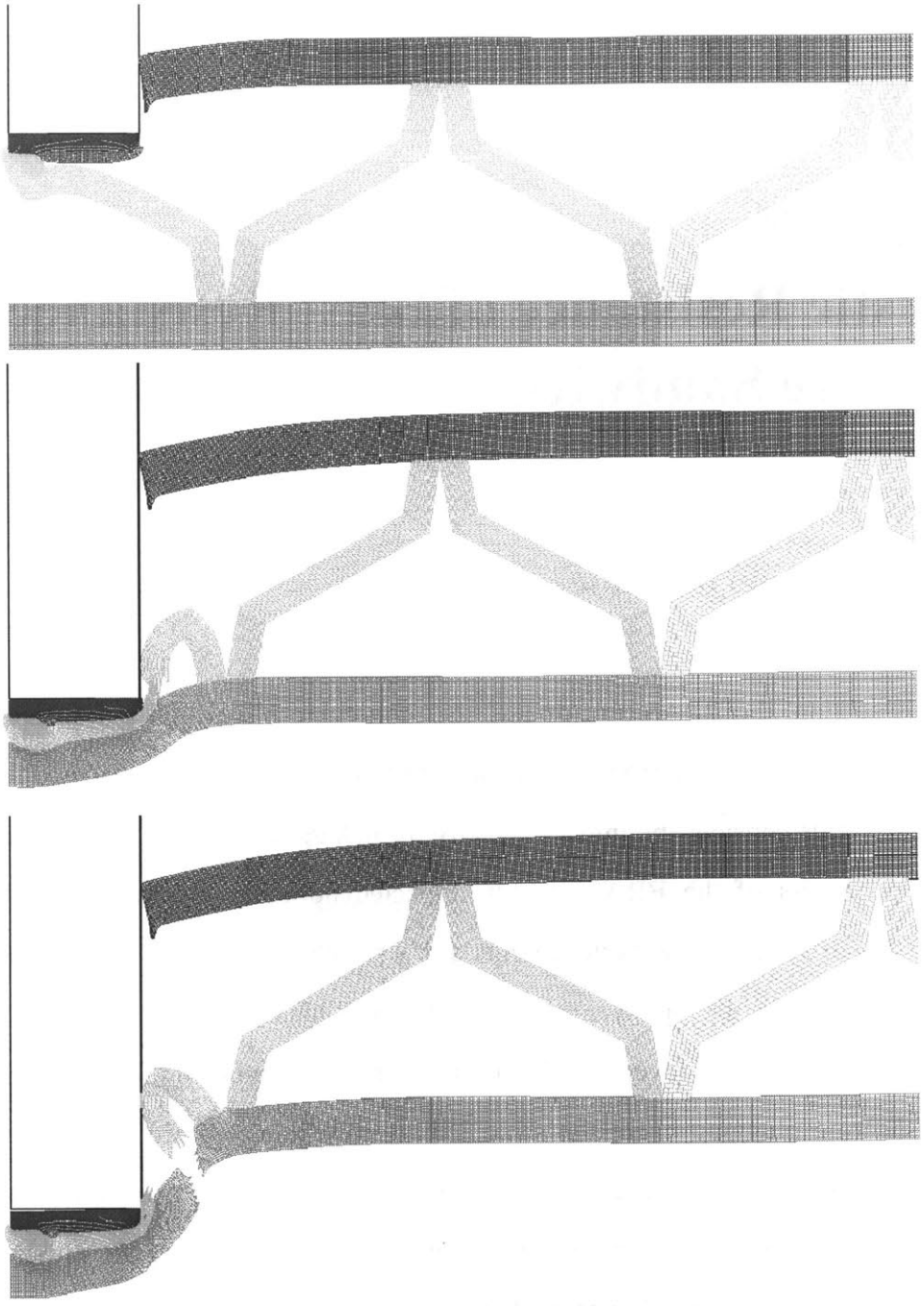

Fig. 5.1: The perforation process of the BRAS shield impacted normally by the heavy flat-nose projectile towards the top joint at V_0 = 400m/s.

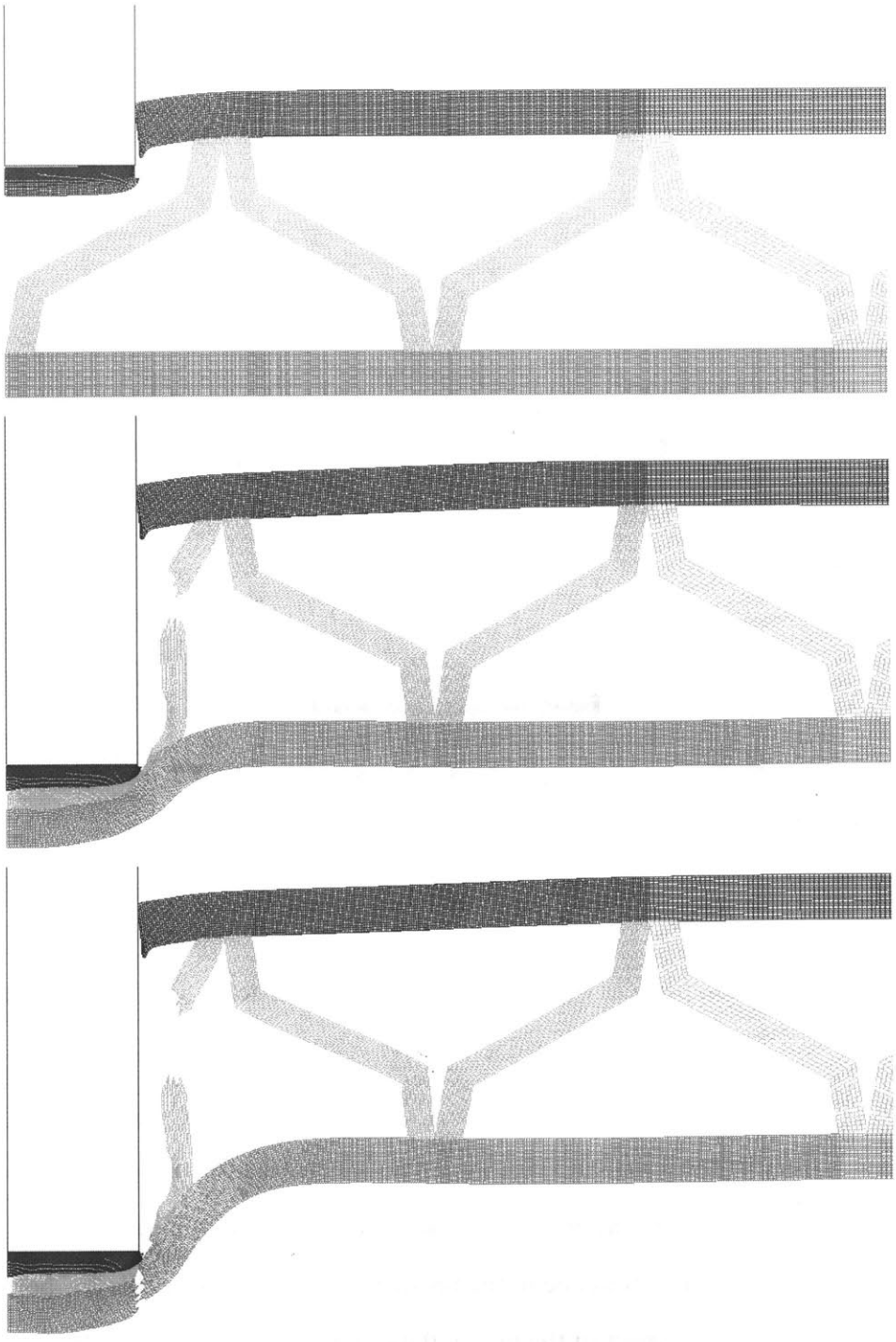

Fig. 5.2: The perforation process of the BRAS shield impacted normally by the heavy flat-nose projectile towards the bottom joint at $V_0 = 400$m/s.

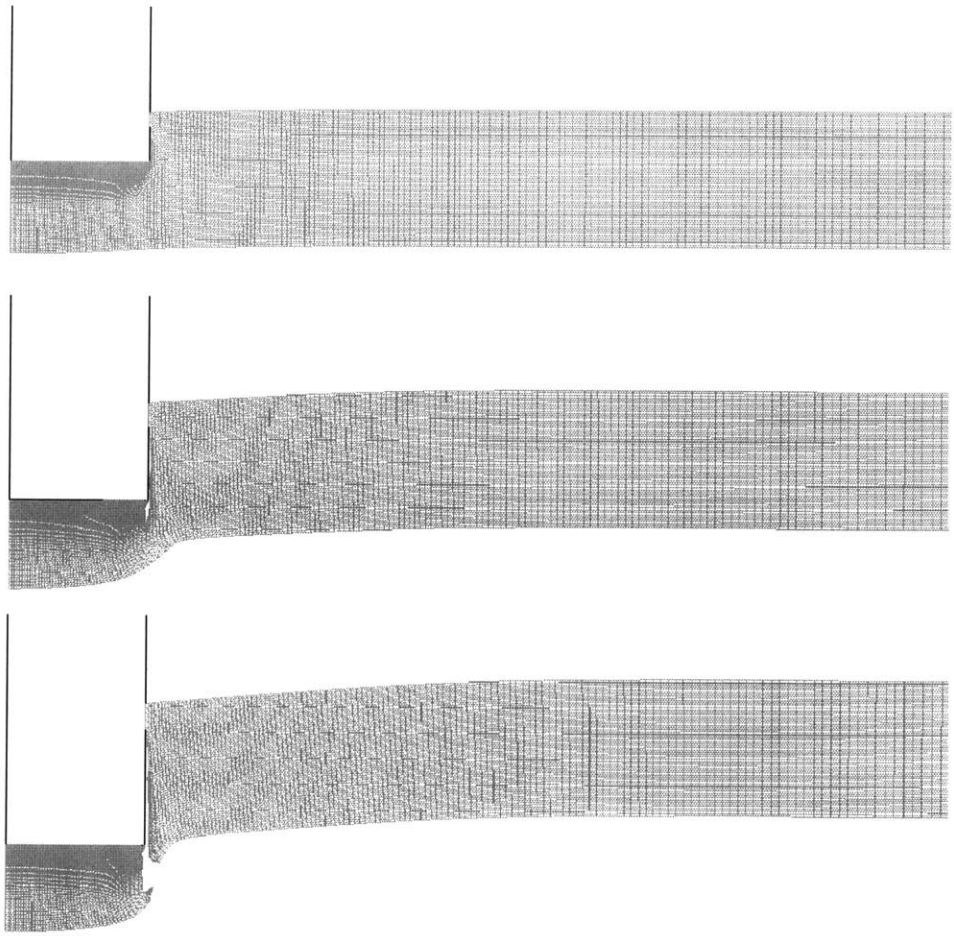

Fig. 5.3: The perforation process of the monolithic plate impacted normally by the heavy flat-nose projectile at V_0 = 400m/s.

The time history of the transient velocity of the heavy flat-nose projectile at V_0 = 400m/s for the BRAS shields and the monolithic plates is shown in Fig. 5.4. It can be observed that there is small difference in the residual velocity of projectile for both configurations. Under the impact of the heavy flat-nose projectile at V_0 = 400m/s, the BRAS shield is slightly superior to the monolithic plate in perforation resistance.

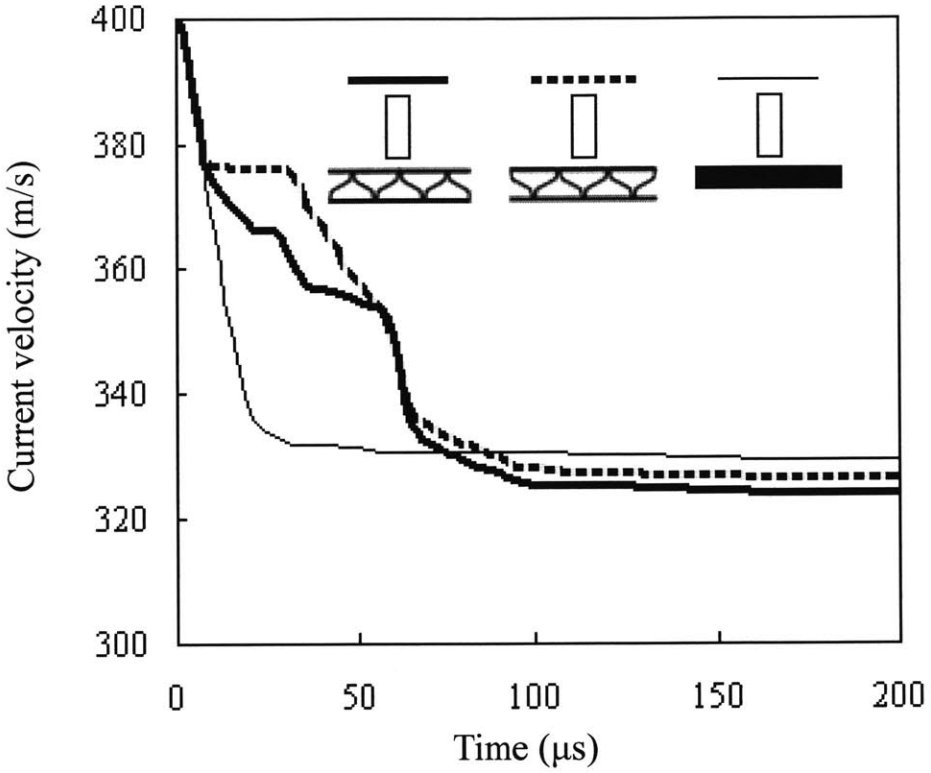

Fig. 5.4: Time history of the transient velocity of the heavy flat-nose projectile at V_0 = 400m/s

Now let us increase the impact velocity to 800m/s. Figures 5.5-5.7 show the perforation processes of the BRAS shields and the monolithic plates impacted normally by the heavy flat-nose projectile at V_0 = 800m/s. It can be observed that both the BRAS shields and the monolithic plates fail by shear plugging. The three configurations are identical in perforation resistance against the heavy flat-nose projectile at V_0 = 800m/s, see Fig. 5.8.

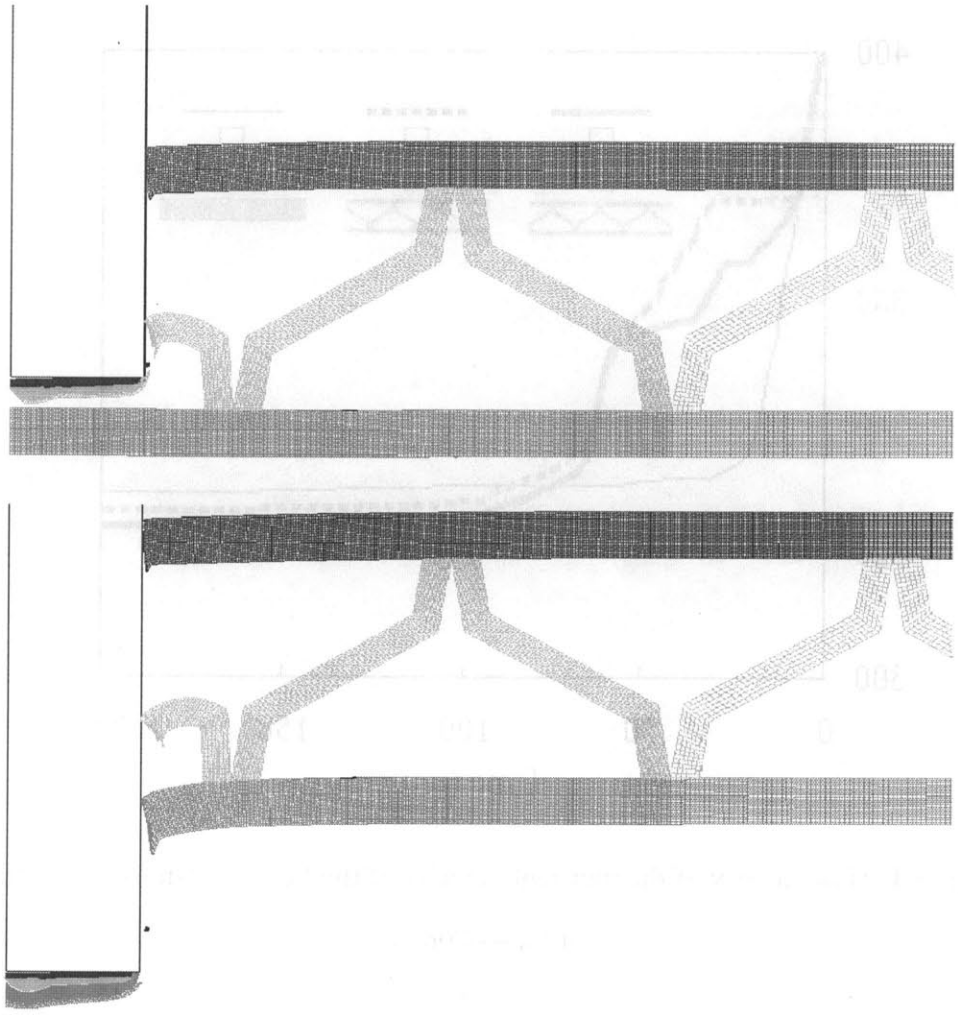

Fig. 5.5: The perforation process of the BRAS shield impacted normally by the heavy flat-nose projectile towards the top joint at V_0 = 800m/s.

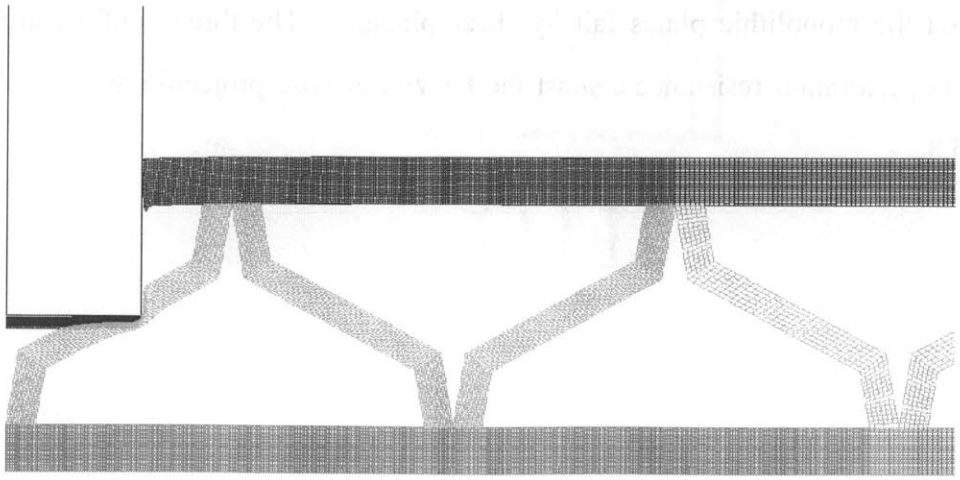

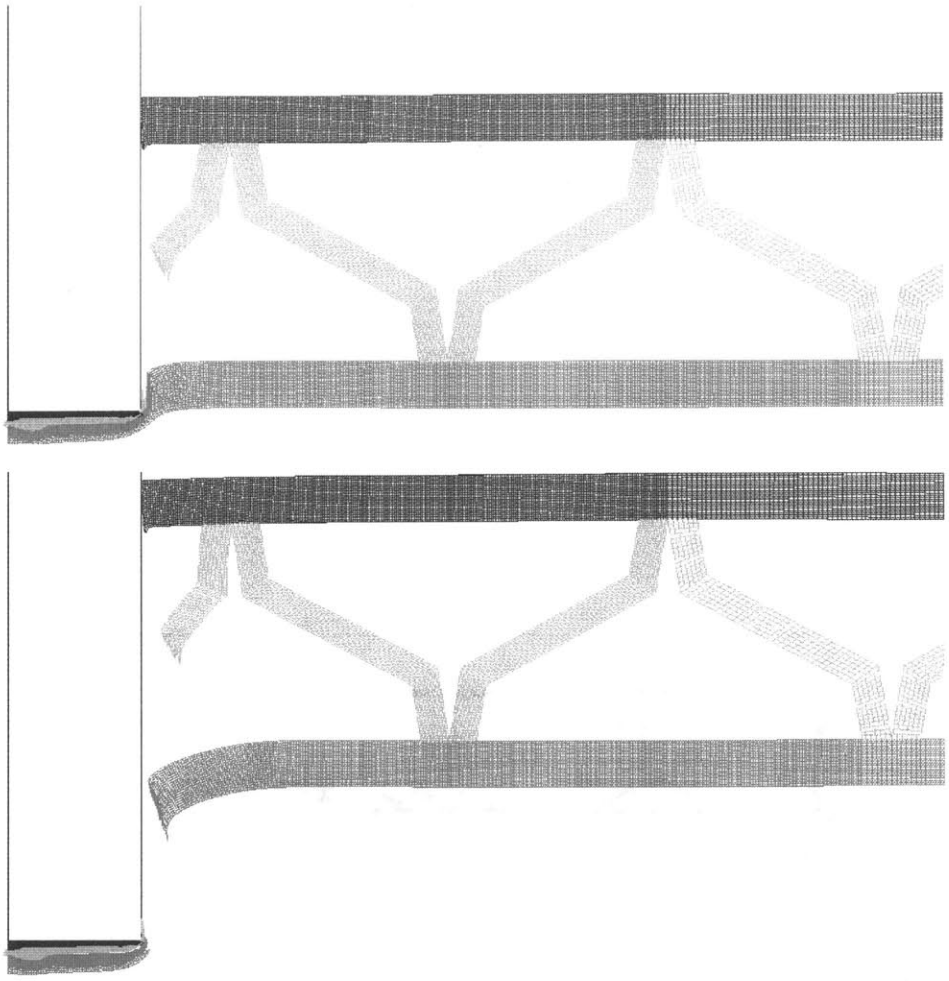

Fig. 5.6: The perforation process of the BRAS shield impacted normally by the heavy flat-nose projectile towards the bottom joint at V_0 = 800m/s.

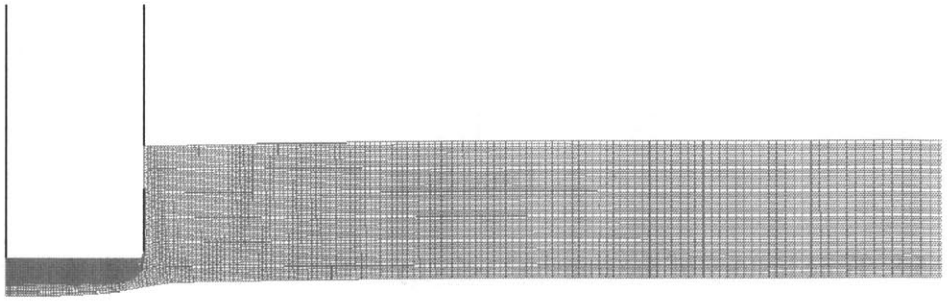

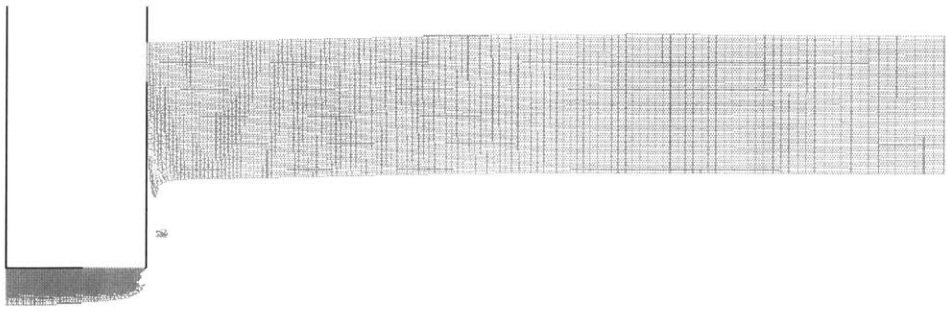

Fig. 5.7: The perforation process of the monolithic plate impacted normally by the heavy flat-nose projectile at V_0 = 800m/s.

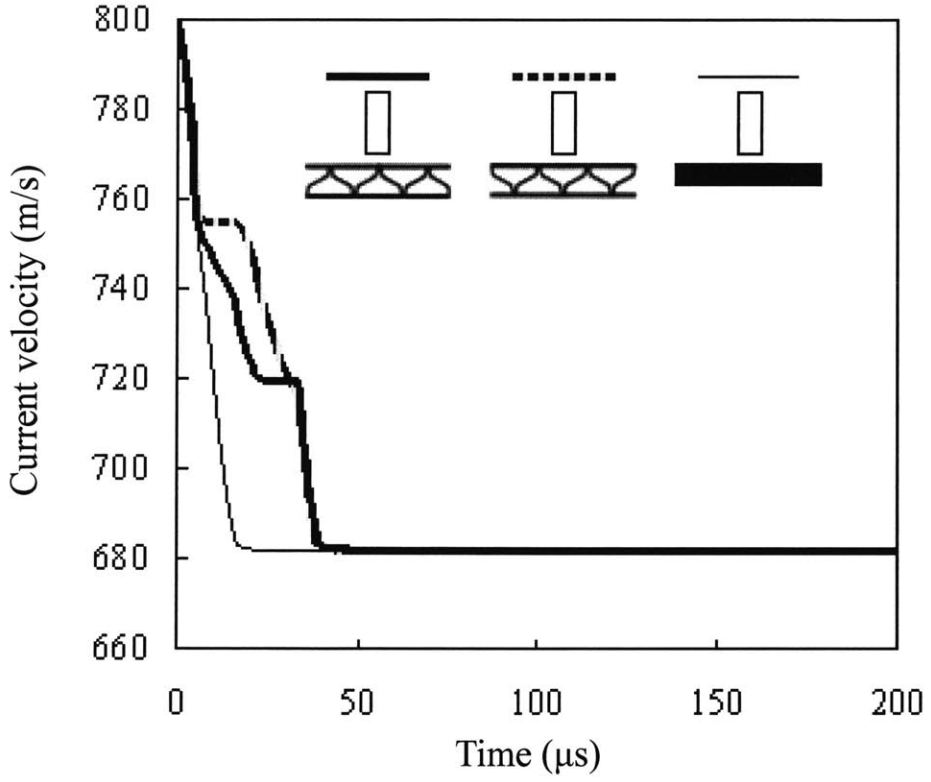

Fig. 5.8: Time history of the transient velocity of the heavy flat-nose projectile at V_0 = 800m/s

5.2 Heavy conical-nose projectile

In this section, a conical-nose projectile of the mass M_0 = 200g and the diameter d = 24mm is considered. Figures 5.9-5.11 show the perforation process of the BRAS shields impacted normally by the heavy conical-nose projectile towards the top and bottom joints at V_0 = 400m/s. It can be observed that the materials in the impacted zone are pushed aside as the projectile penetrates through the thickness. Both shields fail by ductile hole enlargement, which is thought of the worst mode for plastic energy dissipation. At the impact position towards top joint of the BRAS shield, the sandwich core folds and braking of bottom joint contribute small energy dissipation. At the impact position towards the bottom joint of the BRAS shield, the sandwich core has almost no contribution to plastic energy dissipation.

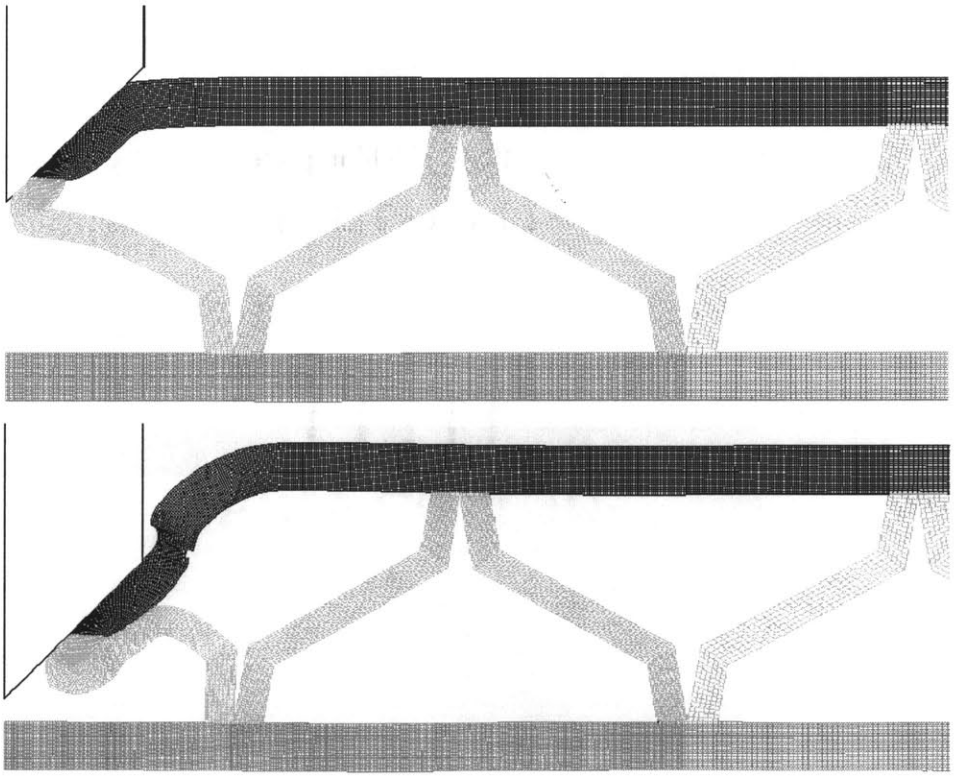

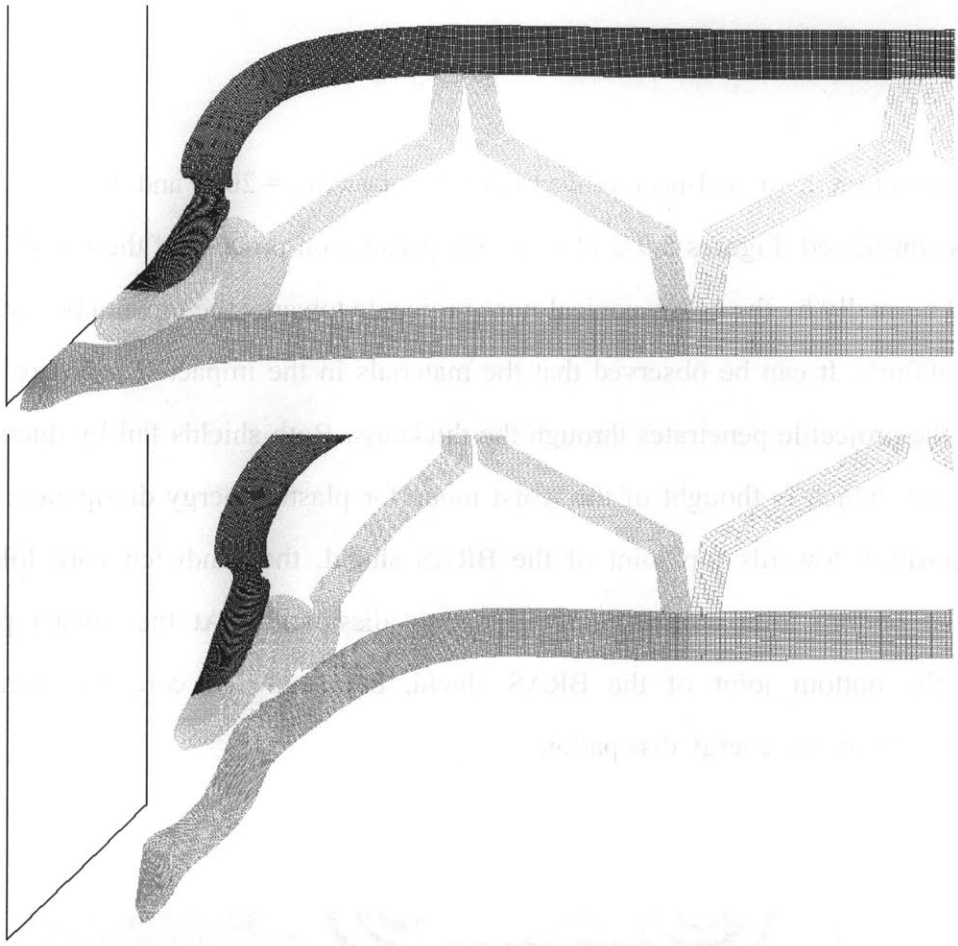

Fig. 5.9: The perforation process of the BRAS shield impacted normally by the heavy conical-nose projectile towards the top joint at $V_0 = 400$m/s.

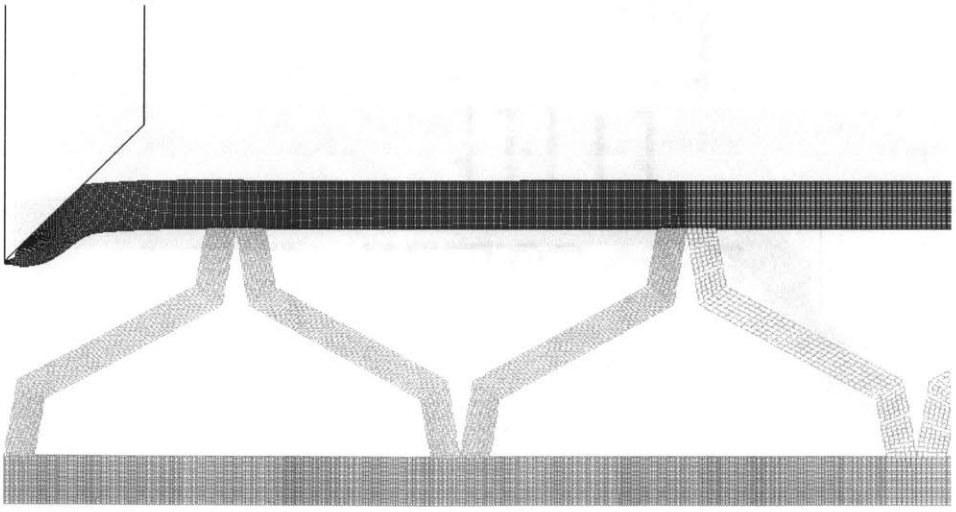

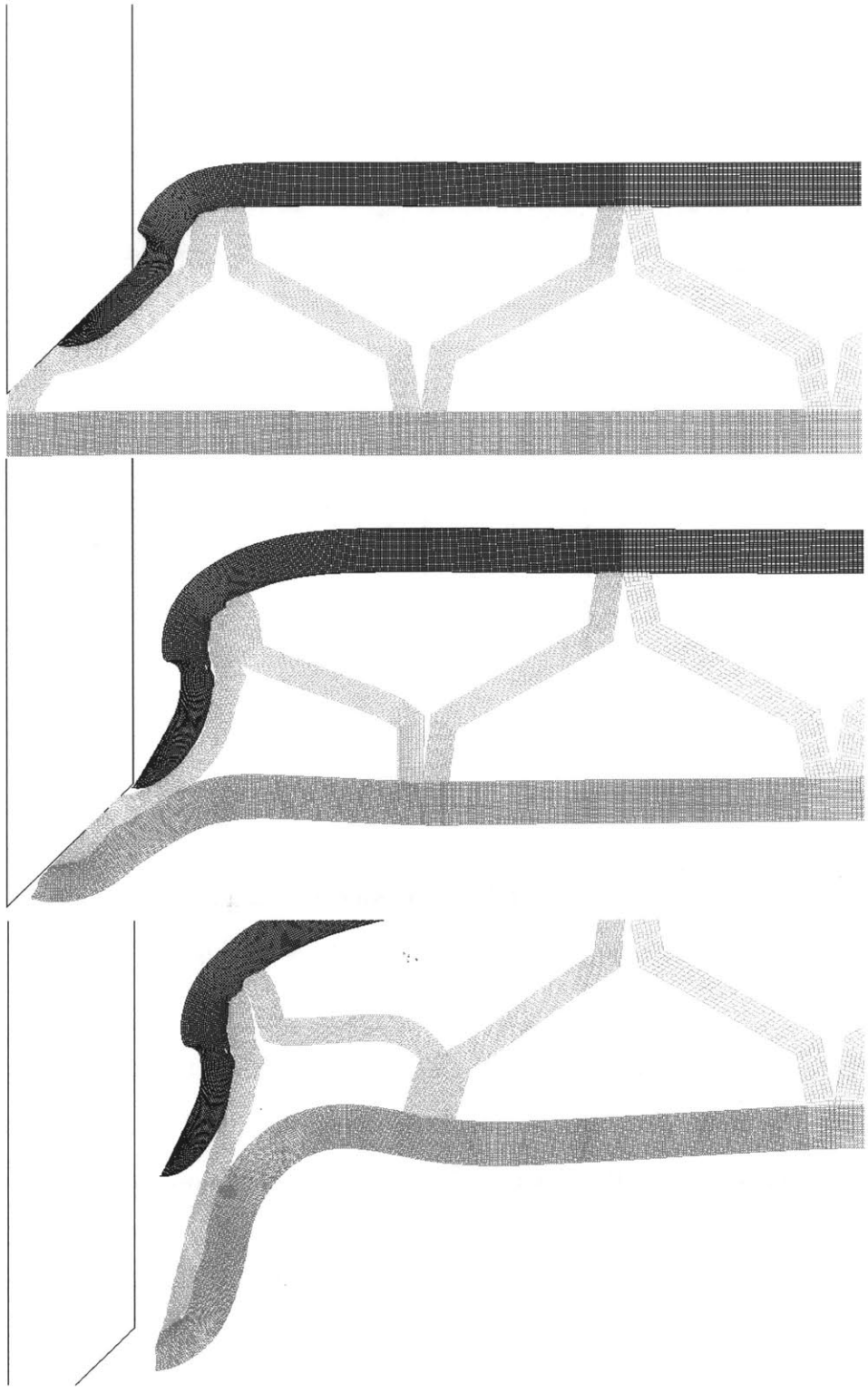

Fig. 5.10: The perforation process of the BRAS shield impacted normally by the heavy conical-nose projectile towards the bottom joint at V_0 = 400m/s.

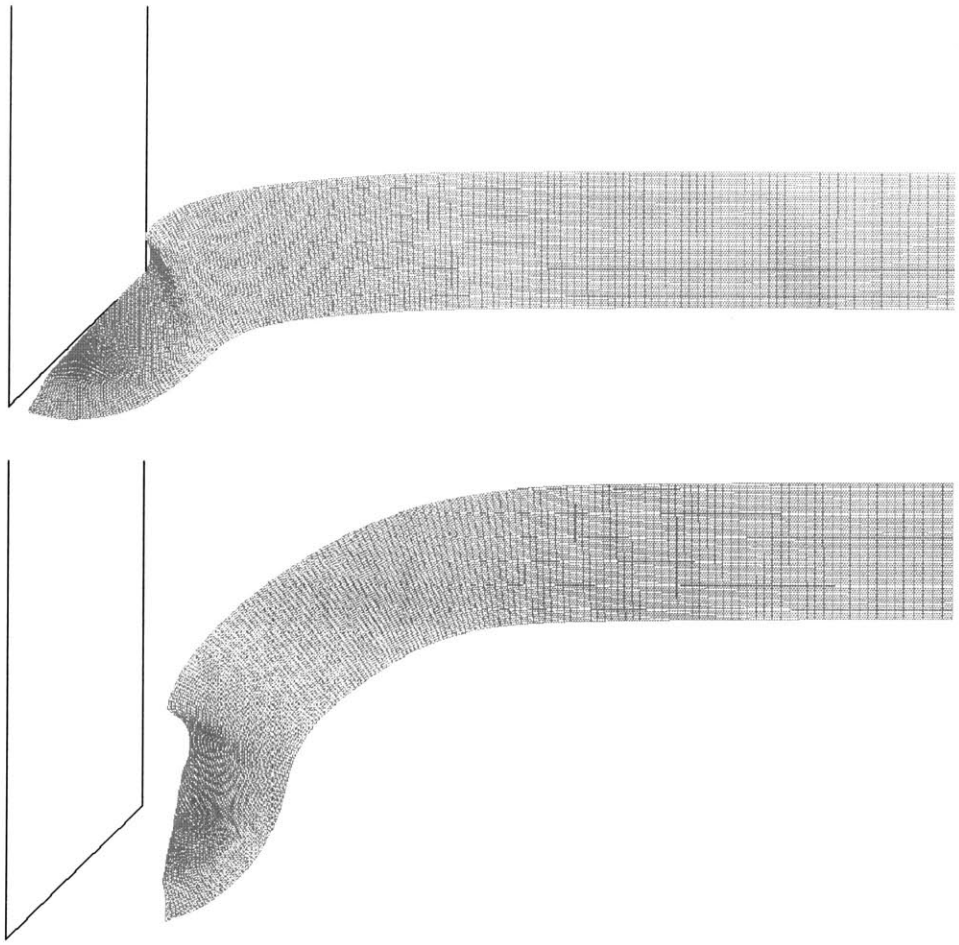

Fig. 5.11: The perforation process of the monolithic plate impacted normally by the heavy conical-nose projectile at $V_0 = 400$m/s.

Anyway, the empty inner structure is disadvantageous for the transition of deformation. Therefore, the BRAS shield is worse than the monolithic plate in perforation resistance under the impact of the heavy conical-nose projectile at $V_0 = 400$m/s, see Fig. 5.12.

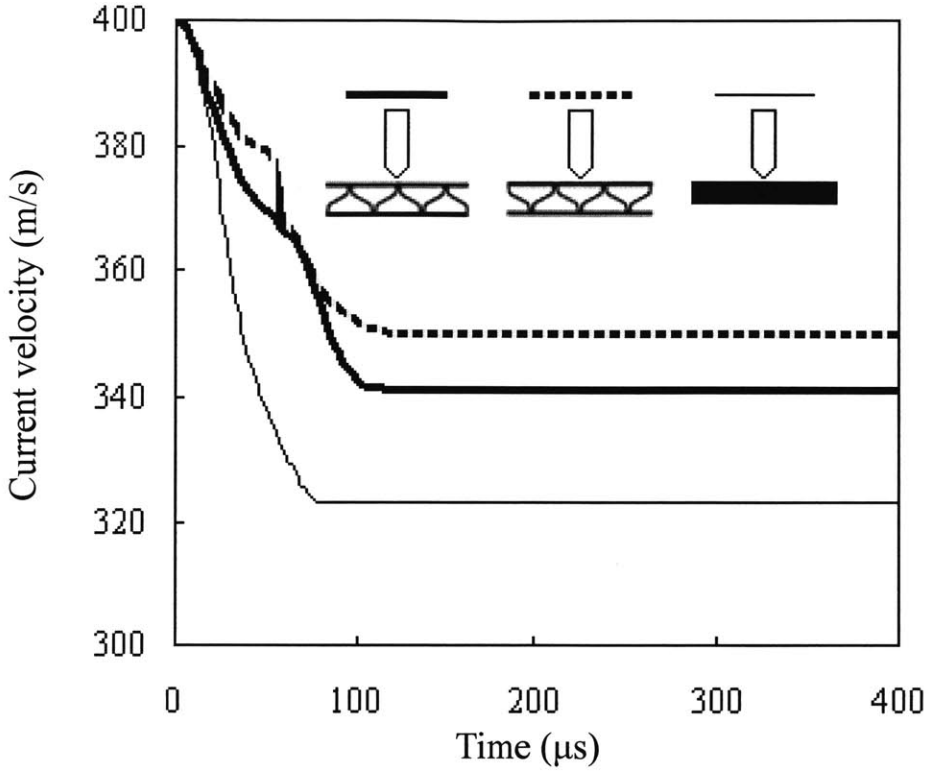

Fig. 5.12: Time history of the transient velocity of the heavy conical-nose projectile at $V_0 = 400$m/s

When the impact velocity is increased to 800m/s, the results are similar. Figures 5.13 show the perforation process of the BRAS shields impacted normally by the heavy conical-nose projectile towards the top joint at $V_0 = 800$m/s. It can be observed that the top layer fails by tensile tearing, while the sandwich core and bottom layer fail by ductile hole enlargement. Again, it can be found that the empty inner structure is disadvantageous for the transmission of deformation.

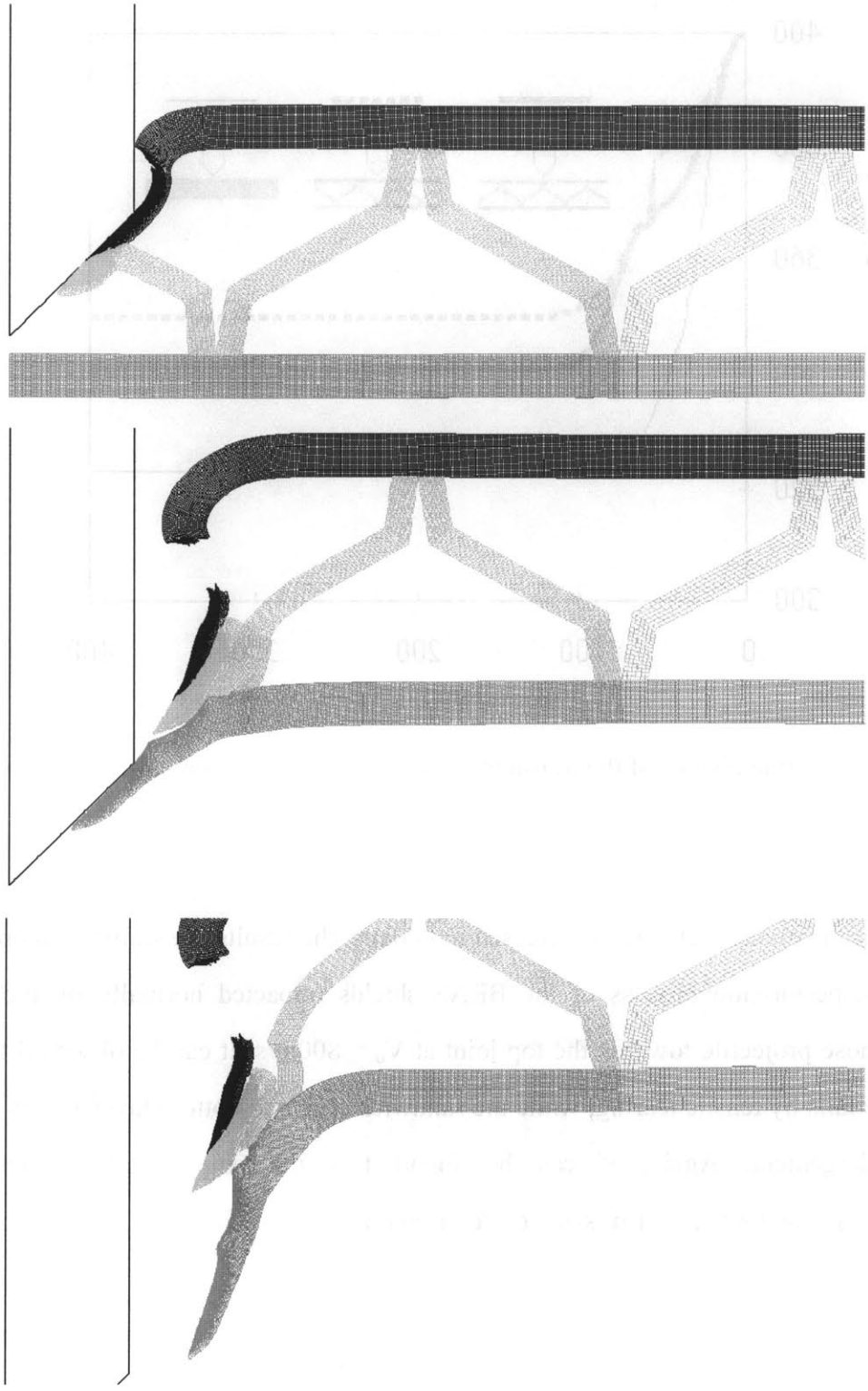

Fig. 5.13: The perforation process of the BRAS shield impacted normally by the heavy conical-nose projectile towards the top joint at V_0 = 800m/s.

Figure 5.14 shows the perforation process of the monolithic plate impacted normally by the heavy conical-nose projectile at V_0 = 800m/s. Although the monolithic plate fails by ductile hole enlargement, the plastic deformation of the monolithic plate is larger than that of the BRAS shield. However, the tensile tearing of top layer of the BRAS shield absorbed more energy than the equivalent part of the monolithic plate. Therefore, there is only small difference in the perforation resistance of the BRAS shields and the monolithic plates. The time history of the transient velocity of the heavy conical-nose projectile at V_0 = 800m/s for both configurations is shown in Fig. 5.15.

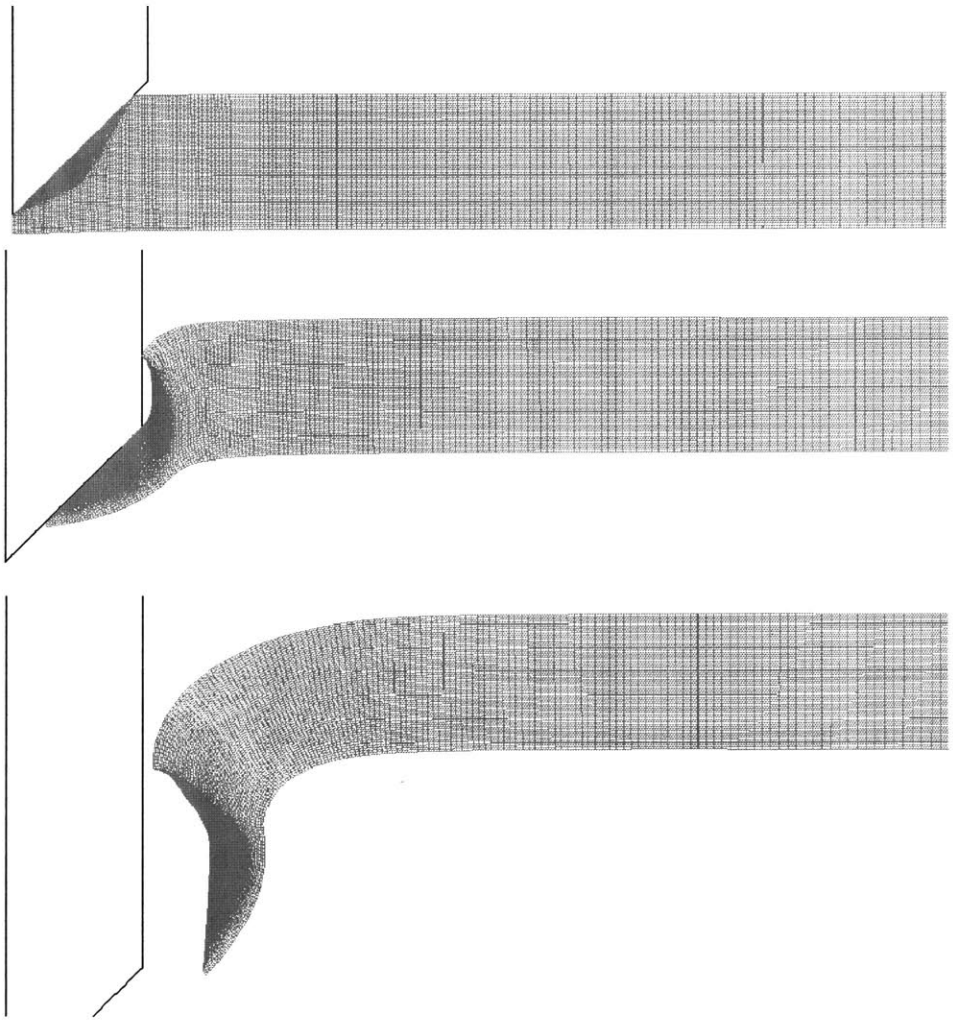

Fig. 5.14: The perforation process of the monolithic plate impacted normally by the heavy conical-nose projectile at V_0 = 800m/s.

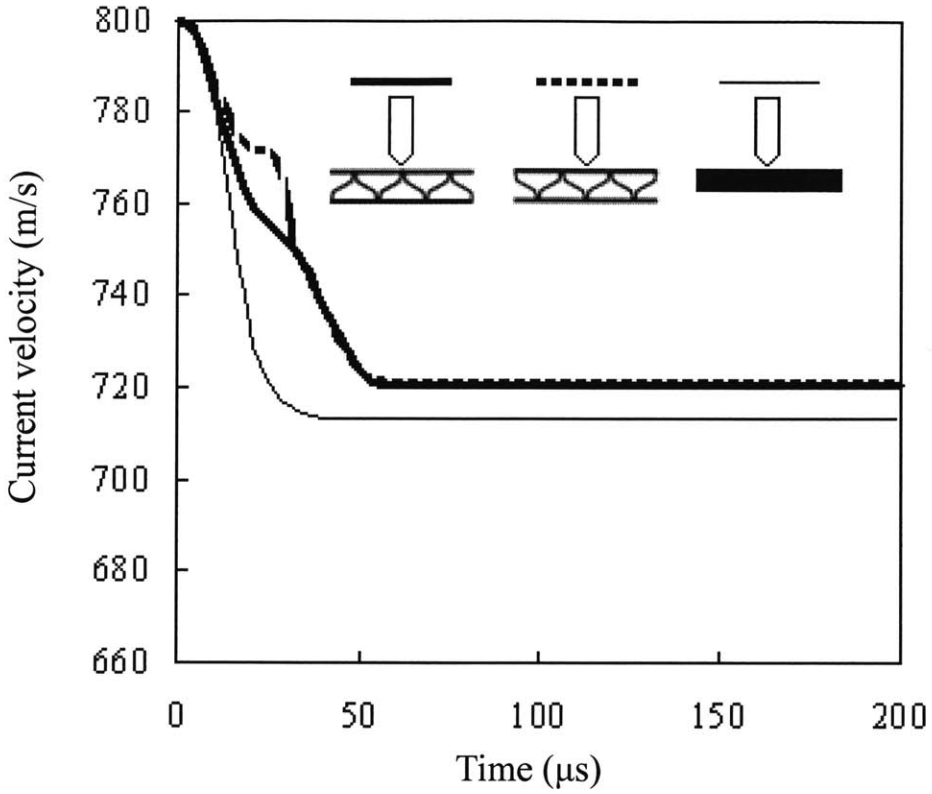

Fig. 5.15: Time history of the transient velocity of the heavy conical-nose projectile at V_0 = 800m/s

5.3 Light flat-nose projectile

In this section, the mass and diameter of flat-nose projectile is decreased to M_0 = 30g and d = 12mm. The perforation processes of the BRAS shields impacted normally by the light flat-nose projectile at different positions at V_0 = 400m/s is shown in Fig. 5.16-5.17. For the impact position towards the top joint, the top layer fails by shear plugging, while the bottom layer fails by tensile tearing, it is similar to the preceding case impacted by the heavy flat-nose projectile. For the impact position of bottom joint, the sandwich core absorbed some energy through tensile tearing.

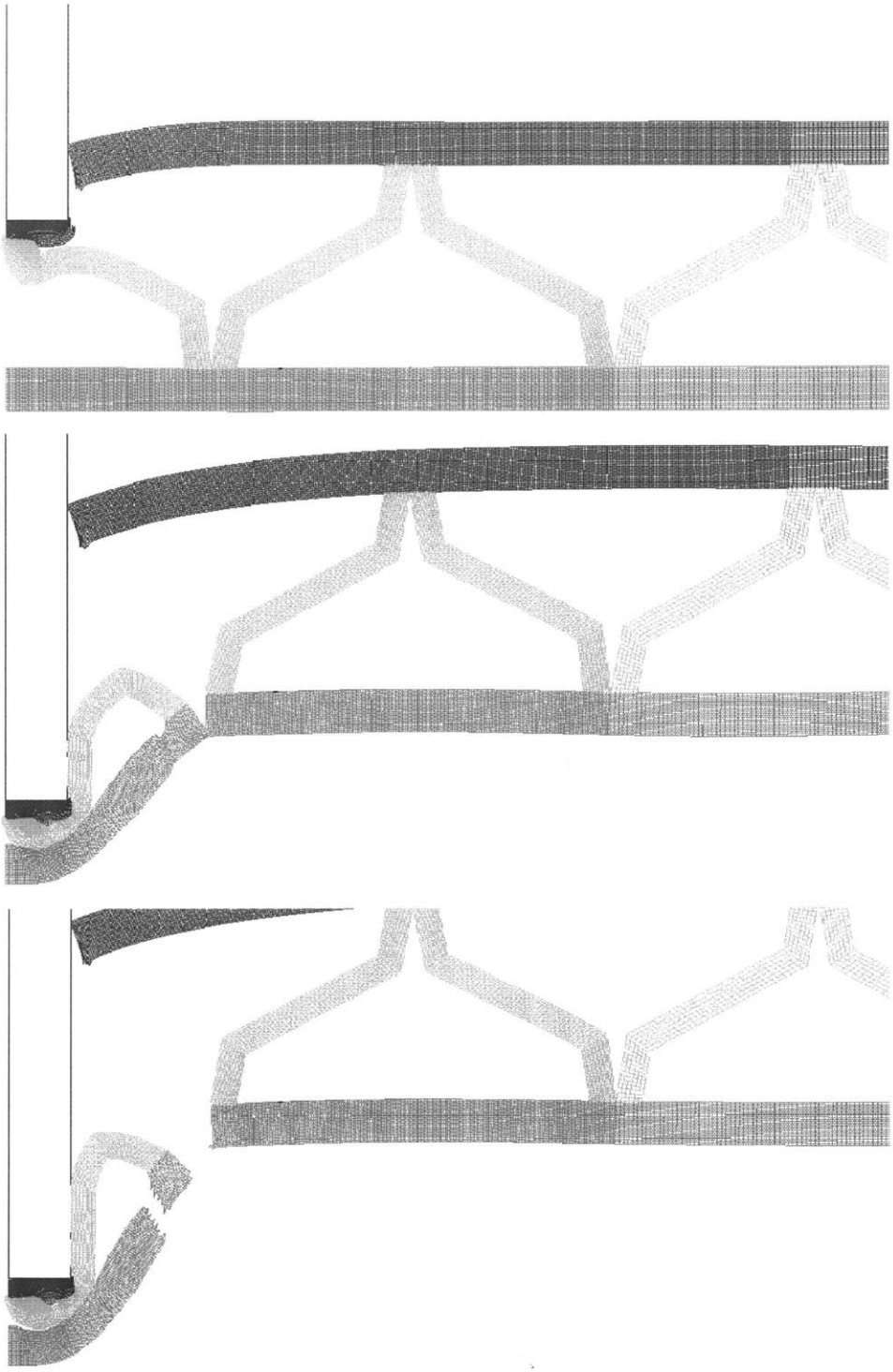

Fig. 5.16: The perforation process of the BRAS shield impacted normally by the light flat-nose projectile towards the top joint at V_0 = 400m/s.

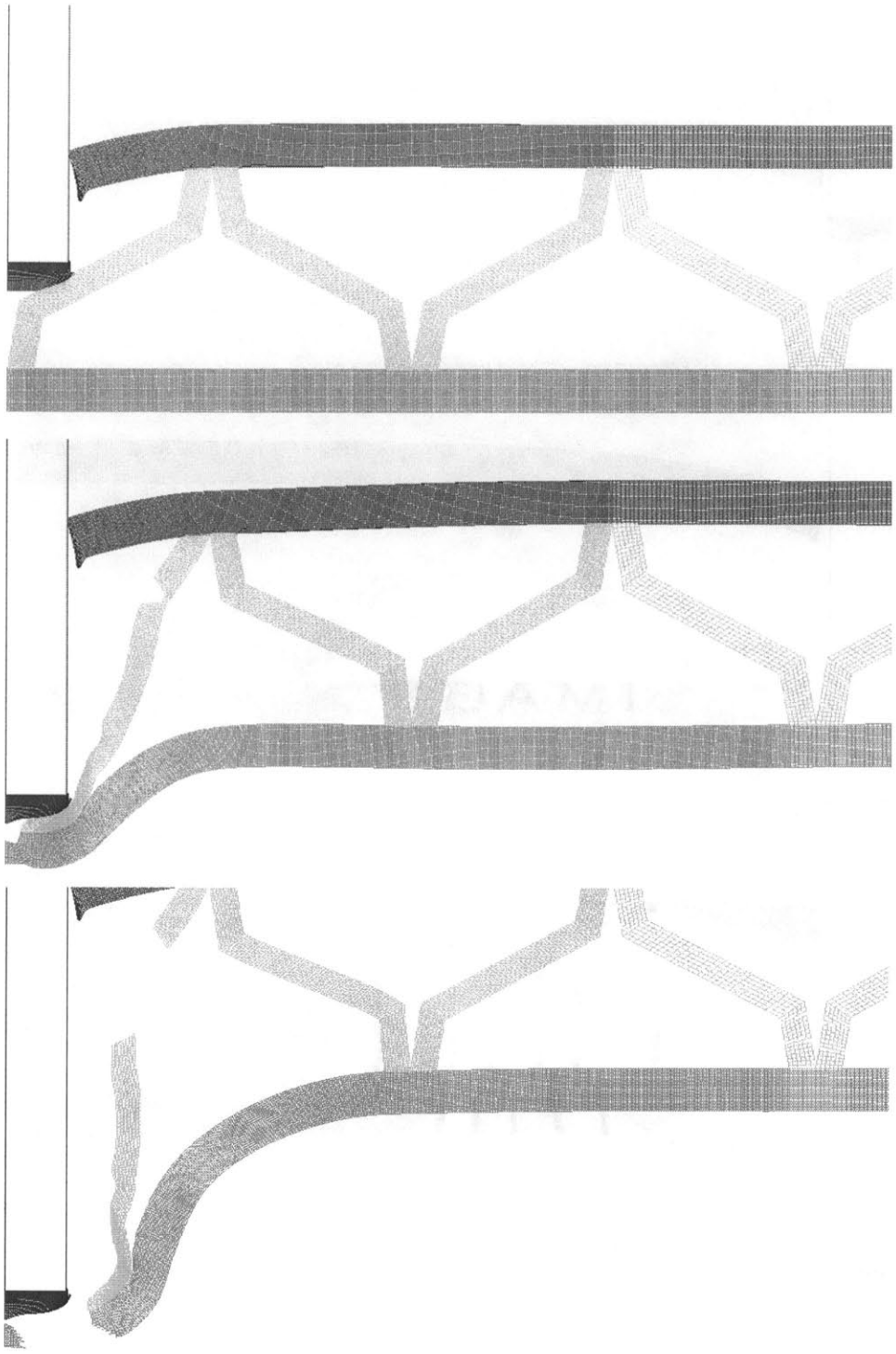

Fig. 5.17: The perforation process of the BRAS shield impacted normally by the light flat-nose projectile towards the bottom joint at $V_0 = 400$m/s.

The perforation process of the monolithic plate impacted normally by the light flat-nose projectile at $V_0 = 400$m/s is shown in Fig. 5.18. Apparently, the failure mode of the monolithic plate is shear plugging. Figure 5.19 shows the time history of the transient velocity of the light flat-nose projectile at $V_0 = 400$m/s for both configuration. It can be concluded that the BRAS shield is superior to the monolithic plate in perforation resistance against the light flat-nose projectile at $V_0 = 400$m/s.

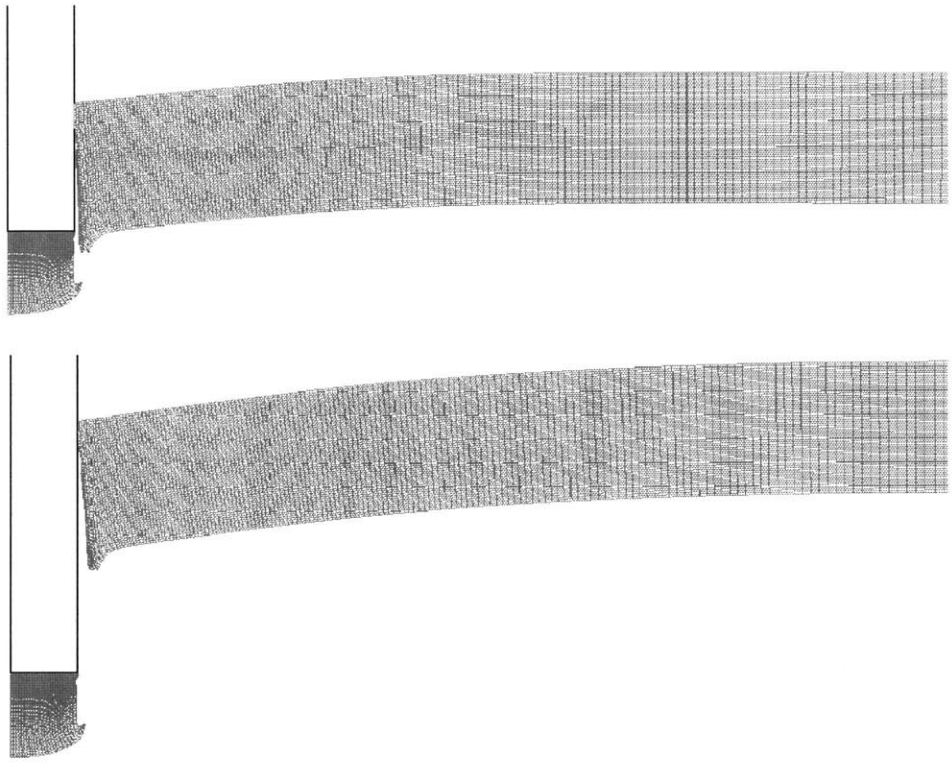

Fig. 5.18: The perforation process of the monolithic plate impacted normally by the light flat-nose projectile at $V_0 = 400$m/s.

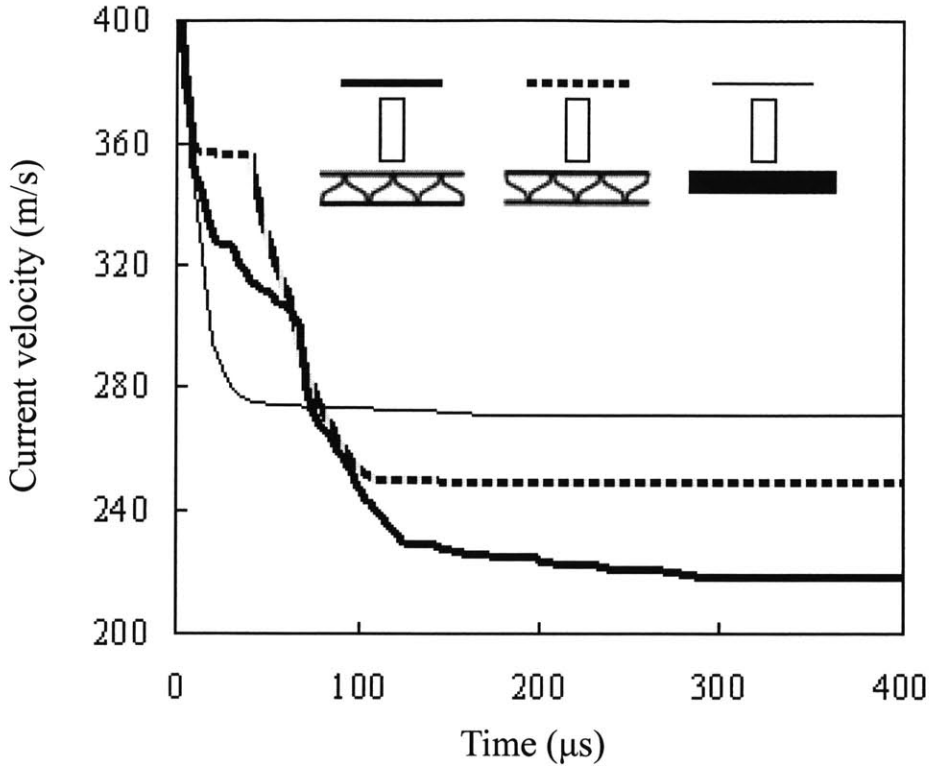

Fig. 5.19: Time history of the transient velocity of the light flat-nose projectile at V_0 = 400m/s

When the impact velocity is increased to 800m/s, the results are similar to the preceding section under the impacted of the heavy flat-nose projectile. It can be observed that both the BRAS shields and the monolithic plates mainly fail by shear plugging, Compared to the monolithic plate, the sandwich core of the BRAS shield contribute some additional energy through bending deformation and tensile tearing. Figure 5.20-5.22 show that the perforation processes of the BRAS shields and the monolithic plates impacted normally by the light flat-nose projectile at V_0 = 800m/s.

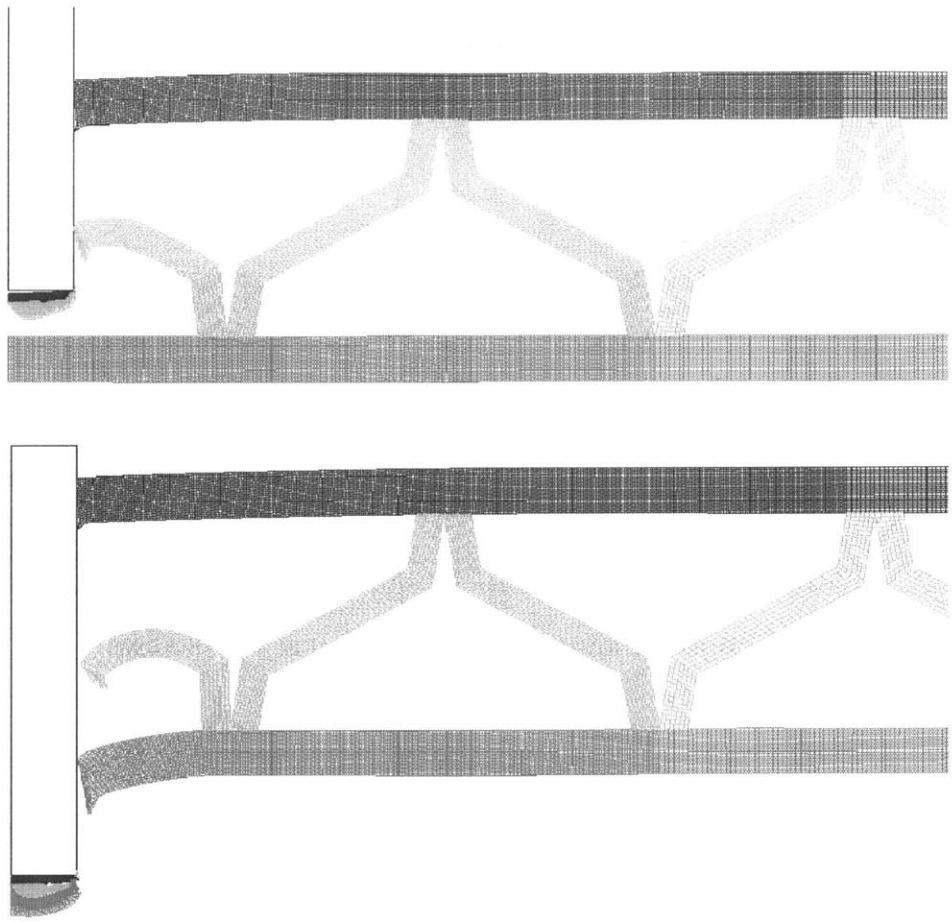

Fig. 5.20: The perforation process of the BRAS shield impacted normally by the light flat-nose projectile towards the top joint at V_0 = 800m/s.

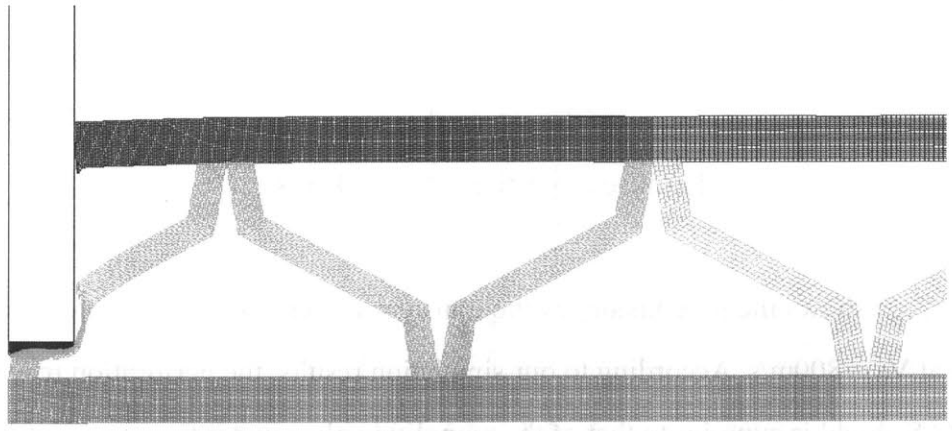

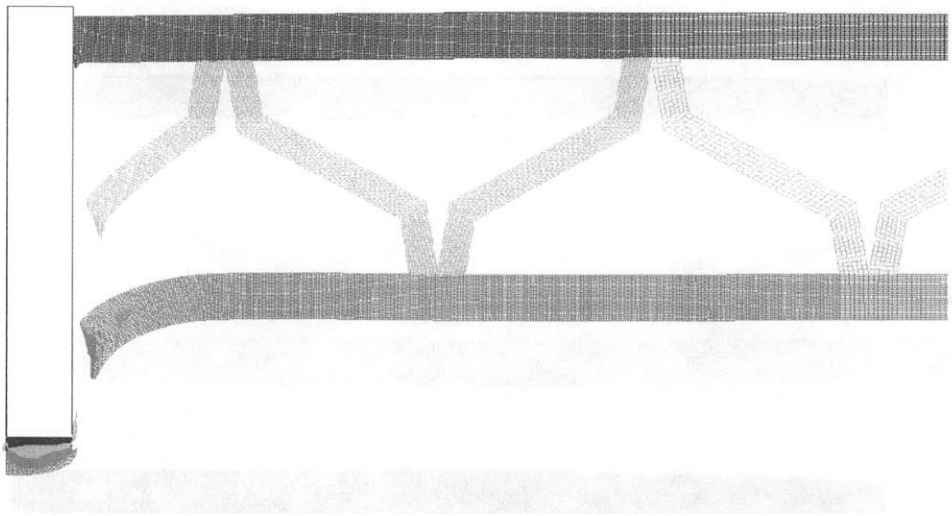

Fig. 5.21: The perforation process of the BRAS shield impacted normally by the light flat-nose projectile towards the bottom joint at V_0 = 800m/s.

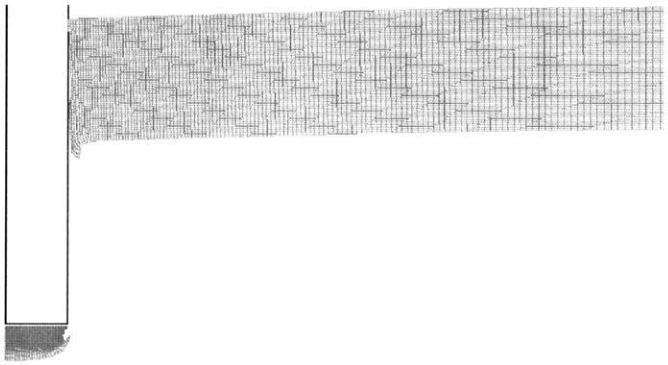

Fig. 5.22: The perforation process of the monolithic plate impacted normally by the light flat-nose projectile at V_0 = 800m/s.

Figure 5.23 shows the time history of the transient velocity of the light flat-nose projectile at V_0 = 800m/s. According to our simulation results, the perforation resistance of the BRAS shield is superior to that of the monolithic plate under the impact of the light flat-nose projectile at V_0 = 800m/s. This is in good accordance with our analysis.

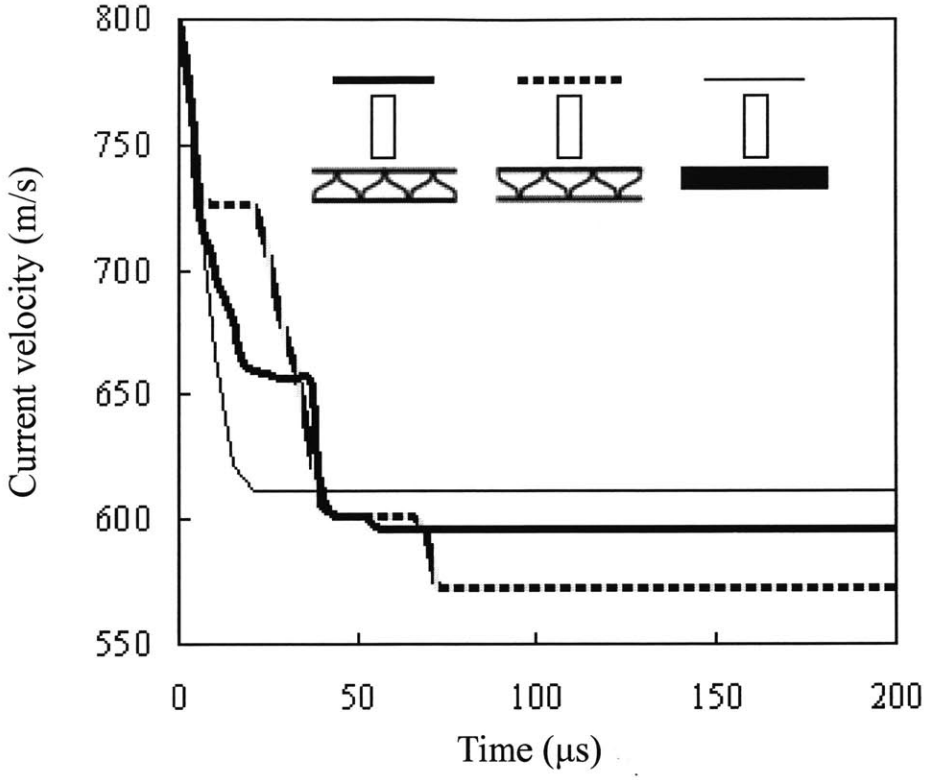

Fig. 5.23: Time history of the transient velocity of the light flat-nose projectile at V_0 = 800m/s

Based on section 5.1 and 5.3, it can be concluded that BRAS shield is superior to the monolithic plate in perforation resistance under the impact of flat-nose projectile.

5.4 Light-conical nose projectile

The projectile considered in this section is a conical-nose projectile of the mass M_0 = 30g and the diameter d = 12mm. The perforation processes of the monolithic and BRAS shields impacted normally by the light conical-nose projectile at V_0 = 400m/s is shown in Fig. 5.24-5.26. It can be observed that ductile hole enlargement is the failure mode for both configurations. As we have mentioned, empty inner structure is bad for transmission

of deformation, therefore, the BRAS shield is worse than the monolithic plate in perforation resistance against the light conical-nose projectile at V_0 = 400m/s, see Fig. 5.27.

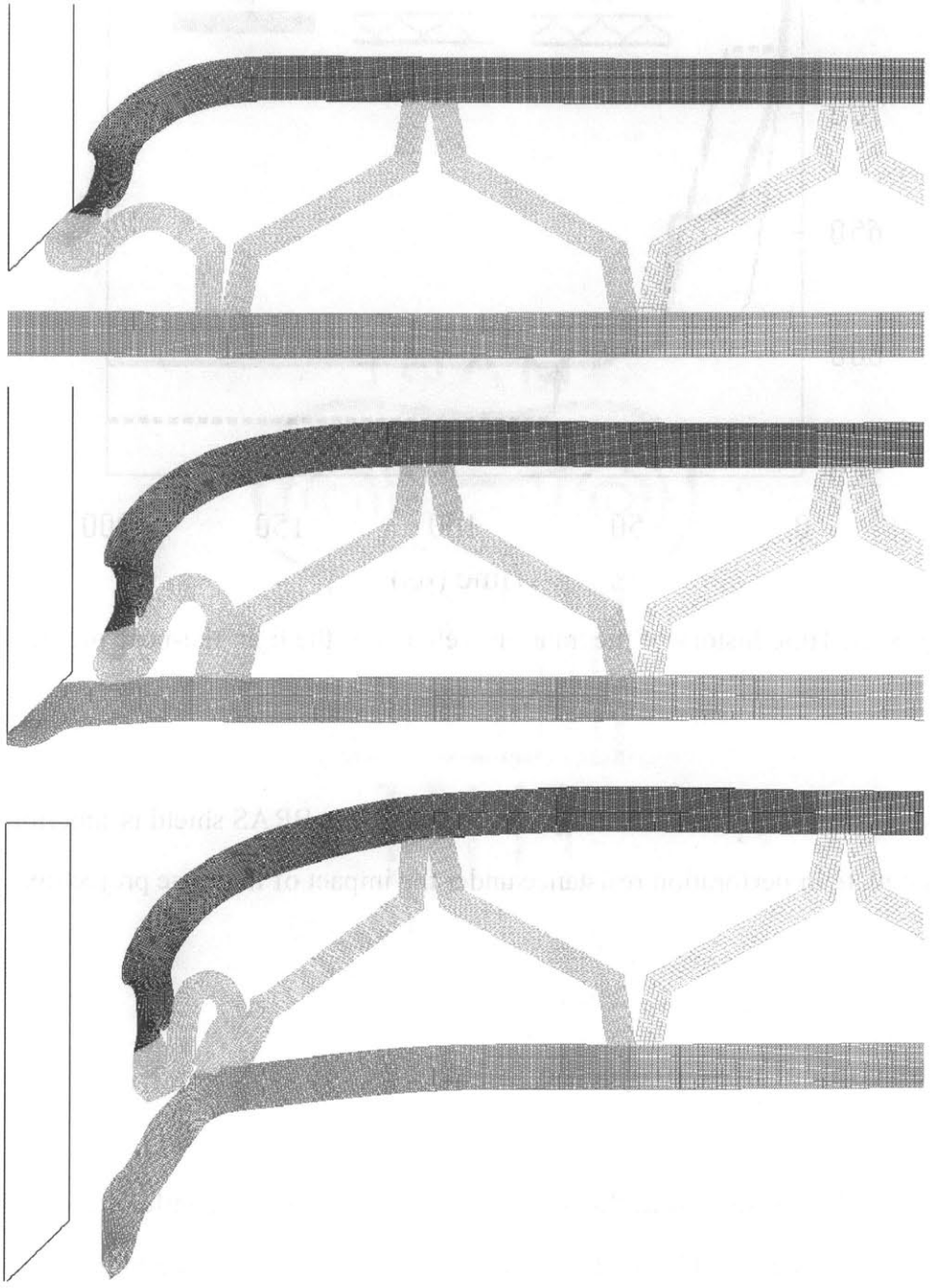

Fig. 5.24: The perforation process of the BRAS shield impacted normally by the light conical-nose projectile towards the top joint at V_0 = 400m/s.

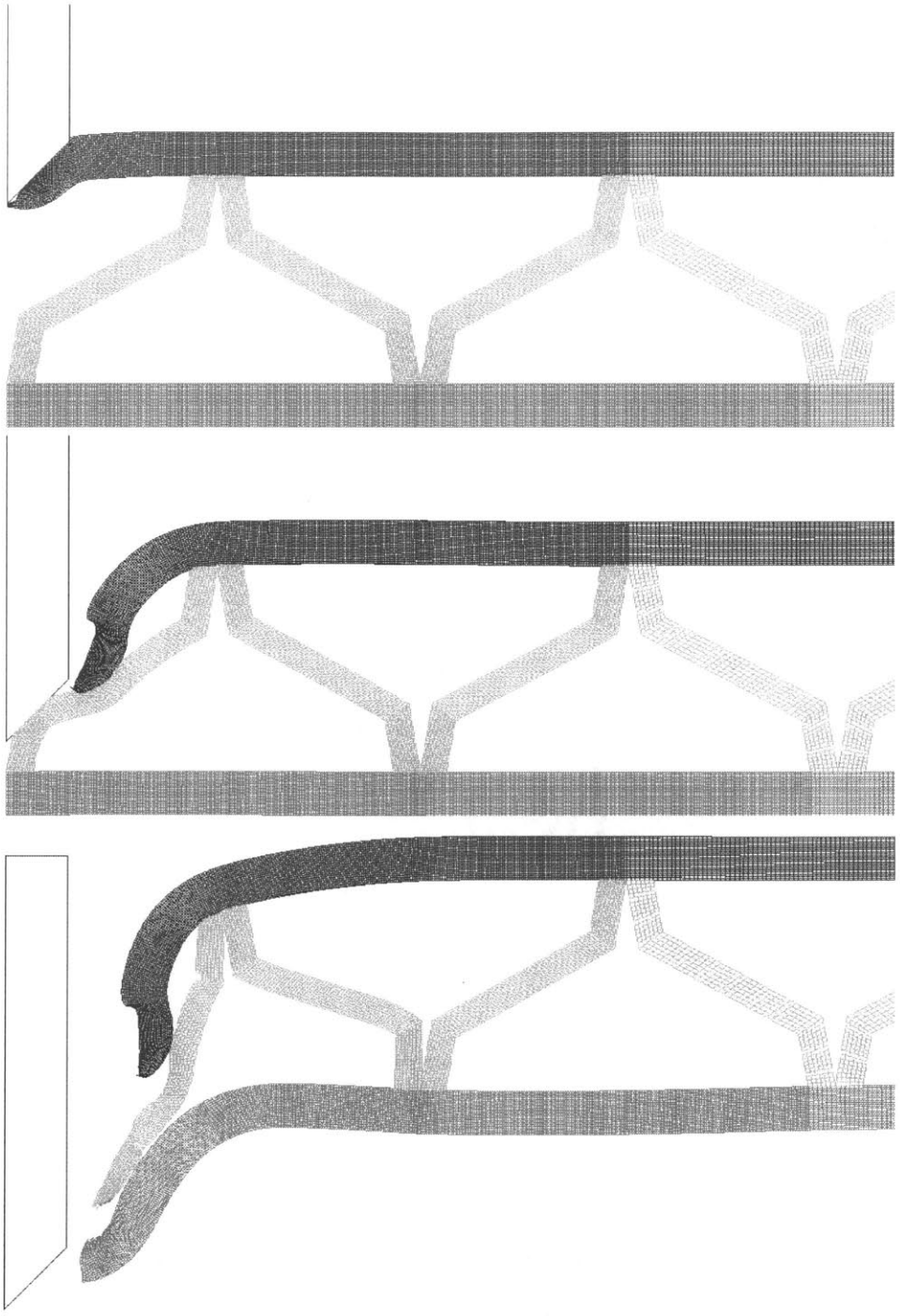

Fig. 5.25: The perforation process of the BRAS shield impacted normally by the light conical-nose projectile towards the bottom joint at V_0 = 400m/s.

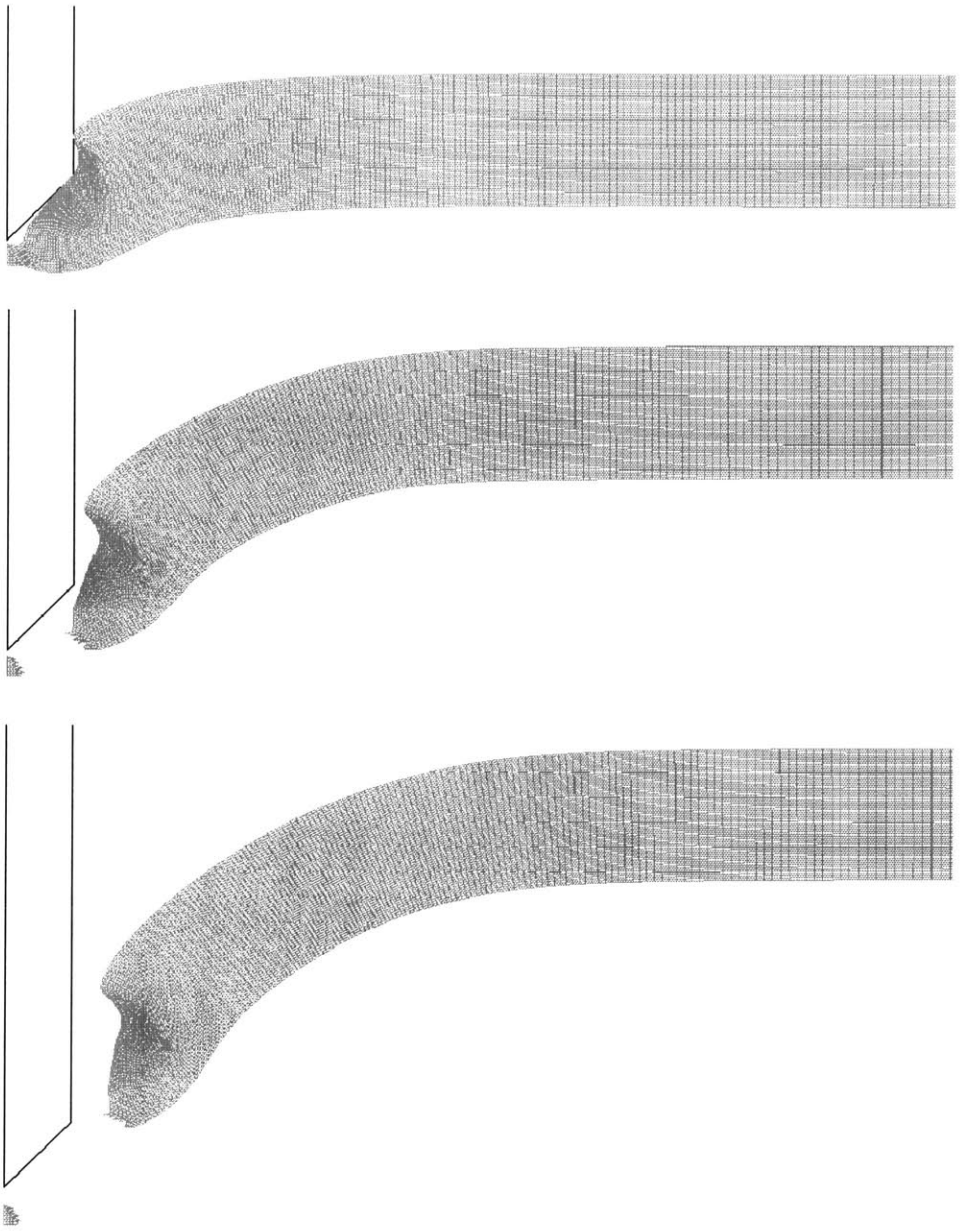

Fig. 5.26: The perforation process of the monolithic plate impacted normally by the light conical-nose projectile at $V_0 = 400$m/s.

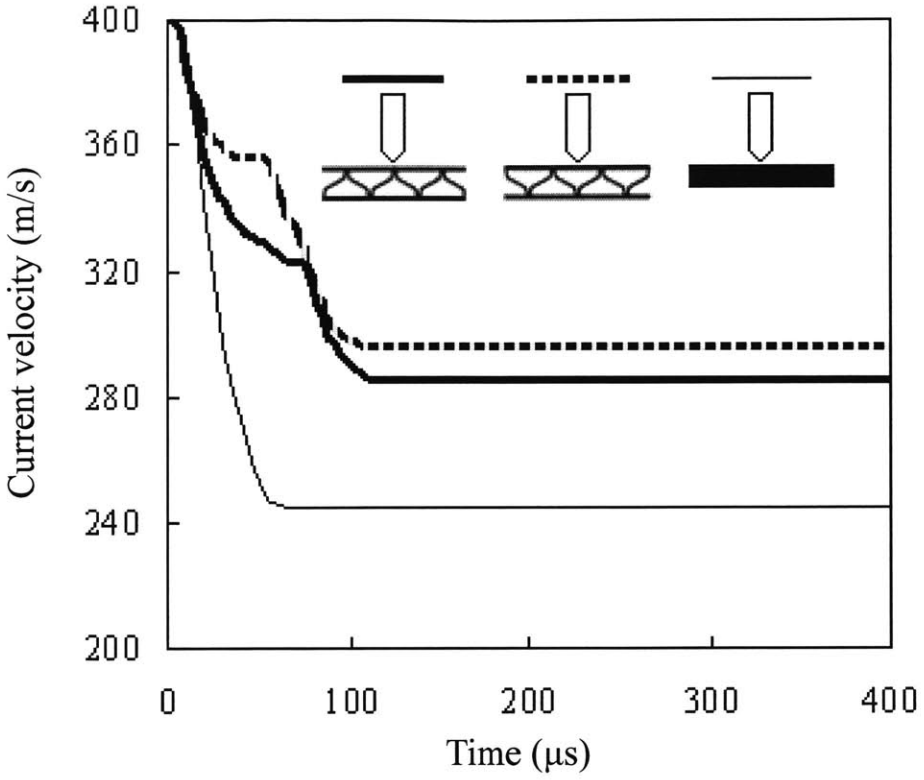

Fig. 5.27: Time history of the transient velocity of the light conical-nose projectile at V_0 = 400m/s

When the impact velocity is increased to 800m/s, the failure mode for both configurations becomes the same, that is ductile hole enlargement. Therefore, there is merely small difference between the perforation resistance of both shields. The perforation processes of the monolithic and BRAS shields impacted normally by the light conical-nose projectile at V_0 = 800m/s is shown in Fig. 5.28-5.30.

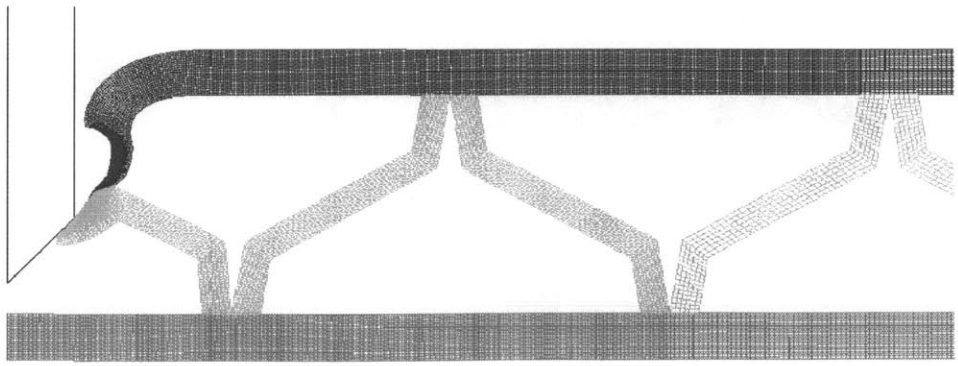

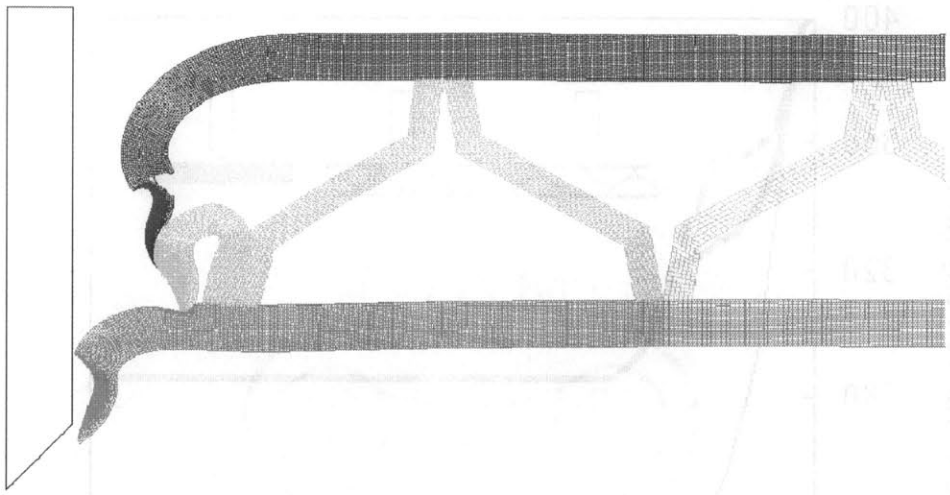

Fig. 5.28: The perforation process of the BRAS shield impacted normally by the light conical-nose projectile towards the top joint at V_0 = 800m/s.

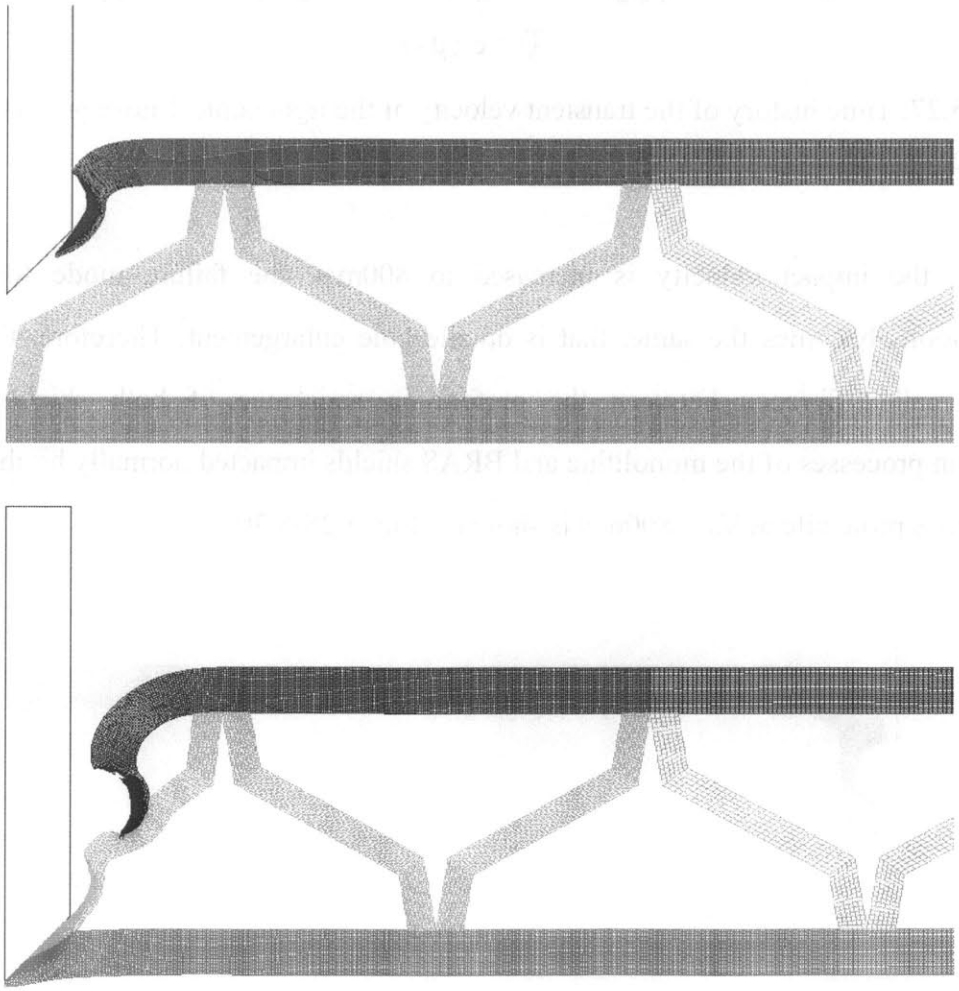

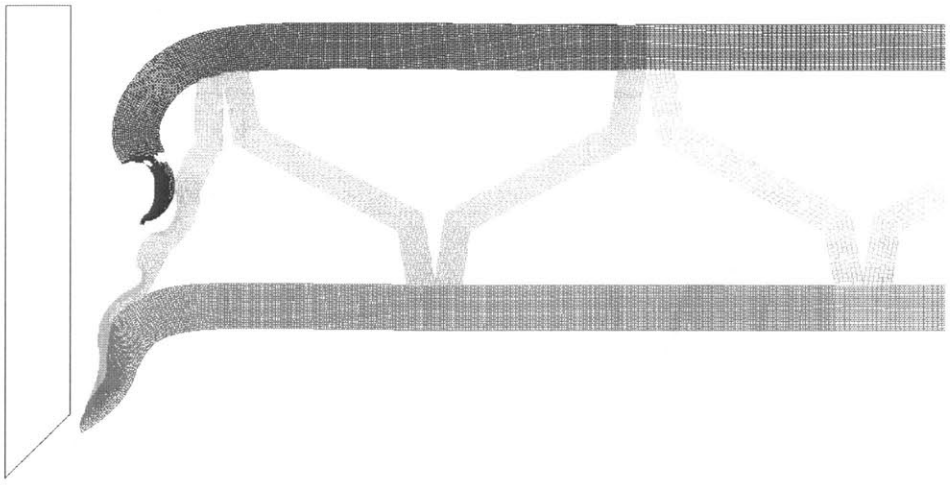

Fig. 5.29: The perforation process of the BRAS shield impacted normally by the light conical-nose projectile towards the bottom joint at V_0 = 800m/s.

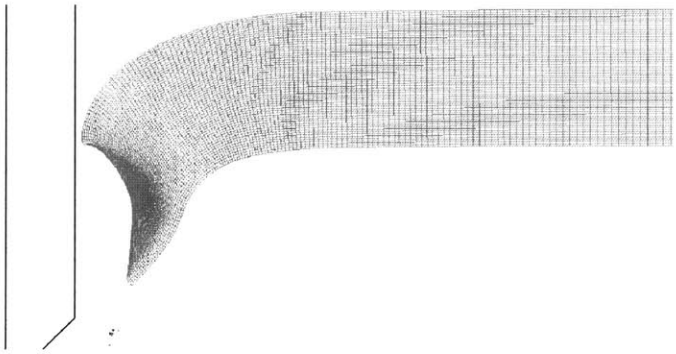

Fig. 5.30: The perforation process of the monolithic plate impacted normally by the light conical-nose projectile at V_0 = 800m/s.

Figure 5.31 shows the time history of the transient velocity of the light conical-nose projectile at V_0 = 800m/s for both configurations. The simulation results are in general in accordance with our analysis. Base on section 5.2 and 5.4, it can be concluded that the BRAS shield is worse than the monolithic plate in perforation resistance against conical-nose projectile at low velocity. However, at high impact velocity, the BRAS shield is not worse than the monolithic plate. Also, the impact position towards the bottom joint is more detrimental than that towards the top joint under the impact of conical-nose projectile.

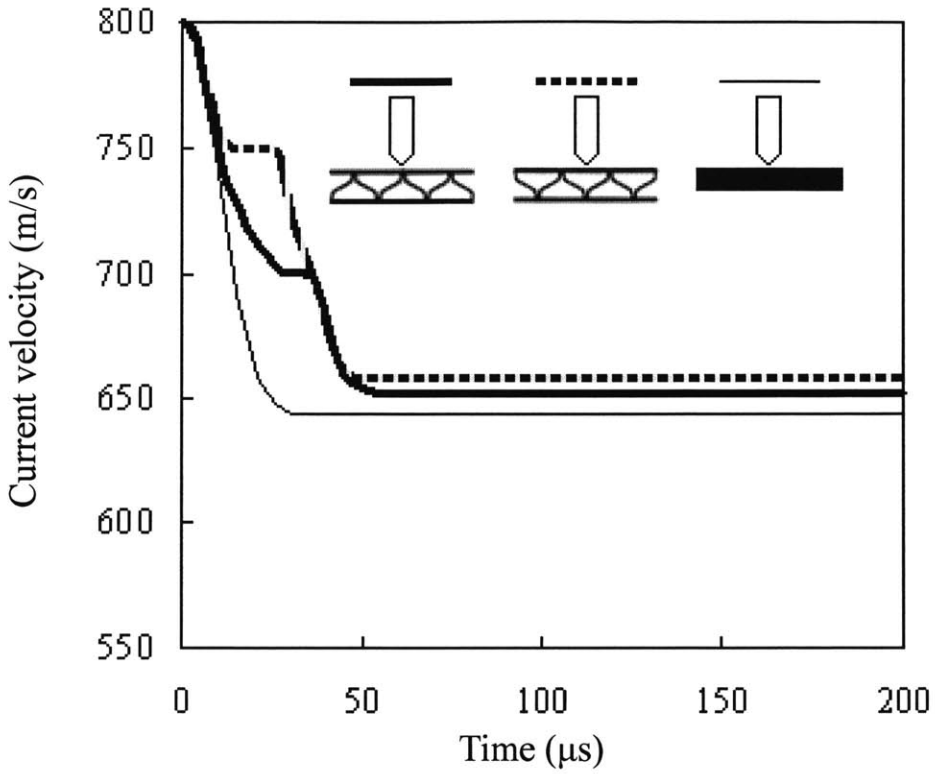

Fig. 5.31: Time history of the transient velocity of the light conical-nose projectile at $V_0 = 800$m/s

Chapter 6
Discussions and Conclusions

In this thesis, the ballistic resistance of the 12mm-thick monolithic plates, the double-layered shields and the BRAS shield of the same weight against projectile impact has been studied using the numerical method. Eight types of projectiles of different weight and nose shapes with a wide range of impact velocity were considered.

6.1 Double-layered shield

Compared to the monolithic plate, the double-layered shields are able to improve the ballistic limit by about 7.0% - 25.0% under the impact of the flat-nose projectiles. However, under the impact of the conical-nose projectile, the perforation resistance of the double-layered shield is slightly weaker than the monolithic plate. The numerical results are in accordance with the experimental results published in the open literature.

It was also found that it is not necessary to perfectly bond two layers to enhance the effectiveness of a double-layered shield. The double-layered shield is as effective as, or more effective than, a monolithic plate of the same weight. At the same time, it will be easy to repair as compared to a monolithic plate. Partially penetrated/damaged plates can be replaced without changing a whole shield.

Furthermore, the increase in the spacing between the two layers is not significantly improving the ballistic resistance of the double-layered shields. Actually, the gap decreases the ballistic limit under the impact of the conical-nose projectile.

An armor shield may encounter various projectile impact. It was revealed by experimental study that the heavy flat-nose projectile is the most detrimental one, the heavy conical-nose and the light flat-nose projectiles are the medium detrimental ones, while the light conical-nose projectile is the least detrimental one.

6.2 Double-layered shield with different material combinations

At low impact velocity, the double-layered shield with the upper layer of high ductility material and the lower layer of low ductility material is always the best configuration for perforation resistance among four configurations, while the double-layered shield with the upper layer of low ductility material and the lower layer of high ductility material is the worst one.

At high velocity impact by the heavy flat-nose projectile, which is the most detrimental projectile, four configurations are nearly the same in perforation resistance. At high velocity impact by the heavy conical-nose projectile and the light flat-nose projectile, which is the medium detrimental projectile, the perforation resistance is mainly depended on the ductility, while the effect of configuration is small. At high velocity impact by the light conical-nose projectile, which is the least detrimental projectile, the double-layered shield with the upper layer of high ductility material and the lower layer of low ductility material is superior than other four configurations in perforation resistance.

It can be concluded that, at moderate detrimental impact, the double-layered shield with the upper layer of high ductility material and the lower layer of low ductility material is the best configurations among all four configurations, while the

double-layered shield with the upper layer of low ductility material and the lower layer of high ductility material is the worst one.

6.3 BRAS shield

Under the impact of flat-nose projectile, the BRAS shield is superior to the monolithic plate in perforation resistance. Similar to the preceding section with double-layered shields with different material combinations, the perforation resistance of the BRAS shields against the heavy flat-nose projectile at high velocity impact is nearly the same for all configurations.

Under the impact of conical-nose projectile, the BRAS shield is worse than the monolithic plate in perforation resistance, except in the least detrimental case, that impacted by the light conical-nose projectile at high velocity. The impact position towards the bottom joint is more detrimental than that towards the top joint.

In this thesis, the upper and lower layers of the double-layered shields and the BRAS shield are assumed to be of the same thickness and the same material. It was indicated by limited studies that the perforation resistance of multi-layered shields can be further enhanced by placing a thinner plate in front of a thicker plate, e.g. see Corran et al. [2]. Also, the experiments conducted by Almohandes et al. [4] suggest that a double-layered shield consisting of two plates of uneven thickness is of a slightly higher ballistic limit than that of the same thickness. Meanwhile, for the BRAS shield, different grades of materials of various strength and ductility can also be defined for different layers. This is also a possible design for further increase of the ballistic limit. All those problems are the subject of an ongoing study.

Bibliography

[1] I. Marom and S. R. Bodner. Projectile perforation of multilayered beams. *International Journal of Mechanical Sciences*, 21(8):489 - 504, 1979.

[2] R. S. J. Corran, P. J. Shadbolt, and C. Ruiz. Impact loading of plates-an experimental investigation. *International Journal of Impact Engineering*, 1(1):3-22, 1983.

[3] J. Radin and W. Goldsmith. Normal projectile penetration and perforation of layered targets. *International Journal of Impact Engineering*, 7(2):229-259, 1988.

[4] A. A. Almohandes, M. S. Abdel-Kader, and A. M. Eleiche. Experimental investigation of the ballistic resistance of steel-fiberglass reinforced polyester laminated plates. *Composites Part B: Engineering*, 27(5):447-458, 1996.

[5] T. Børvik, S. Dey, and A. H. Clausen. A preliminary study on the perforation resistance of high-strength steel plates. *Journal de Physique IV*, 134:1053 - 1059, 2006.

[6] S. Dey, T. Børvik, X. Teng, T. Wierzbicki, and O. S. Hopperstad. On the ballistic resistance of double-layered steel plates: An experimental and numerical investigation. 2006. Int.

[7] G. Ben-Dor, A. Dubinsky, and T. Elperin. Effect of air gaps on the ballistic resistance of ductile shields perforated by nonconical impactors. *Journal of Mechanics of Materials and Structures*, 1:279-299, 2006.

[8] P. Elek, S. Jaramaz, and D. Mickovic. Modeling of perforation of plates and multi-layered metallic targets. *International Journal of Solids and Structures*, 42:1209-1224, 2005.

[9] J. Liss, W. Goldsmith, and J. M. Kelly. A phenomenological penetration model of plates. *International Journal of Impact Engineering*, 1(4):321-341, 1983.

[10] C. C. Liang, M. F. Yang, P. W. Wu, and T. L. Teng. Resistant performance of perforation of multi-layered targets using an estimation procedure with marine application. *Ocean Engineering*, 32(3-4):441-468, 2005.

[11] X. Teng and T. Wierzbicki. Failure mode transition in round-nosed mass-to-beam impact. *European Journal of Mechanics-A Solids*, 24(5):857-876, 2005.

[12] T. Børvik, M. Langseth, O. S. Hopperstad, and K. A. Malo. Perforation of 12mm thick steel plates by 20mm diameter projectiles with flat, hemispherical and conical noses Part I: Experimental study. *International Journal of Impact Engineering*, 27(1):19-35, 2002.

[13] T. Børvik, O. S. Hopperstad, T. Berstad, and M. Langseth. Perforation of 12mm thick steel plates by 20mm diameter projectiles with flat, hemispherical and conical noses Part II: Numerical simulations. *International Journal of Impact Engineering*, 27(1):37-64, 2002.

[14] Young-Woong Lee. Fracture Prediction in Metal Sheets. Doctor Thesis, MIT.

[15] Military Specification MIL-P-46593A (ORD). Projectile, calibers 0.22, 0.30, 0.50, and 20-mm fragment simulating, 1962.

[16] X. Teng and T. Wierzbicki. Numerical study on crack propagation in high velocity perforation. *Computers and Structures*, 83:989-1004, 2005.

[17] T. Børvik, O. S. Hopperstad, M. Langseth, and K. A. Malo. Effects of target thickness in blunt projectile penetration of Weldox 460 E steel plates. *International Journal of Impact Engineering*, 28(4):413-464, 2003.

[18] T. Børvik, O. S. Hopperstad, S. Dey, E. V. Pizzinato, M. Langseth, and C. Albertini. Strength and ductility of Weldox 460 E steel at high strain rates, elevated temperatures and various stress triaxialities. *Engineering Fracture Mechanics*, 72:1071-1087, 2005.

[19] T. Børvik, O. S. Hopperstad, T. Berstad, and M. L. Langseth. A computational model of viscoplasticity and ductile damage for impact and penetration. *European Journal of Mechanics: A/Solids*, 20:685-712, 2001.

[20] G. R. Johnson and W. H. Cook. A constitutive model and data for metals subjected to large strains, high strain rates and high temperatures. In *Proceedings of the Seventh International Symposium on Ballistics*, pages 541-547, Hague, Netherlands, 1983.

[21] G. R. Johnson and W. H. Cook. Fracture characteristics of three metals subjected to various strains, strain rates, temperatures and pressures. *Engineering Fracture Mechanics*, 21(1):31 - 48, 1985.

[22] Y. Bao and T. Wierzbicki. On the cut-off value of negative triaxiality for fracture. *Engineering Fracture Mechanics*, 72(7):1049 - 1069, 2005.

[23] X. Teng, T. Wierzbicki, S. Hiermaier, and I. Rohr. Numerical prediction of the Taylor test with fracture. *International Journal of Solids and Structures*, 42(9/10):2929-2948, 2005.

[24] S. Dey, T. Børvik, O. S. Hopperstada, J. R. Leinumc, and M. Langseth. The effect of target strength on the perforation of steel plates using three different projectile nose shapes. *International Journal of Impact Engineering*, 30:1005-1038, 2004.

[25] N. K. Gupta and V. Madhu. An experimental study of normal and oblique impact of hard-core projectile on single and layered plates. *International Journal of Impact Engineering*, 19:395 - 414, 1997.

Appendices

The input files used to simulate the perforation of the multi-layered shields against projectile impact using Abaqus/Explicit

The double-layered shield:

```
*Heading
** Job name: double-layered-joint-shield Model name: double-layered-joint-shield
*Preprint, echo=NO, model=NO, history=NO, contact=NO
**
** PARTS
**
*Part, name=shield
*End Part
*Part, name=projectile
*End Part
**
** ASSEMBLY
**
```

```
*Assembly, name=Assembly
**
*Instance, name=shield, part=shield
*Node
      1,          0.25,           0.006
      2,            0.,           0.006
      3,            0.,              0.
      4,          0.25,              0.
      5,          0.25,           0.012
      6,            0.,           0.012
...
18361,     0.2478709,          0.0118
*Element, type=CAX4R
      1,      1,      7,   1020,    662
      2,      7,      8,   1021,   1020
      3,      8,      9,   1022,   1021
      4,      9,     10,   1023,   1022
      5,     10,     11,   1024,   1023
...
18000, 18361,    691,      5,    692
*Elset, elset=set-1, generate
 9001,   18000,         1
*Elset, elset=Set-2, generate
      1,   9000,         1
** Region: (Section-1:Set-1)
** Section: Section-1
*Solid Section, elset=Set-1, material=high_ductility
```

```
1.,
** Region: (Section-2:Set-2)
** Section: Section-2
*Solid Section, elset=Set-2, material=low_ductility
1.,
*End Instance
**
*Instance, name=projectile, part=projectile
          0.,          0.013,          0.
** Region: (point:Picked)
*Element, type=MASS, elset=projectile_MASS_
1, 1
*Mass, elset=projectile_MASS_
0.03,
*Node
       1,          0.,          0.,          0.
*Nset, nset=projectile_RefPt_, internal
1,
*Surface, type=SEGMENTS, name=projectile_RigidSurface_, internal
START, 0.,          0.
 LINE,  0.,        0.044
 LINE,  0.006, 0.044
 LINE,  0.006, 0.006
 LINE,  0.,          0.
*Rigid Body, ref node=projectile_RefPt_, analytical surface=projectile_RigidSurface_
*End Instance
*Nset, nset=projectile_initial_velocity, internal, instance=bullet-1
```

1,

*Nset, nset=projectile_bc, internal, instance=bullet-1

1,

*Nset, nset=projectile_current_velocity, instance=bullet-1

1,

*Nset, nset=shield_temperature, internal, instance=shield, generate

1, 18361, 1

*Elset, elset=shield_temperature, internal, instance=shield, generate

1, 18000, 1

*Nset, nset=shield_bc1, internal, instance=shield

1, 4, 5, 634, 635, 636, 637, 638, 639, 640, 641, 642, 643, 644, 645, 646, 647, 648, 649, 650, 651, 652, 653, 654, 655, 656, 657, 658, 659, 660, 661, 662, 663, 664, 665, 666, 667, 668, 669, 670, 671, 672, 673, 674, 675, 676, 677, 678, 679, 680, 681, 682, 683, 684, 685, 686, 687, 688, 689, 690, 691

*Elset, elset=shield_bc1, internal, instance=shield

1, 301, 601, 901, 1201, 1501, 1801, 2101, 2401, 2701, 3001, 3301, 3601, 3901, 4201, 4501, 4801, 5101, 5401, 5701, 6001, 6301, 6601, 6901, 7201, 7501, 7801, 8101, 8401, 8701, 9300, 9600, 9900, 10200, 10500, 10800, 11100, 11400, 11700, 12000, 12300, 12600, 12900, 13200, 13500, 13800, 14100, 14400, 14700, 15000, 15300, 15600, 15900, 16200, 16500, 16800, 17100, 17400, 17700, 18000

*Nset, nset=shield_bc2, internal, instance=shield

2, 3, 6, 306, 307, 308, 309, 310, 311, 312, 313, 314, 315, 316, 317, 318, 319, 320, 321, 322, 323, 324, 325, 326, 327, 328, 329, 330, 331, 332, 333, 334, 991, 992, 993, 994, 995, 996, 997, 998, 999, 1000, 1001, 1002, 1003, 1004, 1005, 1006, 1007, 1008, 1009, 1010, 1011, 1012, 1013, 1014, 1015, 1016, 1017, 1018, 1019

*Elset, elset=shield_bc2, internal, instance=shield

```
 300,   600,   900,  1200,  1500,  1800,  2100,  2400,  2700,  3000,  3300,  3600,
3900,  4200,  4500,  4800,  5100,  5400,  5700,  6000,  6300,  6600,  6900,  7200,
7500,  7800,  8100,  8400,  8700,  9000,  9001,  9301,  9601,  9901, 10201, 10501,
10801, 11101, 11401, 11701, 12001, 12301, 12601, 12901, 13201, 13501, 13801, 14101,
14401, 14701, 15001, 15301, 15601, 15901, 16201, 16501, 16801, 17101, 17401, 17701
*Nset, nset=shield, instance=shield, generate
      1,  18361,        1
*Elset, elset=shield, instance=shield, generate
      1,  18000,        1
*Nset, nset=shield_output, instance=shield
      2, 256, 277, 363, 962
*Nset, nset=shield_CNS_, internal, instance=shield, generate
      1,  18361,        1
*Surface, type=NODE, name=shield_CNS_, internal
shield, 1.
*End Assembly
**
** MATERIALS
**
*Material, name=high_ductility
*Density
7850.,
*Elastic
 2e+11, 0.33
*Inelastic Heat Fraction
          0.9,
*Plastic
```

4.9e+08, 0., 293.

6.7564e+08, 0.2, 293.

7.4359e+08, 0.4, 293.

7.9435e+08, 0.6, 293.

8.3641e+08, 0.8, 293.

8.73e+08, 1., 293.

9.0575e+08, 1.2, 293.

9.3561e+08, 1.4, 293.

9.6321e+08, 1.6, 293.

9.8897e+08, 1.8, 293.

1.0132e+09, 2., 293.

1.0361e+09, 2.2, 293.

1.0579e+09, 2.4, 293.

1.0788e+09, 2.6, 293.

1.0987e+09, 2.8, 293.

1.1179e+09, 3., 293.

1.1364e+09, 3.2, 293.

1.1543e+09, 3.4, 293.

1.1716e+09, 3.6, 293.

1.1884e+09, 3.8, 293.

1.2047e+09, 4., 293.

1.2206e+09, 4.2, 293.

1.236e+09, 4.4, 293.

1.2511e+09, 4.6, 293.

1.2658e+09, 4.8, 293.

1.2802e+09, 5., 293.

4.4923e+08, 0., 400.

```
 6.1941e+08,  0.2, 400.
 6.8171e+08,  0.4, 400.
 7.2825e+08,  0.6, 400.
 7.6681e+08,  0.8, 400.
 8.0035e+08,   1., 400.
 8.3038e+08,  1.2, 400.
 8.5776e+08,  1.4, 400.
 8.8306e+08,  1.6, 400.
 9.0667e+08,  1.8, 400.
 9.2888e+08,   2., 400.
...
 7.5297e+07,   4.,1700.
 7.6289e+07,  4.2,1700.
 7.7255e+07,  4.4,1700.
 7.8197e+07,  4.6,1700.
 7.9117e+07,  4.8,1700.
 8.0016e+07,   5.,1700.
*Rate Dependent, type=YIELD RATIO
      1.,     0.
 1.1493,  100.
 1.1584,  200.
 1.1638,  300.
 1.1676,  400.
 1.1706,  500.
...
 1.2362,60000.
*Shear failure, type=tabular
```

0.8410, , -1.5000

0.8837, , -1.4000

0.9289, , -1.3000

0.9765, , -1.2000

1.0268, , -1.1000

1.0798, , -1.0000

1.1358, , -0.9000

1.1949, , -0.8000

1.2573, , -0.7000

1.3232, , -0.6000

1.3927, , -0.5000

1.4660, , -0.4000

1.5435, , -0.3000

1.6252, , -0.2000

1.7115, , -0.1000

1.8025, , 0

1.8986, , 0.1000

2.0000, , 0.2000

2.1071, , 0.3000

4.0000, , 0.3300

*Specific Heat

452.,

*Material, name=low_ductility

*Density

7850.,

*Elastic

2e+11, 0.33

*Inelastic Heat Fraction

0.9,

*Plastic

9.8e+08, 0., 293.

1.35128e+09, 0.2, 293.

1.48718e+09, 0.4, 293.

1.5887e+09, 0.6, 293.

1.67282e+09, 0.8, 293.

1.746e+09, 1., 293.

1.8115e+09, 1.2, 293.

1.87122e+09, 1.4, 293.

1.92642e+09, 1.6, 293.

1.97794e+09, 1.8, 293.

2.0264e+09, 2., 293.

2.0722e+09, 2.2, 293.

2.1158e+09, 2.4, 293.

2.1576e+09, 2.6, 293.

2.1974e+09, 2.8, 293.

2.2358e+09, 3., 293.

2.2728e+09, 3.2, 293.

2.3086e+09, 3.4, 293.

2.3432e+09, 3.6, 293.

2.3768e+09, 3.8, 293.

2.4094e+09, 4., 293.

2.4412e+09, 4.2, 293.

2.472e+09, 4.4, 293.

2.5022e+09, 4.6, 293.

2.5316e+09, 4.8, 293.

2.5604e+09, 5., 293.

8.9846e+08, 0., 400.

1.23882e+09, 0.2, 400.

1.36342e+09, 0.4, 400.

1.4565e+09, 0.6, 400.

1.53362e+09, 0.8, 400.

1.6007e+09, 1., 400.

1.66076e+09, 1.2, 400.

1.71552e+09, 1.4, 400.

1.76612e+09, 1.6, 400.

1.81334e+09, 1.8, 400.

1.85776e+09, 2., 400.

...

1.50594e+08, 4.,1700.

1.52578e+08, 4.2,1700.

1.5451e+08, 4.4,1700.

1.56394e+08, 4.6,1700.

1.58234e+08, 4.8,1700.

1.60032e+08, 5.,1700.

*Rate Dependent, type=YIELD RATIO

1., 0.

1.1493, 100.

1.1584, 200.

1.1638, 300.

1.1676, 400.

1.1706, 500.

...

1.2362,60000.

*Shear failure, type=tabular

0.4205, , -1.5000

0.44185, , -1.4000

0.46445, , -1.3000

0.48825, , -1.2000

0.5134, , -1.1000

0.5399, , -1.0000

0.5679, , -0.9000

0.59745, , -0.8000

0.62865, , -0.7000

0.6616, , -0.6000

0.69635, , -0.5000

0.733, , -0.4000

0.77175, , -0.3000

0.8126, , -0.2000

0.85575, , -0.1000

0.90125, , 0

0.9493, , 0.1000

1.0000, , 0.2000

1.05355, , 0.3000

2.0000, , 0.3300

*Specific Heat

452.,

**

** INTERACTION PROPERTIES

```
**
*Surface Interaction, name=INTPROP-1
*Friction
 0.1,
*Surface Behavior, pressure-overclosure=HARD
**
** BOUNDARY CONDITIONS
**
** Name: BC-1 Type: Displacement/Rotation
*Boundary
projectile_bc, 1, 1
projectile_bc, 6, 6
** Name: BC-2 Type: Displacement/Rotation
*Boundary
shield_bc1, 1, 1
shield_bc1, 2, 2
shield_bc1, 6, 6
** Name: BC-3 Type: Displacement/Rotation
*Boundary
shield_bc2, 1, 1
shield_bc2, 6, 6
**
** FIELDS
**
** Name: Field-1     Type: Temperature
*Initial Conditions, type=TEMPERATURE
shield_temperature, 293.
```

```
** Name: Field-2    Type: Velocity
*Initial Conditions, type=VELOCITY
projectile_initial_velocity, 1, 0.
projectile_initial_velocity, 2, -400.
**
** STEP: Step-1
**
*Step, name=Step-1
*Dynamic, Explicit, adiabatic
, 0.0003
*Bulk Viscosity
0.06, 1.2
**
** INTERACTIONS
**
** Interaction: Int-1
*Contact Pair, interaction=INTPROP-1, mechanical constraint=KINEMATIC,
cpset=Int-1
shield_CNS_, projectile_RigidSurface_
**
** OUTPUT REQUESTS
**
*Restart, write, number interval=1, time marks=NO
**
** FIELD OUTPUT: F-Output-1
**
*Output, field
```

```
*Node Output
A, RF, U, V
**
** FIELD OUTPUT: F-Output-2
**
*Contact Output
CSTRESS,
**
** FIELD OUTPUT: F-Output-3
**
*Element Output
DENSITY, FV, LE, PE, PEEQ, S, SDV, STATUS, TEMP, UVARM
**
** HISTORY OUTPUT: H-Output-1
**
*Output, history
*Node Output, nset=shield_output
U1, U2, V1, V2
**
** HISTORY OUTPUT: H-Output-2
**
*Energy Output, elset=shield
ALLAE, ALLFD, ALLKE, ALLPD
**
** HISTORY OUTPUT: H-Output-3
**
*Node Output, nset=_projectile_current_velocity
```

V1, V2

*End Step

The BRAS shield:

*Heading

** Job name: BRAS_shield Model name: BRAS_shield

*Preprint, echo=NO, model=NO, history=NO, contact=NO

**

** PARTS

**

*Part, name=shield

*End Part

*Part, name=projectile

*End Part

**

** ASSEMBLY

**

*Assembly, name=Assembly

**

*Instance, name=shield, part=shield

*Node

1, 0.0388399996, -0.00667000003

2, 0.0365200005, -0.0050499998

3, 0.0211599991, -0.0133300005

4, 0.0234699994, -0.0149499997

5, 0.0425999984, 0.

6, 0.0399999991, 0.

```
 7, 0.0411599986, -0.00667000003
 8, 0.043469999, -0.0050499998
 9, 0.0373999998,              0.
10, 0.0026000001,              0.
11,              0.,            0.
12, 0.00115999999, -0.00667000003
13, 0.00347000011, -0.0050499998
14, 0.0174000002, -0.0199999996
15, 0.0199999996, -0.0199999996
16,         0.01884, -0.0133300005
17, 0.0165199991, -0.0149499997
18, 0.0226000007, -0.0199999996
...
 33104,   0.182505608, -0.0133210002
*Element, type=CPS4R
  1,     1,   129, 4257,   270
  2,   129,   130, 4258, 4257
  3,   130,   131, 4259, 4258
  4,   131,   132, 4260, 4259
  5,   132,   133, 4261, 4260
  6,   133,   134, 4262, 4261
  7,   134,   135, 4263, 4262
  8,   135,   136, 4264, 4263
  9,   136,   137, 4265, 4264
 10,   137,   138, 4266, 4265
...
31270, 33104,   4237,    126,   3818
```

```
*Elset, elset=Set-1, generate
     1,  31270, 1.
** Region: (Section-1:Set-1)
** Section: Section-1
*Solid Section, elset=Set-1, material=Weldox
1.,
*End Instance
**
*Instance, name=projectile, part=projectile
              0.,          0.005,              0.
** Region: (point:Picked)
*Element, type=MASS, elset=projectile_MASS_
1, 1
*Mass, elset=projectile_MASS_
0.2,
*Node
        1,              0.,              0.,              0.
*Nset, nset=projectile_RefPt_, internal
1,
*Surface, type=SEGMENTS, name=projectile_RigidSurface_, internal
START, 0.,          0.
 LINE,  0.,      0.044
 LINE,  0.006, 0.044
 LINE,  0.006, 0.006
 LINE,  0.,          0.
*Rigid Body, ref node=projectile_RefPt_, analytical surface=projectile_RigidSurface_
*End Instance
```

*Nset, nset=projectile_initial_velocity, internal, instance=projectile

1,

*Nset, nset=projectile_bc, internal, instance=projectile

1,

*Nset, nset=projectile_output, instance=projectile

1,

*Nset, nset=shield_temperature, internal, instance=shield, generate

1, 33104, 1

*Elset, elset=shield_temperature, internal, instance=shield, generate

1, 31270, 1

*Nset, nset=shield_bc1, internal, instance=shield

116, 117, 123, 124, 3612, 3613, 3614, 3615, 3616, 3617, 3618, 3619, 3620, 3621, 3622, 3623, 3624, 3625, 3626, 3627, 3628, 3629, 3630, 3631, 3784, 3785, 3786, 3787, 3788, 3789, 3790, 3791, 3792, 3793, 3794, 3795, 3796, 3797, 3798, 3799, 3800, 3801, 3802, 3803

*Elset, elset=shield_bc1, internal, instance=shield

27888, 27889, 27890, 27891, 27892, 27893, 27894, 27895, 27896, 27897, 27898, 27899, 27900, 27901, 27902, 27903, 27904, 27905, 27906, 27907, 27908, 29130, 29134, 29138, 29142, 29146, 29150, 29154, 29158, 29162, 29166, 29170, 29174, 29178, 29182, 29186, 29190, 29194, 29198, 29202, 29206, 29210

*Nset, nset=shield, instance=shield, generate

1, 33104, 1

*Elset, elset=shield, instance=shield, generate

1, 31270, 1

*Nset, nset=shield_bc2, internal, instance=shield

11, 40, 49, 53, 1279, 1280, 1281, 1282, 1283, 1284, 1285, 1286, 1287, 1288, 1289, 1290, 1291, 1292, 1293, 1294, 1295, 1296, 1297, 1298, 1901, 1902, 1903, 1904,

1905, 1906, 1907, 1908, 1909, 1910, 1911, 1912, 1913, 1914, 1915, 1916, 1917, 1918,
1919, 1920, 1921
*Elset, elset=shield_bc2, internal, instance=shield
11600, 11601, 11602, 11603, 11604, 11605, 11606, 11607, 11608, 11609, 11610, 11611,
11612, 11613, 11614, 11615, 11616, 11617, 11618, 11619, 11620, 17913, 17914, 17915,
17916, 17917, 17918, 17919, 17920, 17921, 17922, 17923, 17924, 17925, 17926, 17927,
17928, 17929, 17930, 17931, 17932, 17933, 17934
*Nset, nset=shield_output, instance=shield
2, 3
*Nset, nset=shield_CNS_, internal, instance=shield, generate
1, 33104, 1
*Elset, elset=shield_contact_1a_S2, internal, instance=shield
1963, 1976, 1989, 2002, 2015, 2028, 2041, 2054, 2067, 2080, 2093, 2106,
2119, 2132, 2145, 2158, 2171, 2184, 2197, 2210, 2223, 2236, 2249, 2262,
2275, 2288, 2301, 2314, 2327, 2340, 29303, 29316, 29329, 29342, 29355, 29368,
29381, 29394, 29407, 29420, 29433, 29446, 29459
*Surface, type=ELEMENT, name=shield_contact_1a, internal
shield_contact_1a_S2, S2
*Elset, elset=shield_contact_1b_S2, internal, instance=shield, generate
637, 780, 13
*Elset, elset=shield_contact_1b_S4, internal, instance=shield, generate
2341, 2718, 13
*Surface, type=ELEMENT, name=shield_contact_1b, internal
shield_contact_1b_S2, S2
shield_contact_1b_S4, S4
*Elset, elset=shield_contact_2a_S4, internal, instance=shield, generate
9626, 11327, 21

*Surface, type=ELEMENT, name=shield_contact_2a, internal
shield_contact_2a_S4, S4
*Elset, elset=shield_contact_2b_S2, internal, instance=shield, generate
 29303, 29784,   13
*Surface, type=ELEMENT, name=shield_contact_2b, internal
shield_contact_2b_S2, S2
*Elset, elset=shield_contact_3a_S2, internal, instance=shield, generate
 2353, 2483,   13
*Surface, type=ELEMENT, name=shield_contact_3a, internal
shield_contact_3a_S2, S2
*Elset, elset=shield_contact_3b_S2, internal, instance=shield, generate
 15228, 15448,   22
*Surface, type=ELEMENT, name=shield_contact_3b, internal
shield_contact_3b_S2, S2
*Elset, elset=shield_contact_4a_S4, internal, instance=shield, generate
 1561, 1938,   13
*Surface, type=ELEMENT, name=shield_contact_4a, internal
shield_contact_4a_S4, S4
*Elset, elset=shield_contact_4b_S2, internal, instance=shield, generate
 29797, 30070,   13
*Surface, type=ELEMENT, name=shield_contact_4b, internal
shield_contact_4b_S2, S2
*Elset, elset=shield_contact_5a_S4, internal, instance=shield, generate
 29291, 30058,   13
*Surface, type=ELEMENT, name=shield_contact_5a, internal
shield_contact_5a_S4, S4
*Elset, elset=shield_contact_5b_S4, internal, instance=shield, generate

```
 1964,  2328,     13
*Surface, type=ELEMENT, name=shield_contact_5b, internal
shield_contact_5b_S4, S4
*Elset, elset=shield_contact_6a_S4, internal, instance=shield, generate
 29577,  30058,      13
*Surface, type=ELEMENT, name=shield_contact_6a, internal
shield_contact_6a_S4, S4
*Elset, elset=shield_contact_6b_S2, internal, instance=shield, generate
 16042,  17406,      22
*Surface, type=ELEMENT, name=shield_contact_6b, internal
shield_contact_6b_S2, S2
*Surface, type=NODE, name=shield_CNS_, internal
shield, 1.
*End Assembly
**
** MATERIALS
**
*Material, name=high_ductility
*Density
7850.,
*Elastic
 2e+11, 0.33
*Inelastic Heat Fraction
          0.9,
*Plastic
    4.9e+08,    0., 293.
 6.7564e+08,  0.2, 293.
```

7.4359e+08, 0.4, 293.

7.9435e+08, 0.6, 293.

8.3641e+08, 0.8, 293.

8.73e+08, 1., 293.

9.0575e+08, 1.2, 293.

9.3561e+08, 1.4, 293.

9.6321e+08, 1.6, 293.

9.8897e+08, 1.8, 293.

1.0132e+09, 2., 293.

1.0361e+09, 2.2, 293.

1.0579e+09, 2.4, 293.

1.0788e+09, 2.6, 293.

1.0987e+09, 2.8, 293.

1.1179e+09, 3., 293.

1.1364e+09, 3.2, 293.

1.1543e+09, 3.4, 293.

1.1716e+09, 3.6, 293.

1.1884e+09, 3.8, 293.

1.2047e+09, 4., 293.

1.2206e+09, 4.2, 293.

1.236e+09, 4.4, 293.

1.2511e+09, 4.6, 293.

1.2658e+09, 4.8, 293.

1.2802e+09, 5., 293.

4.4923e+08, 0., 400.

6.1941e+08, 0.2, 400.

6.8171e+08, 0.4, 400.

```
 7.2825e+08,   0.6, 400.
 7.6681e+08,   0.8, 400.
 8.0035e+08,    1., 400.
 8.3038e+08,   1.2, 400.
 8.5776e+08,   1.4, 400.
 8.8306e+08,   1.6, 400.
 9.0667e+08,   1.8, 400.
 9.2888e+08,    2., 400.
...
 7.5297e+07,    4.,1700.
 7.6289e+07,   4.2,1700.
 7.7255e+07,   4.4,1700.
 7.8197e+07,   4.6,1700.
 7.9117e+07,   4.8,1700.
 8.0016e+07,    5.,1700.
*Rate Dependent, type=YIELD RATIO
      1.,     0.
 1.1493,   100.
 1.1584,   200.
 1.1638,   300.
 1.1676,   400.
 1.1706,   500.
...
 1.2362,60000.
*Shear failure, type=tabular
    0.8410, ,  -1.5000
    0.8837, ,  -1.4000
```

0.9289, , -1.3000

0.9765, , -1.2000

1.0268, , -1.1000

1.0798, , -1.0000

1.1358, , -0.9000

1.1949, , -0.8000

1.2573, , -0.7000

1.3232, , -0.6000

1.3927, , -0.5000

1.4660, , -0.4000

1.5435, , -0.3000

1.6252, , -0.2000

1.7115, , -0.1000

1.8025, , 0

1.8986, , 0.1000

2.0000, , 0.2000

2.1071, , 0.3000

4.0000, , 0.3300

*Specific Heat

452.,

**

** INTERACTION PROPERTIES

**

*Surface Interaction, name=INTPROP-1

*Friction

0.1,

*Surface Behavior, pressure-overclosure=HARD

```
**
** BOUNDARY CONDITIONS
**
** Name: BC-1 Type: Displacement/Rotation
*Boundary
projectile_bc, 1, 1
projectile_bc, 6, 6
** Name: BC-2 Type: Displacement/Rotation
*Boundary
shield_bc1, 1, 1
shield_bc1, 2, 2
shield_bc1, 6, 6
** Name: BC-3 Type: Displacement/Rotation
*Boundary
shield_bc2, 1, 1
shield_bc2, 6, 6
**
** FIELDS
**
** Name: Field-1    Type: Temperature
*Initial Conditions, type=TEMPERATURE
shield_temperature, 293.
** Name: Field-2    Type: Velocity
*Initial Conditions, type=VELOCITY
projectile_initial_velocity, 1, 0.
projectile_initial_velocity, 2, -800.
**
```

```
** STEP: Step-1
**
*Step, name=Step-1
*Dynamic, Explicit, adiabatic
, 0.0006
*Bulk Viscosity
0.06, 1.2
**
** INTERACTIONS
**
** Interaction: Int-1
*Contact Pair, interaction=INTPROP-1, mechanical constraint=KINEMATIC,
cpset=Int-1
shield_CNS_, projectile_RigidSurface_
** Interaction: Int-2
*Contact Pair, interaction=INTPROP-1, mechanical constraint=KINEMATIC,
cpset=Int-2
shield_contact_1a, shield_contact_1b
** Interaction: Int-3
*Contact Pair, interaction=INTPROP-1, mechanical constraint=KINEMATIC,
cpset=Int-3
shield_contact_2a, shield_contact_2b
** Interaction: Int-4
*Contact Pair, interaction=INTPROP-1, mechanical constraint=KINEMATIC,
cpset=Int-4
shield_contact_3a, shield_contact_3b
** Interaction: Int-5
```

```
*Contact Pair, interaction=INTPROP-1, mechanical constraint=KINEMATIC,
cpset=Int-5
shield_contact_4a, shield_contact_4b
** Interaction: Int-6
*Contact Pair, interaction=INTPROP-1, mechanical constraint=KINEMATIC,
cpset=Int-6
shield_contact_5a, shield_contact_5b
** Interaction: Int-7
*Contact Pair, interaction=INTPROP-1, mechanical constraint=KINEMATIC,
cpset=Int-7
shield_contact_6a, shield_contact_6b
**
** OUTPUT REQUESTS
**
*Restart, write, number interval=1, time marks=NO
**
** FIELD OUTPUT: F-Output-1
**
*Output, field
*Node Output
A, RF, U, V
**
** FIELD OUTPUT: F-Output-2
**
*Contact Output
CSTRESS,
**
```

```
** FIELD OUTPUT: F-Output-3
**
*Element Output
DENSITY, FV, LE, PE, PEEQ, S, SDV, STATUS, TEMP, UVARM
**
** HISTORY OUTPUT: H-Output-1
**
*Output, history
*Node Output, nset=shield_output
U1, U2, V1, V2
**
** HISTORY OUTPUT: H-Output-2
**
*Energy Output, elset=shield
ALLAE, ALLFD, ALLKE, ALLPD
**
** HISTORY OUTPUT: H-Output-3
**
*Node Output, nset=projectile_output
V2
*End Step
```